

Copyright is owned by the Author of the thesis. Permission is given for a copy to be downloaded by an individual for the purpose of research and private study only. The thesis may not be reproduced elsewhere without the permission of the Author.

**A Novel, Neuroscience-based Control Paradigm
for
Wearable Assistive Devices**

A thesis presented in partial fulfilment of the
requirements for the degree of

Doctor of Philosophy
in
Engineering

at Massey University, Albany,
New Zealand.

Frazer Kingsley Noble

2013

The author declares that this is his own work, except where due acknowledgement has been given. This thesis is submitted in fulfilment of the requirements of a PhD. in Engineering at Massey University, Albany, New Zealand.

This thesis describes the research carried out by the author at the School of Engineering and Advanced Technology (SEAT), Massey University Albany, New Zealand from November 2009 to February 2013, supervised by Associate Professor Dr. Johan Potgieter and Professor Dr. Peter Xu.

Acknowledgements

I would like to express my deep gratitude to my supervisors, Associate Professor Johan Potgieter and Professor Peter Xu: their encouragement, guidance, and support over these few years has helped me grow as an independent researcher.

I would also like to extend my thanks to the faculty of Massey University's School of Engineering and Advanced Technology for their assistance. Special thanks is offered to Professor Olaf Diegel for his support.

On a personal note, I would like to acknowledge the support of my parents, David and Cristine Noble; brother and sister, Rhys and Frances-Elise Noble; and grandparents, Kingsley and Dawn Collins, and Stella Noble.

I would also like to thank the friends who supported and motivated me during the course of my studies.

Finally, I thank God, through whom all things are possible.

The author was supported with a Massey University Doctoral Scholarship

Abstract

The biological domain has evolved in such a way that it efficiently overcomes many problems we struggle to solve in the engineering domain; for example, bipedal locomotion, which requires a number of desirable attributes, e.g. compliance and adaptability. As such, the aim of this research has been to provide a bridge between the biological and engineering domains, capturing these attributes, and developing an enabling control technology. The application of this research has been around wearable assistive devices: devices that assist rehabilitation and recuperation of lost or impaired functions or enable an end user to perform difficult to complete tasks. As such, this thesis presents a novel, neuroscience-based control technology for wearable assistive devices. Major contributions of this work include reproducing both biological movement's compliant and adaptive properties in the engineering domain.

The presented approach consists of using an assistive device, whose joints are antagonistically actuated using compliant pneumatic muscles, and central pattern generators. The assistive device's actuators make the arm robust to collision and give it smooth, compliant motion. The pattern generators produce the rhythmic commands of the joints of the assistive device, and the feedback of the joints' motion is used to modify each pattern generator's behaviour. The pattern generator enables the resonant properties of the assistive device to be exploited to perform a number of simulated rhythmic tasks.

As well as providing a wealth of simulated and real data to support this approach, this thesis implements integrate-and-fire, Izhikevich, and Hodgkin-Huxley neuron models, comparing their output based on firing patterns observed in neurons of the nervous system. These observations can be used as a mechanism for deciding the "realism" needed to represent a neural system's characteristics. In addition, Hill's muscle model has been presented, and simulation of an implemented soleus muscle carried out. Parametric variation provides quantitative insight into passive and active series and parallel elements' roles in generating tension and tension's time-response characteristics. Furthermore, an antagonistically coupled pair of extensor and flexor muscles have been presented and shown to effect compliant joint actuation

of a modelled limb under differential activation. Co-activation of the extensor and flexor has been shown to increase a joint's stiffness, leading to increased stability and rejection of limb perturbation.

Thesis Supervisor: Johan Potgieter

Title: Associate Professor

Thesis Supervisor: Peter Xu

Title: Professor

Contents

1	Introduction	1
1.1	Synopsis	1
1.2	Approach	3
1.3	Comparisons	6
1.4	Contributions	9
1.5	Thesis outline	11
1.6	Notes on Data in the Thesis	14
2	Literature Review	15
2.1	Introduction	15
2.2	Assistive Devices and Control	16
2.3	Organisation of the Nervous System	24
2.4	Neurons and Neuron Models	27
2.5	Skeletal Muscle, Models, and Engineering Parallels	30
2.6	Muscle Sensory Organs	37
2.7	Pattern Generating Pathways and Models	40
2.8	Summary	48
3	Hill's Model, Parametric Variation, and Antagonistic Actuation	51
3.1	Introduction	52
3.2	Hill's muscle model	53
3.3	Determining muscle's properties	55
3.4	Methodology	56

3.5	Muscle Parameter Fitting	57
3.6	Passive and Active Muscle Parameter Analysis	58
3.7	Antagonistic Actuation	63
3.8	Summary	66
4	Novel Central Pattern Generator and Analysis	70
4.1	Introduction	71
4.2	The Central Pattern Generator	72
4.3	Analysis Methodology	79
4.4	Pattern Generator Describing Function	82
4.5	Limit Cycle Stability	85
4.6	Parameter Evaluation	86
4.7	Summary	87
5	The McKibben Muscle, Antagonistic Actuation, and Antagonistic Controllers	90
5.1	Introduction	91
5.2	The McKibben Muscle Model	92
5.3	Methodology	95
5.4	Static and Dynamic Modelling	96
5.5	Antagonistic Coupling	99
5.6	Antagonistic Actuator Control Paradigm	104
5.7	Summary	106
6	Assistive Device Controller and Antagonistic Actuator	109
6.1	Introduction	110
6.2	Methodology	112
6.3	Fabricated McKibben Muscle	113
6.4	Static and Dynamic Assistive Device Controller properties	121
6.5	Antagonistic Actuator and Realised Controller	123
6.6	Static and Dynamic Actuator and Controller properties	130
6.7	Summary	131

7 Conclusion	135
7.1 Future Work	135
7.2 Discussion	137
7.3 Summary	140
References	144

List of Figures

1-1	Assistive device control schematic.	5
1-2	Pattern generator and wearable assistive device coupling.	6
1-3	Comparison between traditional and compliant control.	7
1-4	Comparison between traditional and pattern generator control.	8
1-5	Graph of thesis' chapters, topics, and contributions.	12
2-1	Block diagram of literature review's sections and topics.	17
2-2	Active wearable assistive device.	20
2-3	Passive supportive assistive devices.	21
2-4	Raytheon's XOS2 active exoskeleton.	22
2-5	Schematic of the closed-loop control paradigm.	23
2-6	Overview of the anatomical organisation of the nervous system.	24
2-7	Divisions of the nervous system and external view of the brain and spinal cord.	25
2-8	Example of neurons in the nervous system.	28
2-9	The nervous system's skeletal muscle.	31
2-10	Myosin and actin ratcheting mechanism.	32
2-11	Hill's muscle model.	34
2-12	Example pneumatic McKibben muscle.	35
2-13	The muscle spindle sensory organ.	38
2-14	The muscle spindle sensory organ.	39
2-15	Rybak et al.'s central pattern generator model.	46
2-16	Matsuoka central pattern generator.	48

3-1	Hill's muscle model.	55
3-2	Hill muscle model ramp stretched tension	59
3-3	Hill muscle model parameter' effects on passive tension	62
3-4	Hill muscle model parameter' effects on active tension	64
3-5	Differential activation of antagonistic Hill-type muscle models.	67
3-6	Coactivation of antagonistic Hill-type muscle models.	68
4-1	Schematic of the pattern generator.	73
4-2	Dirac delta plot.	75
4-3	Linear kernel.	76
4-4	Natural central pattern generator output.	77
4-5	Pattern generator behaviour under changing tonic T excitation.	78
4-6	Plot of pattern generator and coupled system.	78
4-7	Power density spectrum of the pattern generator.	79
4-8	Coupled pattern generator and system schematic.	80
4-9	Phase plot of the coupled pattern generator and system $L(j\omega)$	82
4-10	Coupled pattern generator and system Bode plot.	84
4-11	Complex plane plot of coupled system's $N(A, j\omega)$ and $J(j\omega)$	85
4-12	Figure showing the effect of varying the damping ratio of the linear system.	88
4-13	Power density spectrum for coupled pattern generator with changing system dynamics.	88
5-1	Basic McKibben muscle model's force, contraction ratio plot.	96
5-2	Static friction-incorporating McKibben muscle model's force, contraction ratio plot.	98
5-3	Dynamic friction-incorporating McKibben muscle model's force, contraction ratio plot.	100
5-4	Differential activation of antagonistic McKibben muscles.	102
5-5	Coactivation of antagonistic McKibben muscles.	103
5-6	Schematic of the torque controller, differential pressure controller, antagonistic muscles, and modelled limb.	105

5-7	Differential pressure controller's evoked transient response.	106
5-8	Torque controller's evoked transient response.	107
6-1	Assistive device control schematic.	112
6-2	McKibben muscle testing apparatus.	114
6-3	Fabricated pneumatic McKibben muscle.	115
6-4	Fabricated McKibben muscle's force-length plot ($P = [1,3,5]$ bar). . .	119
6-5	Fabricated McKibben muscle's force-length plot ($P = [2,4]$ bar). . .	120
6-6	Optimised McKibben muscle's force-length plot ($P = [1,3,5]$ bar). . .	121
6-7	Optimised McKibben muscle's force-length change plot ($P = [2,4]$ bar).122	
6-8	Assistive Device controller's evoked transient response plots.	124
6-9	Driven assistive device controller's transient response plot.	125
6-10	BeagleBoard-xM embedded target.	127
6-11	Arduino Uno sensor interface.	128
6-12	Static antagonistic actuator's transient response plot.	132
6-13	Dynamic antagonistic actuator's transient response plot.	133
7-1	Multiple degree-of-freedom manipulator.	139
7-2	Block diagram of thesis' chapters and topics.	141

List of Tables

3.1	Hill-type muscle model parameters used during simulation.	58
6.1	Table of fitted force curve parameters ($P = 1$ bar).	117
6.2	Table of fitted force curve parameters ($P = 2$ bar).	117
6.3	Table of fitted force curve parameters ($P = 3$ bar).	118
6.4	Table of fitted force curve parameters ($P = 4$ bar).	118
6.5	Table of fitted force curve parameters ($P = 5$ bar).	119
6.6	Table of optimised McKibben muscle model's parameters.	122
6.7	Table of RMS values of optimised McKibben muscle model's parameters.	122

Chapter 1

Introduction

1.1 Synopsis

The need to amplify humans' natural strength, in order to assist the recuperation and rehabilitation of lost or impaired neuromuscular functions, or augment the strength of healthy people performing physically arduous tasks, presents an opportunity for a range of assistive technologies, e.g. wearable assistive devices (WAD), which assist rehabilitation and recuperation of lost or impaired functions or enable an end user to perform difficult to complete tasks, to assist in many of life's everyday tasks. However, current actuation, drive, and control technologies, which exhibit low compliance, comfort, and intelligence, it is argued, are limiting factors; preventing wearable assistive devices from moving beyond the prototype stage and into commercially viable deployment.

The work described in this thesis is motivated by the need for enabling technologies; necessary for the development of wearable assistive devices. To overcome current technologies' shortcomings, this research has looked towards the biological domain for inspiration in developing an engineering solution to the current limitations. The nervous system has been identified as possessing a wide range of desirable properties, e.g. compliance and adaptation, which literature review has identified as being due to muscle's structure and operation, and functional grouping of neurons,

termed "central pattern generators", found in the spinal-cord and brainstem [55][35]

Based on observations made during experiments with spinal-cord transected cats and dogs, Graham Brown's half-centre oscillator (HCO) provides a framework upon which a number of pattern generator models have been developed. Although there exists a number of CPGs in literature, this thesis has identified two models of note: Rybak et al.'s dual layered, rhythm and pattern formation model, which represents the most up-to-date modelling of the locomotor pattern generator; and Matsuoka's single layered, reciprocally connected, mutually inhibited model, which represents a CPG at its most abstract, yet has found widespread usage, in contrast to Rybak et al.'s.

A key property of pattern generators is their ability to produce rhythmic output in the absence of descending tonic input, where sensory feedback elicits a motor pattern relative to its intensity and duration; or ascending feedback, where descending activation elicits stereotyped motor patterns lacking adaptation. With application to wearable assistive devices, a pattern generator can be used to specify a joint's set-point; where, angular feedback can be passed to the CPG's input, which in turn accounts for the limb's dynamics by adapting its firing rate.

In addition to pattern generators, this thesis has found skeletal muscles are an integral component in the nervous system's generation of compliant and adaptive movement. In terms of traditional mechanics, muscles represent damped "spring-like" actuators, whose tension is a function of active contractile force generated by myosin and actin proteins' half-bridging. A number of muscle models have been identified [22]; however, Hill's model has been found to be the most widely used to describe muscle tension, representing it as a combination of parallel and series, active and passive elements' forces. From this model, a number of conclusions can be drawn; namely, muscle tension is not only dependent on innervation frequency, but also on muscle length - displaying a Gaussian-like force distribution about the point when half contracted. Bridging the gap between the skeletal muscle and traditional mechanisms of actuation, the pneumatic McKibben muscle has been shown to be in agreement with Hill's three element representation of muscles; possessing equivalent force-length properties.

Since muscles, both skeletal and McKibben, are entirely contractile elements, the nervous system has evolved an antagonistic coupling of extensor and flexor muscles in order to effect bidirectional rotation of a limb's joint. Differential activation of the two muscles leads to smooth and compliant rotation, in effect varying a joint's equilibrium point. In contrast, coactivation doesn't vary a joint's angle; rather, it changes its stiffness - a useful mechanism for matching a joint's compliance to a desired level. With respect to wearable assistive devices, the ability to vary stiffness and ensure safe and stable actuation of a limb overcomes a number of the limitations imposed on assistive devices by current technologies.

Having identified CPGs and muscles' roles in producing compliant and adaptive movement, this thesis presents an assistive device control paradigm consisting of a pattern generator driven, antagonistically actuated system. Joint torque is generated by coupled extensor and flexor McKibben muscles, whose pressure difference results in a moment that effects a limb's rotation about a joint. The joint's set-point is specified by the rhythmic output of the pattern generator, which in turn receives input from the joint's angular position. The CPG adapts its output's frequency, entraining to a coupled resonance. In this paradigm, the joints' CPGs are coupled through the assistive device's dynamics; rather than explicit connections between the each network.

The following sections present the approach in more detail, commenting on the relations between this work, previous authors', states the contribution of this thesis, and introduces the subsequent chapters.

1.2 Approach

This section describes the approach taken in this thesis: the choice and use of the presented pattern generator and the antagonistically coupled, pneumatic muscle actuators.

In designing a wearable assistive device, an important consideration is the stiffness of the device's linkages and joints. For tasks that require a robust interaction with an unknown environment, the assistive device's joints should be as compliant as

possible. For tasks that require accuracy, the device’s linkages and joints need to be as stiff as possible. With respect to traditional control, if a joint is compliant, there is no guarantee that output of a rotating or translating medium is at the position required, making the control of the assistive device’s joints much more difficult. For the work in this thesis, antagonistically actuated pneumatic, muscle actuators have been proposed to be used.

The pneumatic muscles work by expanding a silicon tube, which is encapsulated within a mesh braid. The braid forms a pantograph, which constrains the radial expansion of the muscle’s cylindrical body; resulting in a maximum contraction proportional to approximately 20% of the muscle’s nominal length. The force generated by the actuators is a function of the muscle’s length, the mesh braid angle, and the pressure being supplied. The pneumatic muscle used within this thesis have been shown to be congruent with biological muscle models [59]; generating a maximum force at 0% contraction and 0% force at maximum contraction. The force-length characteristics are similar to that of skeletal muscle [22], decreasing exponentially as the muscle shortens. Due to the contractile nature of the pneumatic muscle it is necessary for two to be coupled in a state of antagonism, i.e. an extensor and flexor pairing of muscles. By measuring the angular displacement of the assistive device’s joint, the force generated in the muscle can be controlled.

The pneumatic muscles’ antagonism contributes to the compliance of the assistive devices joint’s, ensuring the actuated assistive system is safe for a human to use and stable when perturbed. An advantage of the antagonistic actuation lies in the ability to coactivate muscles; increasing the nominal pressure of the muscles can increase the joint’s stiffness or conversely its compliance. There exist a number of real world cases where this is a desirable property, e.g. when throwing a tennis ball the arm is supple, transferring a maximum amount of energy to the ball; however, when catching, the opposite is true: the limb’s joints are very stiff, absorbing a maximum force. Furthermore, the ability to vary the wearable assistive device’s dynamics can facilitate the pattern generator’s entrainment to varying loads connected to the assistive device.

To control the wearable assistive device, the presented pattern generator is used

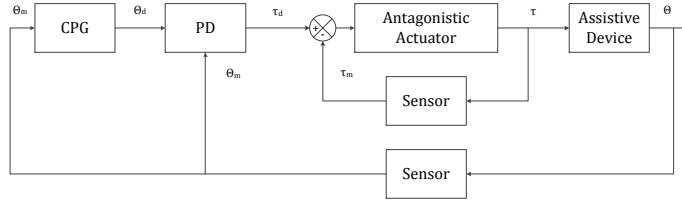


Figure 1-1: The assistive device’s control paradigm’s schematic. The pattern generator is coupled to the antagonistic actuators via a PD control law, whose output is the desired torque τ_d . The antagonistic actuator’s torque controller follows the input, generating a corresponding torque τ that acts upon the plant. The plant’s angle θ_m is fed back into the antagonistic actuator, PD controller, and CPG closing the loop.

to drive each of the devices joint’s set-points. The CPG model presented in this thesis consists of two adaptive exponential integrate-and-fire neurons [14], which are reciprocally coupled and mutually inhibited, as per Graham Brown’s half-centre concept [5][6], resulting in an oscillatory system. In the absence of feedback, the CPGs will generate a fixed frequency output; however, once an input is applied, the pattern generators entrain to an approximately resonant frequency. The pattern generators sync to the wearable assistive device’s state using feedback from the devices joint’s (e.g. angular position). The system is tightly coupled (see figure 1-2), where each of the assistive devices’ joints’ set-points are individually driven.

The pattern generator’s behaviour makes the system suitable to adaptive controllers for a wearable assistive device. Once an assistive device is configured and a natural frequency of oscillation determined, the pattern generators will respond to the coupled system; injecting energy as its natural frequency shifts to the resonant frequency of the coupled system. The work in this thesis concentrates on evaluating, explaining, and understanding the pattern generator’s behaviour in conjunction with the antagonistically actuated pneumatic muscles.

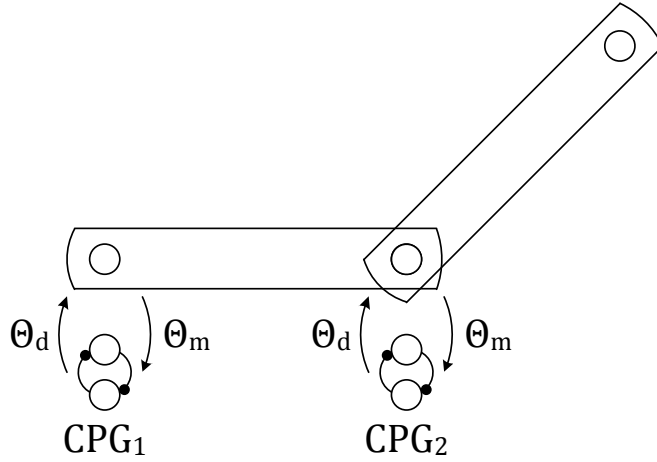


Figure 1-2: The pattern generators are coupled to each of the wearable assistive device’s joints. The angular feedback is used as the CPG’s inputs, to which the pattern generators entrain to. Generally, each joint’s pattern generator doesn’t interact with neighbouring CPGs; rather, interacting via the assistive device’s mechanical structure.

1.3 Comparisons

The main difference between the traditional control and that used here for a wearable assistive device is how the dynamics of the coupled system is handled. Traditionally, a robot is viewed as a general purpose manipulator, performing tasks independent of its configuration. Tasks are specified in terms of a desired trajectory or set-point, which the robot works towards achieving. Generally, robot dynamics are ignored and typically don’t play a role in how the task is effected. In this thesis, the control of a wearable assistive device has been approached from the opposite perspective: that complex behaviour can be obtained by exploiting the system’s dynamics. In fact, the core reason for using a pattern generator is to exploit the coupled system’s dynamics.

The difference in the approach is presented in 1-3. The task illustrated is that of a moving a mass back and forward. In traditional control, dynamics of the robot are removed, so the equivalent connections between the desired position of the mass

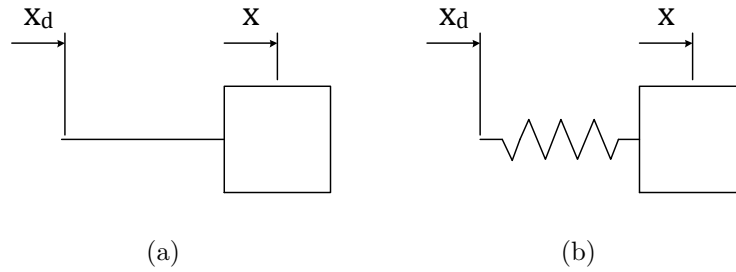


Figure 1-3: Comparison between traditional control (a), and exploiting natural dynamics (b) for the task of moving a mass back and forward. Under traditional control, the mass will be displaced the same distance as the input, i.e., the dynamics of the linkage is not used. If, however, the dynamics of the system were exploited, the output could be achieved; albeit, it a unique manner. For a mass attached to a spring displacement of its free end will cause it to oscillate. The role of the controller is then to maintain its oscillation at the desired position.

x_d , and its actual position x is stiff. The set-point trajectory x_d is necessary to move the mass back and forward, and the controller need only overcome the mass and frictional damping of the system. If the dynamics of the coupling mechanism is to be exploited, represented as as spring, the situation changes. The natural behaviour of the mass is to vibrate on the spring, moving back and forward. The role of the trajectory x_d is now to inject and remove energy to sustain the motion, not to create the motion.

The traditional approach is much more general, since the mass can be moved in any arbitrary trajectory. However, for the rhythmic task, the alternative has some advantages. One consequence of exploiting the dynamics is that the linkage needs to be compliant. This has the benefit of giving robust interactions with objects. In terms of traditional control, stiffness needs to be high to minimise tracking errors, and unexpected collisions are not dealt with well. Too high of a stiffness can lead to instability issues.

The second difference is in terms of the design of the controller, and is schematically shown in 1-2. While a traditional controller requires a desired trajectory x_d , the pattern generator control generates the signal using internal dynamics. As be-

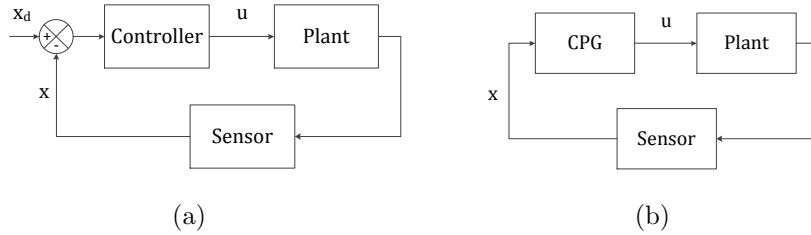


Figure 1-4: Comparison between traditional control (a) and pattern generator (b). In traditional control the plant’s output is controlled to follow the desired set-point by the controller. The pattern generator control does not receive an explicit set-point; rather, it generates its output internally, modifying its output based on the state of the coupled system.

fore, the typical controller is more general, and the pattern generator system being restricted to the trajectories being generated by the pattern generator’s dynamics.

The main advantage of using the pattern generator is that the desired trajectory is reactive to the dynamics of the system. For a spring-mass system, the pattern generator can generate a motor command, which complements the motion of the mass; injecting and removing energy. The trajectory generated by the pattern generator is reactive since it is calculated within a tight loop, and is synchronised with the system’s motion since it is generated relative to the system’s state. These characteristics are achieved without a separate system to calculate the desired trajectory and independent of extra sensing, modelling, and computations.

In the case where pattern generators are controlling multiple assistive device joints, the internal generation of trajectories is even more advantageous. The pattern generators are independent coupled only through the assistive device’s dynamics. The trajectories for all the joints are thus generated in a distributed manner, with coordination which is correct relative to the motion of the wearable assistive device. This contrasts with the complexity of the system required to generate explicit trajectories for all the joints. The difference is accentuated by the versatility of the pattern generators. While calculating x_d for one task is relatively straight forward, the computation for each joint could be tedious and require extra complexity of kinematic modelling and calibration

A further difference between the traditional case and pattern generator control approach is that the pattern generator control system doesn't deteriorate as the speed of the task increases and the dynamics of the wearable assistive device become significant.

1.4 Contributions

This research has made a number of contributions; amongst which, the main, or “key”, contributions are as follows:

- **Adaptability:** having identified the functional role of central pattern generators (CPGs), as discussed, this research has successfully modeled, developed, implemented, and experimented with an adaptive CPG-based wearable assistive device (WAD) control technology, not seen previously in literature. This research demonstrates the ability of the presented controller to adapt to different stimuli, changing its output frequency, which enables adaptive control of any driven system, given feedback.
- **Compliance:** having identified the functional role of skeletal muscles in movement, as discussed, this research has successfully modeled biological muscles using Hill's model, and designed, fabricated, modeled, and experimented with McKibben pneumatic muscles, which has led to an antagonistically actuated joint control paradigm. This research has shown that by varying the pressure between the antagonistic actuators, the joint stiffness changes; enabling control of a joint's compliance.

To demonstrate the “real” applicability of this research, consider the following scenario: (a) a tennis ball is about to be thrown, (b) a tennis ball is about to be caught, and (c) having caught the tennis ball in (b), the example's participants are shaking hands. In case (a) the muscles that rotate the thrower's elbow and wrist's joints are activated such that the limb is stiff, ensuring maximum amount of force is transferred to the tennis ball. In the second case, the catcher's limb's muscles are

not as strongly activated, effecting a compliant joint, and ensuring the ball is caught safely. Finally, in the third case both the throwers and catcher’s limbs are activated in such a way to generate the characteristic handshaking movement, where each limb reaches a mutually “agreeable” rate of hand shaking.

In the above example we see two things: both the thrower’s and catcher’s arms are varying their limb’s joints’ stiffness, i.e. implementing compliance control, in response to the required tasks, i.e. throwing and catching, and following coupling of the limbs, i.e. gripping each other’s hand, each limb entrains to the coupled system’s natural frequency (one which reduces the metabolic cost of the hand shaking movement), i.e. demonstrating adaption. Moreover, these real responses/attributes are exactly what this research has reproduced in the engineering domain: a CPG-based controller, which adapts to changes in stimuli that in turn drives an antagonistically coupled pair of actuators, which can vary a joint’s compliance in response to the demands of the CPG’s output.

With respect to literature, a central pattern generator-based, antagonistically actuated control technology for wearable assistive devices has not been seen previously. Certainly, the integration of these two sub-systems is a novel scientific contribution; furthermore, we have not seen previously works which describe the bridging of biological means of control, e.g. of locomotion and complex reaching tasks, into the engineering domain, and certainly not with respect to wearable assistive devices.

Additional contributions of this thesis are as follows:

- Implemented Integrate-and-Fire, Izhikevich, and Hodgkin-Huxley neuron models, comparing their output to typical neuron behaviour. Our observations can be used as a tool to help decide what level of abstraction an engineer or researcher may need in order to represent a neural system’s biological aspects.
- Implemented a Hill-type soleus muscle model and performed parametric variation of passive and active parallel and series element’s stiffness and damping. Our results can be used to determine parallel and series elements’ stiffness and viscosity.

- Antagonistic coupling of two Hill-type muscle models has been shown to effect smooth and compliant joint rotation. Results demonstrate coactivation of the extensor and flexor muscle can be used to vary a joints stiffness, which can be used to match a joint’s compliance to a desired value.
- A novel, neuroscience-based, pattern generator has been developed and implemented, which has been shown to be able to generate rhythmic oscillations. Results demonstrate that when coupled to a mechanical system, the CPG is able to entrain to the plant’s dynamic feedback.
- Antagonistic coupling of two McKibben-like muscles has been implemented. Results demonstrate their suitability for actuation of a wearable assistive device. Differential activation of the extensor and flexor muscle has been shown to effect smooth and compliant joint rotation. In addition, muscle coactivation demonstrated the ability to control a joint’s stability.
- Descending activation of spinal pattern generators, the spinal-cords CPG’s operation, and muscles’ antagonism has been replicated in the engineering domain using model-based simulation environment Simulink. Embedded systems have been shown to be a suitable environment in which to execute the assistive device’s model-based control algorithm.

1.5 Thesis outline

The structure of this figure is indicated as in figure 1-5 and proceeds as follows:

- **Chapter Two.** In this chapter, the thesis reviews the current state of assistive technologies, categorising examples. The review goes on to provide an overview of the nervous system, identifying key areas. Following that, the review investigates the neuron and discusses a number of model types. The review goes on to look at muscles and muscle’s sensory organs, discussing the role of alpha-gamma coactivation and the myotatic reflex, as well as, a number of muscle

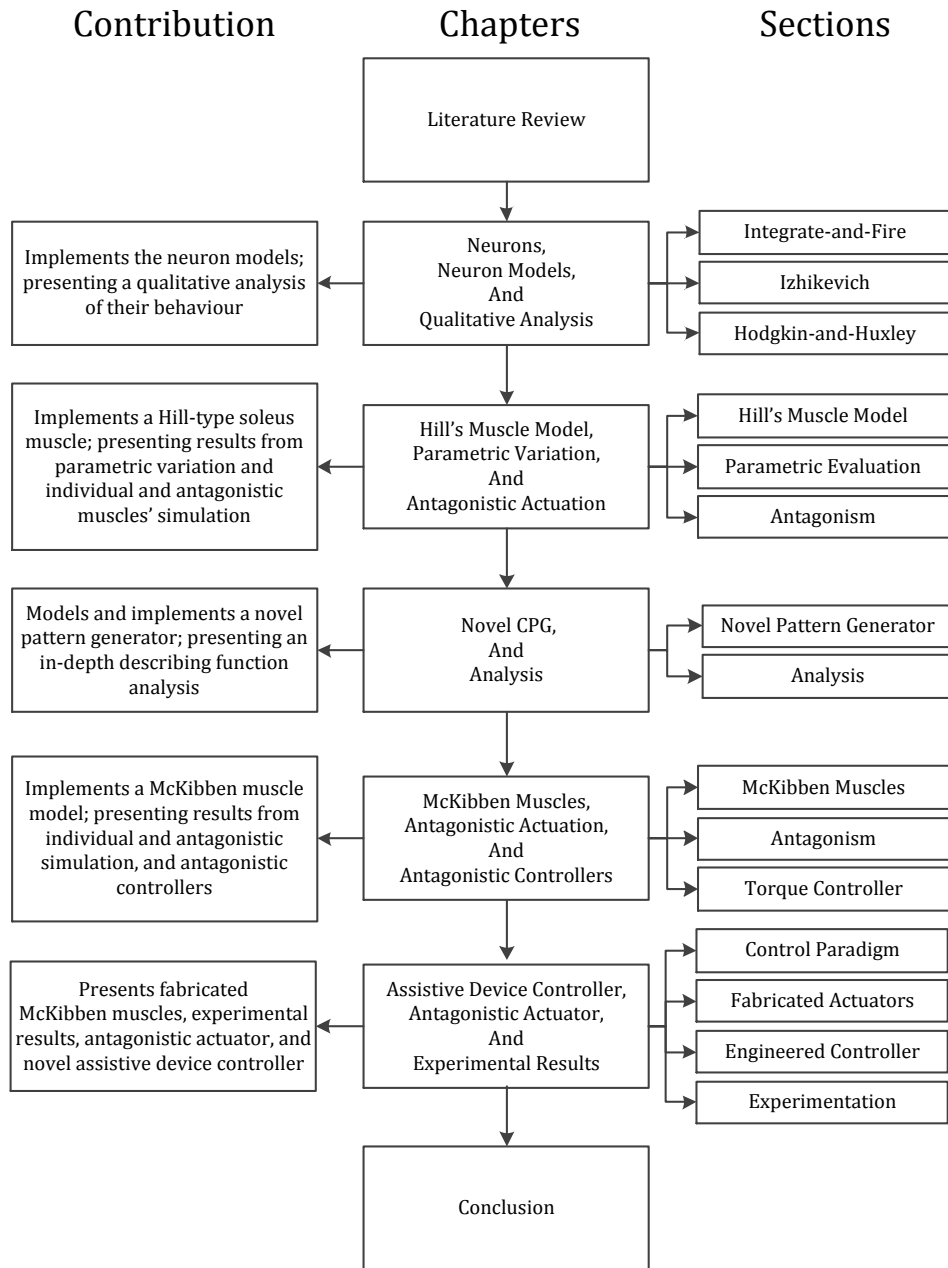


Figure 1-5: Block diagram of the thesis' chapters, chapter's topics, and chapter's contributions.

models and engineering parallels. The review then introduces central pattern generators, discussing their operation and a number of models.

- **Chapter Three.** In this chapter, the thesis presents the Integrate-and-Fire, Izhikevich, and Hodgkin-Huxley neuron models. Special attention is applied to Hodgkin and Huxley's model as it forms a framework upon which most, if not all, subsequent models found in literature are derived. Each model is implemented and simulated in the Simulink environment. The output is compared to each others and subsequently to observations made of neurons found in the nervous system.
- **Chapter Four.** In this chapter, the thesis presents Hill's muscle model and a parametric analysis of a soleus muscle implementation. Passive and active series and parallel elements' effects on the tension's stretch and transient response are presented and discussed. An antagonistically coupled pair of extensor and flexor muscles are presented and results from differential and coactivation shown.
- **Chapter Five.** In this chapter, the thesis' novel central pattern generator, which consists of two, mutually inhibited, Integrate-and-Fire neurons, is presented. Given a tonic input T , the pattern generator is shown to autonomously generate rhythmic output. When feedback is applied, the CPG entrains to a near resonance frequency. Subsequently, an in-depth describing function analysis is presented and the robustness and sensitivity of the pattern generator discussed.
- **Chapter Six.** In this chapter, the thesis introduces the McKibben muscle, discusses the actuator's model, and presents results of individual and antagonistic muscles' simulations. Differential activation, where the extensor receives a pressure greater than the flexor, is shown to effect joint rotation. Subsequently, coactivation, where the antagonistic actuators receive equal pressure, is shown to increase joint stiffness, enabling control of a joint's compliance. In

addition, differential pressure and torque controllers are presented and shown to effect smooth and compliant rotation.

- **Chapter Seven.** In this chapter, the thesis presents the assistive device control paradigm, which integrates the discussed pattern generator and antagonistic McKibben muscles. In addition, fabricated McKibben actuators are presented, curves fitted to their produced force, and optimised muscle model parameters given. Subsequently, an antagonistic actuator is presented and results from simulation and experimentation shown.
- **Chapter Eight.** In this chapter, the thesis concludes the presented work, discussing future work and vision for the novel pattern generator and antagonistic McKibben muscles.

1.6 Notes on Data in the Thesis

This thesis includes data both from simulations of the wearable assistive device and the presented test-bed. The figure captions indicate the source of the data. Figures with simulated data are marked SIM, while figures with real data are marked with REAL. This approach is borrowed from [62].

Chapter 2

Literature Review

2.1 Introduction

This thesis has looked towards the biological domain for inspiration in overcoming current technologies impediment of assistive device development. This chapter reviews the relevant literature in assistive devices, their control, the nervous system, muscles, and central pattern generators. Figure 2-1 depicts the structure of this review, which is divided as follows: section 2.2 discusses the current state of assistive device technologies and their control; section 2.3 provides an overview of the nervous system and identifies key areas responsible for compliant and adaptive movement; section 2.4, which introduces the neuron, describes its structure and operation, and presents a number of models; section 2.5, which discusses the operation and structure of skeletal muscles, presents macro- and micro-scopic models and engineering parallels; section 2.6, which discusses muscle's sensor organs' operation and structure, identifies the roles of gamma-motor neurons and the myotatic reflex pathway; section 2.7, which presents an in-depth review of central pattern generators, gives arguments for their existence, discusses their operation, and identifies a number of CPG models; section 2.8, which concludes this chapter, identifies and discusses a number of important points.

This review has largely focused on, though not limited to, the following topics:

- **Biological movement control:** the hierarchy of the nervous system is investigated, the origin of descending signals and their roles identified, the operation of functional grouping of neurons in the spinal cord discussed, how muscles operate and how they have been modeled in the past. Since we are bridging between the biological and engineering domains, it is necessary to have sufficient understanding of its architecture and operation.
- **Engineering movement control:** the nature of wearable of assistive devices are investigated, traditional methodology of control discussed, actuator technologies investigated, parallels between biological and engineering structures identified, and different examples of assistive devices presented. As discussed, since we are bridging between biological and engineering domains, we need to understand how we might realize biomimetic systems.

2.2 Assistive Devices and Control

In this section, we review the current state of assistive device technologies; discussing the classical proportional-integral-derivative (PID) algorithm and assistive device's control approach.

Assistive Devices

New Zealand has an ageing population; the median age of (as of 2010) was 36.7 years compared to (2000) 34.3 years (total New Zealand population/gender independent). Furthermore, the percentages of adults with disabilities increases with age: less than 10% of 15 year olds have some form of disability, compared to 45% of adults aged 65 years or older. There are approximately 660,300 New Zealander's (approximately 17% of the population) that have some form of disability, with physical disability most common in adults over 15 years of age. The number one cause of adult disability in New Zealand is disease, followed by injury.

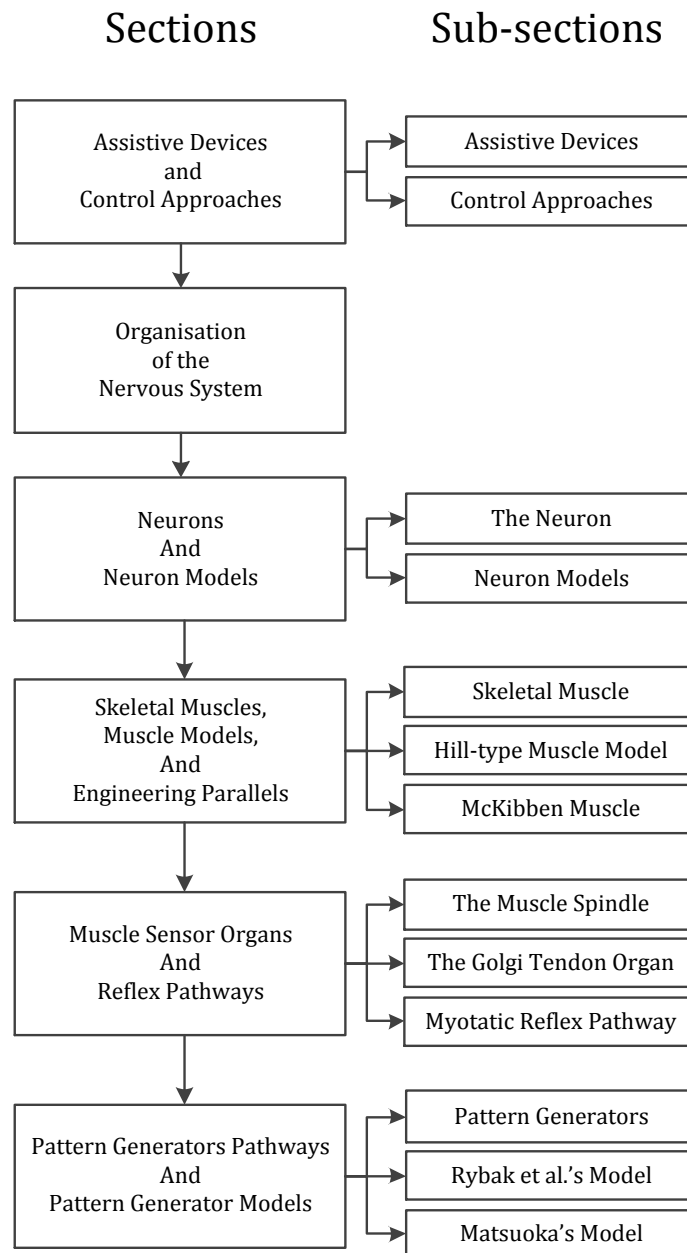


Figure 2-1: Block diagram of the literature review's sections and topics.

To overcome the limitations intrinsic to physical disability, assistive technologies can be used. Assistive devices facilitate the recuperation of, and rehabilitation from, an end-user's injuries, or augments their physical strength. However, component technologies are a limiting factor of their development; where, they are only as light, durable, and small as the underlying actuation mechanism used. For example, if exoskeletons (see figures 2-2(a) - 2-2(b)) are to find further use in upper extremity applications, their core components, e.g. actuators, power supply, and linkages, need to reduce in weight.

Furthermore, traditional control also limits assistive devices' development. Specification of a set-point can be used to drive a joint; however, the usefulness of such an approach is limited by its connection to the underlying mechanism that generates the desired trajectory. For example, in trying to effect locomotion over varied terrain, an assistive device's controller will need to be coupled to the end-user's intention. The problem is: how to express intention in terms of limb joint angles?

A number of assistive technologies exist, the key attributes of which we have classified as follows:

- **Active:** Active technologies are characterised by the use of actuators to effect movement of an end-user's limb. Current actuator technologies include: direct current (DC) motors, pneumatic pistons, and hydraulic rams.
- **Passive:** Passive technologies, in contrast to active assistive devices, are not actuated; rather, passive devices exploit properties, e.g. compliance, inherent to their core component in order to provide assistance.
- **Wearable:** Wearable assistive devices, in contrast to supportive assistive devices, are worn; extending the functions of the end-user's limbs. Typical device include: exoskeletons (see figure 2-2)
- **Supportive:** Supportive assistive devices are peripheral structures, which are used to load-bear; transferring force from the body to a distal plane, upon which the force is exerted. Examples include: walker frames and crutches (see figure 2-3).

These classifications are not mutually exclusive; rather, there may be devices that have a combination of elements, e.g. being both wearable and supportive.

A popular passive support device is the wheelchair (figure 2-3(c)), which has seen widespread and global adoption [26]. Traditionally, the wheelchair has been used by humans who have experienced some form of spinal injury, where the spinal cord has been transected at the thoracic level or below, i.e. the lumbar and sacral vertebrae. Powered wheelchairs, or "powerchairs" [7], represent an active support device and are typically controlled via a joystick, with turning and directional functionality. In addition, supplementary devices, e.g. SmartDrive [7], can be added to passive support devices to make them active.

Originally developed for military purposes, exoskeletons (figure 2-2(a)) have experienced a recent growth in popularity; especially as a wearable assistive device platform. Rex Bionics Ltd. recently released a lower extremity active wearable assistive device (figure 2-2(c)), which was touted as "the world's first hands-free, self-supporting, independently controlled" walking device targeted towards civilian paraplegics [4]. In addition to active lower extremity exoskeletons, Raytheon Sarcos have developed a whole body exoskeleton: the XOS2 [50], which, in contrast to Rex Bionic's exoskeleton, is targeted at able-bodied users with military applications, e.g. logistics.

Classical and Assistive Device Control

Classical control approaches utilise "automatic controllers", such as the proportional-integral-derivative controller (PID), which has found wide usage in industry [3], in a closed-loop configuration (see figure 2-5) [45]. The PID controller works by calculating the difference between a set-point $r(t)$ and a plant's measured output $m(t)$, calculating the error $e(t)$, and generating a control action $u(t)$ that is used to control an actuator and in turn the plant. The PID controller's goal is to minimise the error, tracing variation in the set-point.

Briefly, the PID controller consists of three terms: proportional (P), which depends on the current error value; integral (I), which depends on the error's past



(a)



(b)



(c)



(d)

Figure 2-2: Active wearable assistive device examples. (a) Berkely Robotic’s Human Engineering Laboratory’s lower extremity exoskeleton (BLEX) [51]. (b) Cyberdyne’s hybrid assistive limb (HAL) [11]. (c) RexBionic’s REX exoskeleton [4]. (d) Honda’s assistive device.



Figure 2-3: Examples of passive supportive assistive device examples. (a) Crutches; force is transferred from the upper chest to the ground via crutch's physical structure. (b) Walker frame; force is transferred from the hand grips to the frame's feet. (c) Invacare's Action3NG wheelchair [26]; torque, and subsequent displacement, is generated by force acting perpendicular to the wheel's rim. (d) Melrose Kiwi Concept Chair's powerchair [7]; controlled via a joystick, the power chair is a cost effective active support assistive device.

trajectory; and derivative (D), which predicts the errors future trajectory. Tuning of the PID controller can be achieved using a number of methods, e.g. Ziegler-Nichols [45], which has the advantages of being on-line, but results in a very aggressive controller; and the Coon-Cohen [3], which is popular in process control, though limited only to first-order processes [3]. The response of the system can be explained using time-domain, e.g. step-response plot, or frequency-response, e.g. Bode and Nyquist plots, analysis methods [45]. In addition, classical control design tends to be constrained to linear, time-invariant systems.

The PID controller's control action is the linear combination the proportional, integral, and derivative terms' output as functions of the error. Control action $u(t)$ can be described by the following equation:

$$u(t) = k_c \left(e(t) + \frac{1}{\tau_i} \int_0^t e(\tau) d\tau + \tau_d \frac{d}{dt} e(t) \right) \quad (2.1)$$

where k_c is the proportional gain, τ_i , the integral time constant; τ_d , the derivative time constant; and $e(t)$, the error. The proportional P term produces an output relative to the instantaneous error, which results in proportional changes in $u(t)$. The integral I term produces an output proportional to the error and the error's time-history, speeding up the system's response. The derivative term produces an output proportional to the error and the error's rate of change, slowing down the system's response.

PID control can be used to drive an assistive device's joint; however, as discussed,



Figure 2-4: Raytheon's XOS2 active exoskeleton [50].

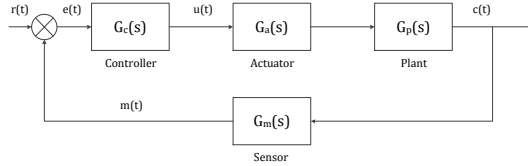


Figure 2-5: A schematic of a closed-loop controller paradigm showing the transfer function of the controller $G_c(s)$, the actuator $G_a(s)$, the plant $G_p(s)$, and the sensor $G_m(s)$.

such an approach is limited by its connection to the underlying mechanism that generates the desired set-point. One approach is to use the principle of shared control to effect the joint’s set points. Under shared control, the assistive device’s end-user actuates a joystick, or similar user-interface device, which in turn can specify the limbs joint’s desired angle. Such an approach has been used for the control of powered wheel chairs [10], as well as Rex Bionic’s lower extremity exoskeleton [4].

Shared control can be classified into two categories:

- **User-based.** Under user-based shared control, an assistive device changes its mode of operation based on a command specified by the end-user, e.g. executing a forward stepping operation as a function of joystick displacement.
- **Condition-based.** Under condition-based shared control, an assistive device changes its model of operation when specific conditions are detected, e.g. obstacle detection.

The disadvantage of shared control is that it requires the end-user to expend an additional effort on top of the nervous system’s standard effort. In addition, condition-based shared control requires an in-exhaustive knowledge-base in order to account for the wide range of conditions that an assistive device may experience. One approach to overcome shared control’s limitations is the development of improved user interfaces. Neurological interfaces, e.g., Emotiv’s EMOTIV neuro-headset [13] and NeuroSky’s MindWave [44], have been used as an alternative interface for a powered wheelchair user [12]. In addition, a tongue-based interface has been presented [58].

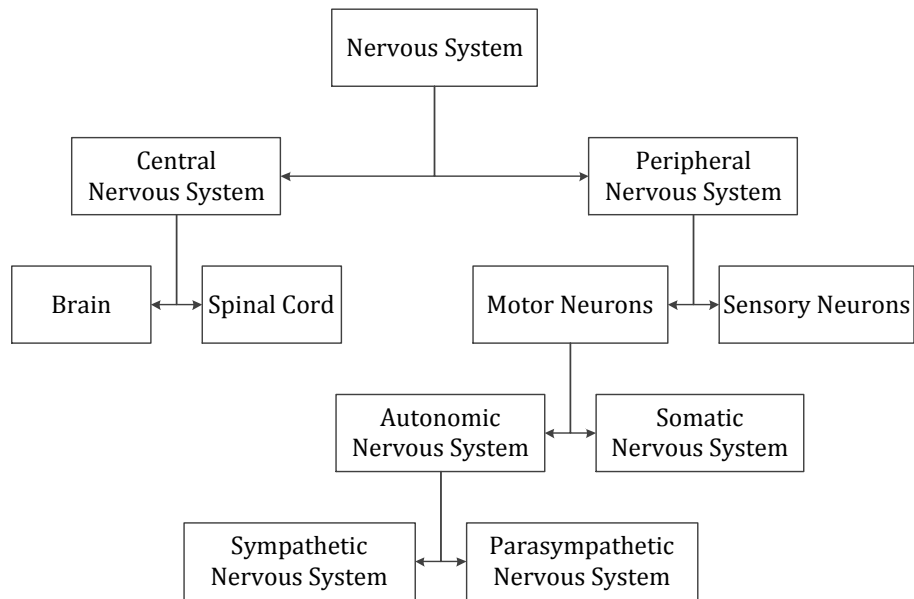


Figure 2-6: Schematic depicting the overview of the anatomical organisation of the nervous system.

2.3 Organisation of the Nervous System

The nervous system is the part of the human body responsible for maintaining homeostasis (the equilibrium of the body). The nervous system consists of the central and peripheral nervous systems (see figure 2-6). The central nervous system (CNS) is comprised of six major centres: the spinal cord, medulla (medulla oblongata), pons, mid-brain, telencephalon, and the diencephalon. The medulla and pons form the hind-brain, the telencephalon and diencephalon form the fore brain, and the mid-brain and hind-brain form the brain-stem. The peripheral nervous system (PNS) consists of afferent and efferent pathways, and their respective cell bodies, found outside of the spinal cord and the brain (see figure 2-7).

Neural pathways facilitate conduction of action potentials from one part of the nervous system to another via ascending and descending tracts. Major pathways, e.g. the spinocerebellar tract, corticospinal tract, medial lemniscus, and spinothalamic

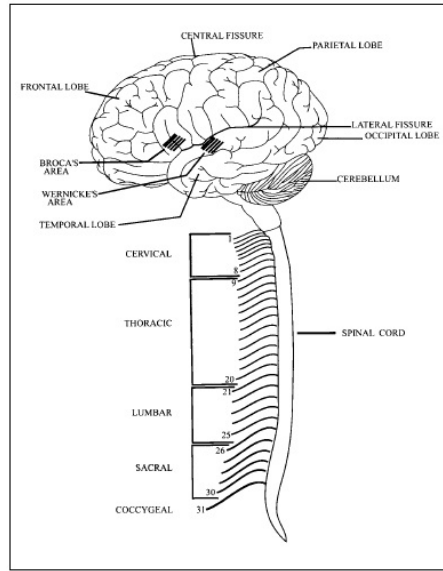


Figure 2-7: Schematic depicting the different regions of the nervous system.

tract, convey proprioceptive information from the body to the cerebellum, transmit descending motor commands, transmits cutaneous sensory information, and noxious, thermal, and proprioceptive information between the brain and the spinal cord. Voluntary movement, e.g. visually guided reaching tasks, have been shown to originate in the primary motor cortex, allowing a human to consciously control movement via the corticospinal tract. Furthermore, the reticulospinal tract has been shown to modulate motor commands generated by autonomous spinal pathways.

The brain-stem contains not only sensory nerves and motor-neurons, but also CPGs; which, have been attributed to control of rhythmic facial behaviour such as mastication and rapid eye movements [35]. In addition, the brain-stem and diencephalon contain neural networks that initiate brain-stem and spinal CPGs' rhythmic behaviour; e.g. the mid-brain's (also termed the mesencephalon) mesencephalic locomotor region (MLR) has been specified as the area which provides descending tonic signals to the spinal-cord's thoracic and lumbar CPG networks [53]. Furthermore, the brain-stem/diencephalon's Reticular formation performs a regulatory role; modulating, i.e. exciting or inhibiting, the spinal-cord's reflex networks' inter-neurons

[47]. Within the mesencephalon, the superior colliculi and red nucleus have also been attributed with contributing to motor control. In vertebrates, the superior colliculi is termed: the optic tectum and acts as sensory processing centre for visual and audio sensory information, as well as contributing to control of the retina [55].

The reticulospinal system appears to be especially important to CPGs' operation; it, alongside other descending pathways, e.g. the corticospinal pathways, modulate CPGs, i.e. speeding up or slowing down the motor pattern; suppressing CPGs, i.e. halting CPG output or inhibiting CPG activity; initiating CPGs, i.e. activating an inactive or inhibited CPG; and fraction CPG output, i.e. moderating a CPG's motor pattern over a particular phase of locomotion [55]. Furthermore, the "direct reticular neurons and spinal motor-neurons' connections play an important role in skeletal muscle control" [47]; where lesions/excitation of the reticular formation support the conclusion of importance. Evidence suggests that the reticulospinal pathway provides a medium for converting supra-spinal control centres output into motor patterns. In addition, reticular neurons have been attributed with behavioural responses to sensory stimuli, i.e. the reticular formation is an "effector apparatus that generates behavioural response to vestibular and somatic afferents" [47]. In lamprey, reticulospinal projections have been attributed with the control of posture and regulation of muscle tone [20].

Within the human spinal-cord there are four main divisions (see figure 2-7: the cervical division, which consists of 7 segments; the thoracic division, which consists of 12 segments; the lumbar division, which consists of five segments; and the sacral division, which consists of five segments too. A division's segments numbering increases rostral-caudally, i.e. top-down, e.g. c1 through to c7, T1 through to T12, etc.. Segments within the spinal-cord that control arms and legs have larger cross-sectional area than those that don't, and are termed enlargements; for example, the cervical enlargement controls the upper extremities and the lumbar enlargement controls the lower extremities. Within the spinal cord, there exist autonomous pathways that have been attributed with the rhythmic generation of motor patterns, termed central pattern generators (CPGs). Mono-synaptic projections from muscle's sensory organs terminate on the CPG's alpha-motor neuron's, constituting closed loop

control and ensuring stable actuation of a limb's joint.

Skeletal muscles are the body's actuators, contracting via myosin and actin proteins' cross-bridging. As a property of sarcomeres' Z disk-connectin bonding, muscles are elastic demonstrating compliant properties. Muscle-spindle and Golgi tendon organs give rise to the muscle's sensory primary and secondary afferents, encoding length, rate change of length, and tendon tension force, terminating via the mono-synaptic projections found within local pathways, i.e. the muscle stretch reflex. Gamma-motor neurons are responsible for biasing a muscle spindle's intrafusal muscle fibres, which via gamma-alpha co-activation provides a mechanism for the nervous system to measure muscle length and joint rotation errors. The nervous system's neurons constitute the building blocks of the nervous system. They are characterized by a soma, or cell body, which when innervated by excitatory synapses result in a sharp depolarization, termed the action potential, closely followed by a hyper-polarisation, and period of quiescence. Neurons consist of the soma, dendrites, axon hillock, and axon.

2.4 Neurons and Neuron Models

In the section, we discuss the neuron: the nervous system's functional unit, its operation, and present examples of neuron models.

The Neuron

The neuron (see figure 2.4) constitutes the nervous system's building block; it provides the input and output functions, as well as, acting as an integrator of different signals, i.e. a convergent unit upon which many other neurons terminate on. Each neuron consists of four main components: the soma, or cell body; axon, the neuron's output; axon hillock, where the axon connects to the soma; and dendrites, the axon's terminal points, which synapse upon other cells. A neuron soma's resting potential is dependent on the conductance of ion channels, e.g. sodium Na and potassium K, as well as leakage channels, e.g. chlorine Cl; which, are in turn dependent on

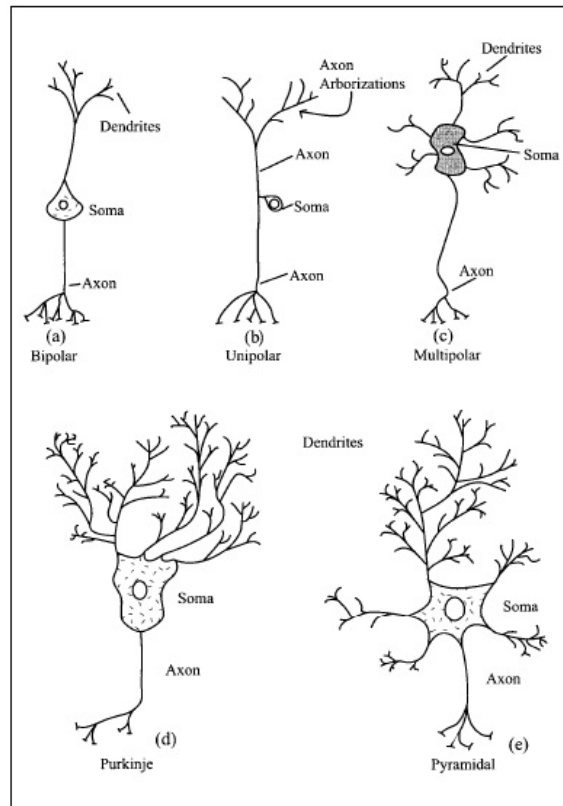


Figure 2-8: Examples of (a) bipolar, (b) unipolar, (c) multipolar, (d) purkinje, and (e) neurons.

membrane potential.

Neurons' membranes are permeable, i.e. they allow solvents, e.g. electrolytes and non-electrolytes, through. As Na^+ and K^+ ions pass through a neuron's membrane, the membrane's resting potential (typically -70 mV) is depolarised or hyper-polarised as a result. An action potential is generated once a neuron's membrane is depolarised past a threshold, e.g. -35 mV ; at which point, the membrane's voltage spikes rapidly closely followed by a hyper-polarisation and quiescent period. The permeability, i.e. the ability to allow ions to enter and exit the membrane is dependent on the membrane's potential; rather than its membrane current [24]).

When a dendrite synapses upon a neuron's soma it either depolarises, i.e. provide

excitatory input; or hyper-polarises, i.e. provide inhibitory input, the neuron. As the dendrites' synapses increase the membrane's potential, Na^+ ions enter the soma. Once the Na^+ ions cause the membrane's threshold to be exceeded, charge reversal occurs and the membrane rapidly depolarises, i.e. creates the action potential. Following the action potential, K^+ ions restore the membrane's rest potential; which results in a hyper-polarisation and quiescent period.

Neuron Models

A number of models of the neuron's spiking behaviour can be found in literature. Perhaps one of the most widely used as a means of describing neural dynamics, and providing a foundation for simplification is the Hodgkin-Huxley neuron model. Hodgkin and Huxley performed experiments on giant squid axon, mathematically modelling the activation and inactivation of ionic gating channels [24]. The neuron's membrane is modelled as a capacitor C , whose current is varied by time and membrane dependent ionic channels, e.g. sodium I_{Na} , potassium I_K , and leakage current I_L . Each channel is a function of its permeability, i.e. conductance, and potential difference, e.g. $I = g_{Na}(E - E_{Na})$; where, E is the membrane potential and E_{Na} the is the sodium channel's equilibrium potential. Fitzhugh provided a simplification of the Hodgkin-Huxley model [17]. Although Fitzhugh's model is qualitative, it does provide a significantly simpler model to simulate. Nagumo, Arimoto, and Yoshiazawa [43] demonstrate a Fitzhugh based electrical circuit consisting of a tunnel diode and "channel potential" connected in series in parallel with a capacitor and series resistor and inductor, which was similar in form to Hodgkin and Huxley's theoretical circuit [24]; was capable to generating "action potential-like" pulses.

A further reduction of the Hodgkin-Huxley neuron model is the Integrate and Fire neuron model. The integrate and fire model is the most commonly used, but it does have drawbacks, e.g. it is one-dimensional and cannot generate burst behaviour [28], which is a common behaviour demonstrated by neurons. By incorporating activation dynamics of a high-threshold potassium current, spike frequency adaptation can be achieved. In general, neuron models can be classified as either:

- **Conductance-based models.** These type of models are commonly the most complex type of abstraction found in literature. Typically consisting of complex non-linear differential equations, they provides the most biological congruent outputs; however, they are also slow to solve numerically and almost impossible to calculate analytically[53][54]. Traditionally, conductance-based neuron models have been simulated in small neural networks (i.e., less than a thousand) due to computers' computational abilities.
- **Bifurcation models.** Bifurcation models, unlike conductance-based neuron models, do not aim to model the complex ionic channels' activation and inactivation gating variables. Rather, sub-threshold dynamics are modelled using differential equations. In terms of computational requirements, they are considerably easier to simulated [27][17].
- **Threshold models.** Threshold model types treat the sub-threshold spiking behaviour of sodium and potassium ionic channels' dynamics as a hard threshold. A current injected into the neuron, or as a synaptic input, changes the membrane's potential; typically modelled as first-order integrator, generating a spike once the solution cross the, aforementioned threshold. These types of neurons are typically characterised by the generation of spike-trains.
- **Firing rate models** Firing models represent neurons in the most abstract sense; they remove any spiking mechanism, generating a "firing rate" output proportion to the spiking rate found in more complex models [39][40].

2.5 Skeletal Muscle, Models, and Engineering Parallels

In this section we discuss the structure and operation of the skeletal system's actuators: muscles; providing a reference point against which literature can be compared.

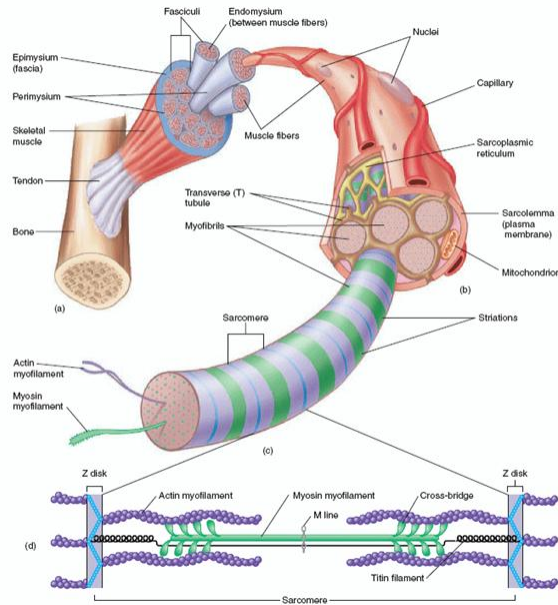


Figure 2-9: Schematic of the nervous system's skeletal muscle [60].

Skeletal Muscle Structure and Function

Skeletal muscles (see figure 2-9) develop from myoblasts that fuse to form fibres. Each muscle fibre comprises bundles of myofibrils, which house a collection of filaments, in turn consisting of sarcomeres. Within the sarcomeres, myosin and actin proteins form strands. The muscle comprises bundles of muscle fibres, with each bundle separated from others by connective tissue. Within the muscle bundles there two types of fibres: extrafusal, which attach to tendons and act upon bones; and intrafusal fibres, which play a sensory role; they contain the muscle spindle, which provides information about the muscle's length [55].

The contractile force produced by muscles is, largely, governed by two proteins: myosin, which forms the muscle's thick filaments; and actin, which forms the muscle's thin filaments. Myosin molecule's structure consists of a globular head, twisted through a neck-like structure, connected to a tail. In the ideal muscle fibre, myosin's head is cocked and separate from the actin fibres. When the muscle is innervated, actin filaments expose binding points for a myosin molecule's head to bind to. The

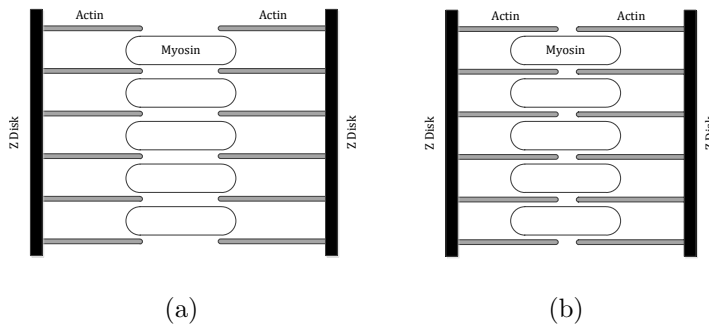


Figure 2-10: Sarcomere in a relaxed state (a), and in its contracted state (b). During contraction the sarcomere shortens as the myosin filaments pull along the rigid filaments of the actin's.

molecule's head undergoes a conformational shift, twisting up to 60 degrees and releasing stored energy [55]; not unlike a stretched spring. Myosin molecule's conformational shift causes the thick and thin filaments to move relative to each other, resulting in a contraction of the muscle's fibres and generating a tension (see figure 2-10).

The passive properties of muscles are largely due to the protein connectin (titin) found between sarcomeres, which acts as a molecular spring. The sarcomeres contain the active contractile elements' thick and thin filaments. The thin filaments connect to an intermediary structure termed the Z disk. Thick filaments also connect to the Z disk via non-contractile connectin filaments. When a muscle is innervated, the sarcomere contracts and the connectin filament shortens; when the muscle relaxes, the connectin filaments lengthens. If a muscle is stretched from rest, force is produced; not unlike a stretched spring.

The interaction of myosin and actin gives rise to muscle's force-length relationship: decreasing force as a muscle contracts. In shortened muscles, connectin and Z disk formations compress thick filaments, reducing the number of myosin heads that can bind to actin; reducing the potential force able to be produced. As the muscle lengthens, the thick filament is decompressed and more binding between myosin and actin can occur; enabling a greater force to be generated. Once muscle length exceeds the point where maximal myosin and actin binding occurs, force production

decreases. In this way, the maximum force is produced at the length where the most myosin heads can bind to actin; this is the muscle’s optimum length (i.e., in the middle of joint’s possible range of movement).

Because muscles are entirely contractile element’s, which can only generate force in one direction, the nervous system has evolved an antagonistic coupling of skeletal flexor and extensor muscles in order to effect bi-direction rotation of a limb’s joints. The extensor muscle, e.g. the triceps (triceps brachii) muscle opens the joint, increasing the angle between two consecutive limb segments. The flexor, e.g. the biceps (biceps brachii) muscle, reduces the angle measured between the two segments. Differential activation of the extensor and flexor muscles results in changes of a limb’s equilibrium, which has been proposed as a mechanism for effecting stable voluntary control [55]; however, the “equilibrium point” control hypothesis has been challenged by the idea that the brain rather uses internal models, i.e. neural representations, of limbs. Co-activation of extensor and flexor skeletal muscles has been shown to affect joint stability and compliance [55].

Hill’s Muscle Model

There exists two type of muscle models typically used for simulating muscle’s tension: Hill’s macroscopic model [22][23], and Huxley’s microscopic model [25]. In this section we present Hill’s muscle model.

The Hill-type muscle is a macroscopic representation of biological muscle’s dynamics, representing visco-elastic properties in terms of a series elastic, parallel elastic, and parallel viscous element. The model is characterized by the following equation:

$$(v + b)(F + a) = b(F_0 + a), \text{ where } b = \frac{aV_0}{F_0} \quad (2.2)$$

Where F is tension in the muscle, v , is the rate of contraction; F_0 is the maximum isometric contraction force; v_0 , the maximum velocity when $F = 0$; and a , the heat shortening coefficient. The model’s equation demonstrates that the relationship between F and V is hyperbolic: for an increase in tension, the slower the contraction; the faster the contraction, the lower the force. However, Hill’s model is only con-

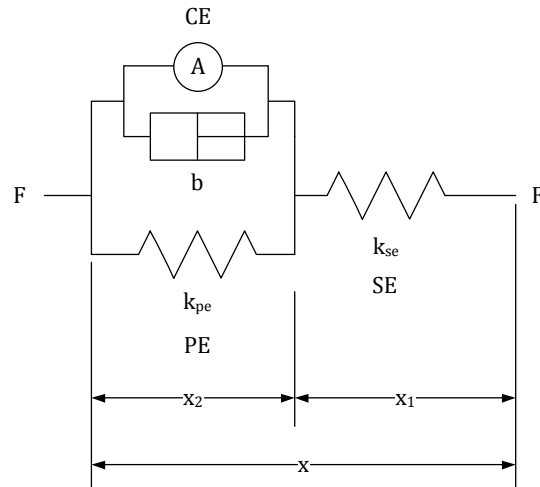


Figure 2-11: Schematic of Hill's muscle model, which illustrates the contractile element CE , the series elastic element SE , and the parallel elastic element PE .

gruent under isotonic contractions (muscle length changes, force remains the same) near the resting length.

The three-element Hill muscle model (see figure 2-11) is a representation of muscle mechanical response. The model contains a contractile element (CE), series elastic (SE), and parallel elastic (PE) element. The contractile element's active force models the myosin and actin protein's ratcheting mechanism and cross bridge recruitment. The parallel element represents the passive force of the muscle's connective tissue and has a soft tissue mechanical response. The series elastic element represents the tendon and the intrinsic elasticity of sarcomeres' connectin.

The net force of Hill's three element model satisfies the following:

$$F = F_{PE} + F_{SE} \tag{2.3}$$

$$F_{CE} = F_{SE} \tag{2.4}$$



Figure 2-12: Fabricated pneumatic McKibben actuator used in this thesis. Here, the initial muscle length $l_0 = 0.26$ m and initial radius $r_0 = 0.006$ m.

Where, the length of the satisfies

$$L = L_{PE} \quad (2.5)$$

$$L = L_{CE} + L_{SE} \quad (2.6)$$

During isometric contraction, i.e. when the muscle experience no change in length during contraction, the series elastic component is under tension and therefore stretched by a finite amount. Muscle's visco-elastic properties can be accounted for by adding the velocity dependent term:

$$F_D = \dot{L} \quad (2.7)$$

To equation (2.2).

McKibben Actuators

The skeletal muscle is inherently compliant due to thick filament's connectin; whereas, traditional actuators, e.g. DC motors, aren't. Fluidic actuators, e.g. the pneumatic McKibben muscle, provided an attractive option for actuating a wearable assistive device: they are inherently compliant due to their gas medium's compressibility; where the compliance can be varied as a function of supply pressure. McKibben muscles have been shown to be congruent with Hill's muscle model of biological muscle [23]. In addition, by having similar dynamics to those of muscles, McKibben actuators facilitate bio-mimetic control approaches by being able to compare biomimetic control performance against the biological system's. Figure 2-12 show the characteristic McKibben muscle.

The typical construction of pneumatic muscle consists of an expandable tube encased within an inextensible mesh braid. Each end of the actuator is encased in a housing with one end having an air supply inlet. As air, or a compressed medium, is inserted into the muscle, the inner cylindrical structure expands and the mesh braid's pantograph structure causes [59] causes the muscle to contract.

As the actuator contracts, the force generated decreases, i.e. it has a force-length relationship similar to biological muscles. The non-linearity of the force production has been attributed to the velocity-dependent coulomb friction effects of the mesh braiding moving relative to the inner tube. In general, McKibben muscles behaviour can be described by using either: a virtual work approach; or, a geometrical-based determination of force based on the deformation of the braid's pitch angle (i.e., the angle measured between the braid and the actuator's central axis), the braid length, and encirclements. For a braid strand of length l and n encirclements, the actuator's volume can be described by:

$$V = \frac{l^3}{4\pi n^2 \cos \theta \sin^2 \theta} \quad (2.8)$$

The maximum volume is attained at a weave angle of 54.70 degrees. When stretching, the pitch angle decreases to its minimum value, which is determined by the braid's thickness, number of encirclements, and the diameter of the muscle's inner tube. The muscle's tension is related to the weave angle by:

$$(2.9)$$

Where D_{Max} is maximum diameter of the braid angle at 90 degrees. The contraction ratio of the muscle is defined by:

$$\epsilon = 1 - \frac{l}{l_0} \quad (2.10)$$

Where l is the muscle's length, l_0 , the nominal length; and ϵ , the contraction ratio. Pneumatic muscles resemble the skeletal muscle insofar that both are contractile

elements [59], decreasing the quantity of force being generated as the muscle contracts. However, a number of differences between skeletal and McKibben muscles are evident: skeletal muscle:

- do not change volume during contraction
- have integrated length, rate of length change, and force sensors (i.e., afferent muscle spindle and Golgi tendon organs)
- do not operate using air

With respect to wearable assistive devices, an advantage of the McKibben muscle is that they are light weight and can generate large forces, i.e. McKibben muscles have large power to weight ratios. Furthermore, they can be directly connected to an assistive devices' limb without the need for transformation of the output force's modality, such as DC motor's need for step-down gearing. Their maximal force produced is often congruent with that produced with skeletal muscles', which is ideal for wearable actuator devices concerned with ensuring safe actuation of an human's limb. Lastly, McKibben muscle's compact size means that they can fit into a wide range of housings. Although McKibben muscles, and to a certain extent other types of fluid muscles [8], have been around for some time, they have not seen wide use to date [59]. Certainly, their use in wearable assistive devices has not been seen in literature, nor commercially available devices.

2.6 Muscle Sensory Organs

In this section we discuss the structure and operation of the skeletal system's sensory organs: the muscle-spindle and the Golgi tendon organ. In addition, the role gamma-motor neurons play in biasing the spindle, and subsequent effects on the spinal stretch reflex, is reviewed.

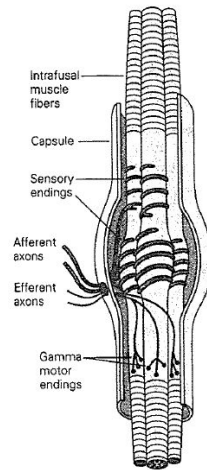


Figure 2-13: The muscle's muscle-spindle sensory organ.

The Muscle Spindle

The muscle spindle (see figure 2-13) is a structure of fine intrafusal muscle fibres that taper at their ends, termed "poles", and contain a fluid-filled capsule at their center [55]. Muscle spindles are fusiform in shape and widely scattered in the fleshy bellies of skeletal muscles [16]. Sensory fibres wrap around the intrafusal fibres within the capsule and serve as transducers of muscle length [29][16].

In the intrafusal fibres the contractile region is limited to its poles, which receive innervation from gamma-motor neurons. Primary muscle-spindle afferents innervate the central region (the nuclear bag) [29]; secondary afferents innervate the poles. Because the intrafusal muscle fibre lies in parallel to the extrafusal muscle, they change length together. However, the two kinds of muscle-spindle afferent encode this length change differently. Primary muscle-spindle afferents respond strongly to a stretch but decrease activity once stretching ends, i.e. primary afferents encode velocity. Secondary muscle-spindle afferents respond to the change in length with increased activity, which is maintained after stretching, i.e. secondary afferents encode length.

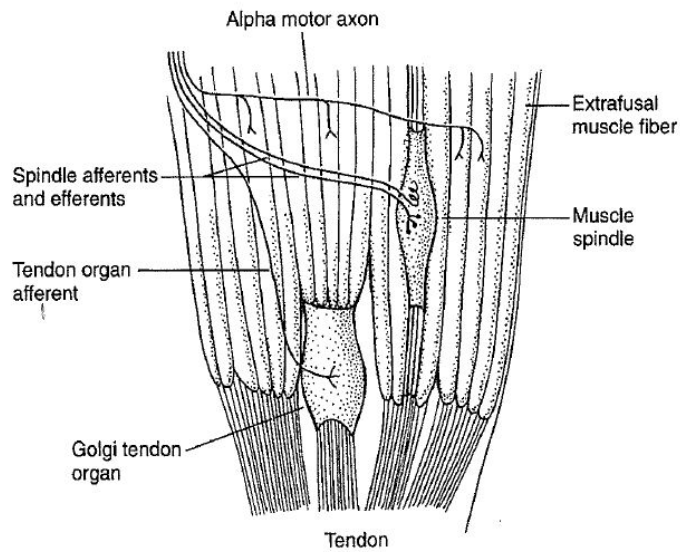


Figure 2-14: The muscle's muscle-spindle sensory organ.

Golgi Tendon Organ

The Golgi tendon organs (see figure 2-14) are located between extrafusal muscle fibres and tendons. The muscle fibres attach to the organ's proximal end, and the distal end attaches to the tendon. Within the organ, type Ib afferents intertwine with collagen fibres. When the Golgi tendon organ is stretched, the collagen deforms the Ib afferents' endings, producing action potentials and encoding force as a firing-rate.

Gamma-motor Neuron

The gamma-motor neuron contracts the muscle-spindle, in effect biasing the muscle-spindles afferent's firing rate in the presence of stretch. In the absence of gamma-motor neurons, the spindle's length change would be equal to the extrafusal fibres'. By being able to change the muscle-spindle's length, the CNS has evolved a mechanism for measuring error between $\alpha - \gamma$ coactivated extrafusal and intrafusal muscle fibres. If muscle contraction is less than that predicted by the gamma-motor neuron's degree of activation, the spindle's afferent fires; if the muscle's contraction is greater

than predicted, the muscle spindle's primary afferent's firing rate decreases.

The Myotatic Stretch Reflex

A number of networks in the spinal cord that mediate sensory motor reflexes have been found [29][42]; the most widely documented being the stretch reflex (or the myotatic reflex). The stretch reflex provides direct excitatory feedback to the motor neurons innervating the muscle that has been stretched. The sensory signal for the stretch reflex originates in muscle spindles, the large-diameter sensory fibres (nuclear bag fibres [16]) allow for very rapid adjustments in this reflex arc when the muscle is stretched. The stretch imposed on the muscle deforms the intrafusal muscle fibres, which in turn initiate action potentials by activating mechanically gated ion channels in the afferent axons coiled around the spindle. The centrally projecting branch of the sensory neuron forms mono-synaptic excitatory connections with the alpha-motor neurons in the ventral horn of the spinal cord that innervate the same muscle and, via local circuit neurons, inhibitory connections with the alpha-motor neurons of antagonistic muscles. This reciprocal innervation results in rapid contraction of the stretched muscle and simultaneous relaxation of the antagonist muscle. All of this leads to especially rapid and efficient responses to changes in the length or tension in the muscle.

2.7 Pattern Generating Pathways and Models

In this section we discuss central pattern generators (CPGs): autonomous neural pathways found within the spinal cord, which have been attributed with the generation of rhythmic, stereotyped motor pattern, which elicit a wide range of locomotion; including, but not limited to, walking, running, swimming, and flying. In addition, CPGs have also been shown to generate motor patterns for mastication.

Central Pattern Generators

A central pattern generator is a type of neuronal network capable of generating a rhythmic pattern of motor activity in the absence of sensory input from peripheral receptors [29]. CPGs responsible for locomotion have been identified as existing in the mammalian spinal-cord; however, CPGs have also been identified in over 50 different rhythmic motor systems, including those controlling swimming [20], walking, breathing, feeding, mastication [63] and flying [29]. However, the term "central pattern generator" refers to a function, not a circumscribed anatomical entity: the individual neurons that constitute the CPG may in principle be located in widely separate parts of the central nervous system [19].

Most CPGs produce a complex temporal pattern of activation of different groups of motor-neurons. The pattern can be divided into a number of distinct phases; even within a phase the timing of an activity can vary in different motor-neurons [54]. The sequence of motor-neurons is regulated by a number of mechanisms; including, mutual inhibition; where inter-neurons that fire out of phase with each other are reciprocally coupled by inhibitory connections, and mutual excitation; which is important for establishing synchronous firing of a group of neurons [29].

While the organisation of CPGs is largely unknown, Thomas Graham Brown [5][6] described how isolated spinal-cord in de-cerebrate and deafferented cats can generate patterns of activity that resembles that generated during motor behaviour, e.g. walking, in the absence of sensory inputs [64], and as a result, provided the first conceptual scheme of the mammalian CPG based on a "half-centre" approach; where, rhythmic behaviour results from the mutual inhibition of two excitatory "half-centres". In Graham Browns' architecture each "half-centre" controlled the rhythm and pattern of motor-neuron activity.

Pattern generators are not isolated entities; rather, they're interconnected circuitry that overlaps in the behaviours that they control. Interaction between CPGs has been approached from two points: one, the shared CPG perspective, where locomotor network consists of distinct spinal CPGs that are activated for selective control of a joint's muscles; two, the share inter-neuron perspective, where complex

movements are configured from pools of inter-neurons. For example, coordinated movement of a limb could be achieved by phase-dependent interaction of different CPGs, or by using a combination of synaptic processes to “sculpt” a desired motor pattern [37]. Perhaps the most compelling of evidence that the spinal-cord’s CPGs are intrinsically able to generate a rhythmic motor pattern stems from fictive locomotion studies; where, the spinal-cord is removed from an animal and placed in a physiological saline [38], such as Grillner did in his study of the lamprey [20]. Fictive locomotion is typically recorded at the ventral roots of the spinal-cord’s grey matter; however, in order to evoke fictive locomotion, neuro-modulators found in descending pathways, e.g. the reticulospinal pathway, are required [38]. Based on lamprey’s evoked fictive locomotion, Grillner concluded the ability to generate coordinated activity, with appropriate phase lag, is distributed along the lamprey’s spinal-cord, i.e. when divided, spinal segments retain the ability to generate alternating activity.

Studies of central pattern generating networks in invertebrates and vertebrates have shown that intrinsic membrane properties of the neurons that constitute CPGs are crucial for understanding the mechanisms of pattern generation [38]. Some neurons fire bursts of actions potentials, either endogenously or in the presence of neuro-modulatory substances. Strongly oscillatory neurons provide timing inputs for circuits; however, when too oscillatory, it can be difficult to inhibit or rest their activity; thus, strong and intrinsically oscillatory neurons are rare. Some neurons are bi-stable and generate plateau potentials that are triggered by a depolarising, excitatory pulse and terminated by a hyper-polarising, inhibitory pulse. Plateau potentials can maintain a state based on their last synaptic input. An innate property of motor systems is their ability to be modified, e.g. in fish, their spinal-cord not only coordinates segmental phase lag but also the direction of locomotion, i.e. forward and backward swimming. Rather than have two independent networks, it’s likely that the same CPG is used; however, different coordination inter-neurons dominate during different directions. In tetrapods, the need to modify limb coordination with varying gaits, e.g. walking, trotting, and galloping; requires different sets of coordination neurons to combine the CPG in different phase relations. For an individual limb, the motor pattern must be flexible; Grillner [21] proposed each limb is controlled by a separate

CPG; however, each limb CPG consists of a number of “unit CPGs”, which control a group of synergistic muscles. Neuro-modulators activate, modify, and terminate central pattern generators; CPGs receive multiple and parallel inputs so that they can be activated a number of ways. Modulators alter the strength of synapses and intrinsic membrane properties; modulating motor patterns [38]. There is evidence that neurons may switch from one network to another; moreover, evidence suggests that a large network can be reconfigured to produce a number of related behaviours, e.g. breathing and gasping.

Although, as discussed, pattern generators may generate characteristic motor patterns in the absence of afferent feedback, i.e. fictive locomotion; afferent information plays an important role in adjusting locomotion’s motor pattern. Certainly, afferent feedback from muscles’ spindles, e.g. groups and afferents, are necessary in order to facilitate the mono-synaptic stretch reflex and maintain limb stability [32][33]. Activation of extensor group afferents, e.g. those in the ankle, result in strong excitation of extensor motor-neurons; which in turn contribute to stance-phase extensor activity [54]. In addition, activity in extensor group afferents also contribute to the transition from stance to swing; entraining the step cycle period. Furthermore, cutaneous reflexes also play an important role in locomotion’s control; for example, cutaneous afferents during extension enhance the extension motor-neurons’ activation, prolonging the extension phase. The same excitation during flexion results in premature initiation of extension [54].

Supra-spinal centres, sensory afferents, and neuro-modulators modulate CPGs so that rather than produce stereotyped motor patterns, CPGs produce flexible, adaptive patterns. Neuro-modulators enhance or diminish the effects of synapses’ neurotransmitters; altering the functionality of neuronal circuits [37]. Certainly, “sensory feedback, elicited during gait, acts directly on the CPG to aid phase transition” [65]; further, the short loop reflex, i.e. the - monosynaptic connection is dependent on the spindle’s afferent input. Sensory feedback also contributes to the CPG’s support of onset of vertebrate’s locomotion’s swing phase; where, when the leg’s loading reduces extensor feedback is reduced [54]. Further, as discussed, much of CPGs’ research has focussed on de-cerebrate/decorticate/deafferented animals; however, of

particular interest is the new born human: descending control is not yet developed fully, yet stepping occurs in the absence of mature corticospinal connections; rather, infant stepping is an example of a sensory evoking reflex driving locomotion example [65].

As discussed, Graham Brown [5][6] demonstrated the cat’s spinal-cords ability to generate rhythmic activity in the absence of MLR activation and afferent feedback. Graham Brown’s proposed general “Half Centre” model is widely accepted; forming the basis of many CPG models, e.g. Lundberg’s [36]. The half-centre paradigm’s key points are: a limb is controlled by a separate CPG; each CPG contains two excitatory neurons; each neuron is mutually inhibited, each neuron possesses a “fatigue” function; and phase shifting is a function of the neurons’ excitability, where, when a neuron’s excitation reduces below a threshold, the contra-lateral neuron is released from inhibition. However, a general problem with this architecture is that it only accommodates a strict alternating pattern of flexion and extension; further, during locomotion co-activation of muscles is evident, which, as discussed, contributes to limb stability. Graham Brown’s architecture fails to accommodate this behaviour.

Lundberg [36] improved upon Graham Browns model by incorporating inter-neurons that shape the bi-phasic nature of the motor-neurons’ activities. However, Lund’s model still contains the underlying principles that prevent Graham Brown’s from explaining complex patterns, e.g. the ability to maintain rhythm in the presence of decreasing motor-neuron activity.

McCrea and Rybak stipulated Graham Browns model’s problem lies in the half-centre’s organisation [41]. In the half-centre, the excitatory neurons drive the motor-neurons directly; thus, any change in the half-centre correlates to a change in the alpha motor-neurons. Graham Brown’s architecture is disadvantageous for individual control of extensor and flexor motor-neurons; in his model they are tied together via the half-centre’s mutual inhibition. Orlovsky, Deliagina, and Grillner proposed additional inter-neurons interact with the motor-neurons [46]. In their model the additional inter-neurons assist the half centre in generating motor-neurons’ activation pattern, arising from afferents, e.g. type Ia, Ib, and II. The addition of a further motor-neuron controlling inter-neuron is beneficial: motor-neuron activity can be

controlled independently of the half-centre’s rhythm generation. However, the improved “flexibility” of the neural network [41] fails to explain biological phenomenon, e.g. reflexes and afferents’ ability to control the activity of the motor-neurons; thus, Orlovsky, Deliagina, and Grillner’s model isn’t complex enough.

Furthermore, single layer architectures, like Graham Brown’s, fail to explain non-resetting deletions: burst of motor-neuron activity absent for a number of motor, during fictive locomotion [54]. During deletions, activity fails simultaneously in multiple synergistic motor-neuron pools and becomes tonic in multiple antagonists. McCrea and Rybak stipulated this suggests deletions reflect changes in a network common to all motor-neurons, e.g. the CPG, and are not the results of neuron inhibition. Further, after deletions a motor-neuron’s activity returns to normal; reappearing without a phase shift in the motor pattern. Clearly, in the single layer architecture if there is a deletion in a neuron’s activity, the contra-lateral neuron is released from inhibition; resulting in a phase shift – contrary to physiological phenomenon.

Rybak et al.’s Model

Rybak, Shevtsova, Lafreniere-Roula, McCrea [54] proposed their own two-level CPG model, which activated a limb’s antagonistic muscles via a rhythm generator (RG) and pattern formation layers (PF) (see figure 2-15). The RG layer consisted of extensor and flexor neuron populations, which set the corresponding muscles’ firing rate and as a result the effected motor pattern’s extensor and flexor rhythm. The RG networks controlled the subsequent PF layer’s network, which distributed and coordinated the activity of alpha-motor neurons and motor neuron pools (MN).

Reciprocal inhibition between the RG and PF layers’ extensor and flexor neuron populations ensured that a given MN population was only active during a specific phase of the elicited motor pattern’s cycle. The model’s neurons were modelled using the Hodgkin-Huxley conductance-based paradigm; however, Rybak et al. included a slowly inactivating sodium current in addition to the standard sodium and potassium ion channels; the advantage of which ensures RG layer populations possessed bursting properties. Their model was able to reproduce a number of aspects observed during

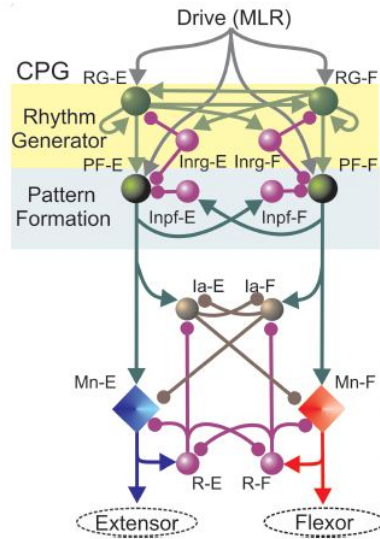


Figure 2-15: Rybak et al.'s dual layered, rhythm generator and pattern formation central pattern generator model.

fictive locomotion; including, the ability to evoke rhythmic locomotion as a function of descending activation, which was attributed to the mesencephalic locomotor region (MLR), and synchronization of extensor and flexor populations in the absence of synaptic inhibition.

An important feature of Rybak et al.'s model is the ability to separate cycle timing and motor activation. The separation of RG and PF allows for a simple explanation for deletions [54]; where, inhibition or excitation of the pattern formation's neurons does not affect the rhythm generation layer. Specifically, a decrease in the PF extensor population's excitability causes a deletion in motor-neuron activity; however, the RG layer maintains the CPG's rhythm, ensuring the PF-level's phase is retained [41]. However, if the pattern formation's extensor population is excited, the contra-lateral flexor population's motor neuron is inhibited, maintaining the extensor's phase.

Of particular interest is Rybak, Shevtsova, Lafreniere-Roula, and McCrea's model's ability to be entrained to an external rhythmic movement, e.g. if the arm was at-

tached to a handle that rotated about its centre. Due to the RG layer’s internal rhythmogenic populations, i.e. because of the extensor and flexor RG layers populations’ internal bursting properties; afferent feedback will depolarise the populations enough for the populations’ inter-neurons to fire, thus creating a general rhythm based on the frequency of the applied mechanical stimulus. While, Rybak, Shevtsova, Lafreniere-Roula, and McCrea’s research’s onus was targeted towards the architecture of the network, it is argued that the RG layer in concert with flexor and extensor reflex will assist the limb’s movement.

Matsuoka’s Model

In contrast to Rybak et al.’s model’s complexity and biological relevance, Matsuoka proposed a pattern generator based loosely on Graham Brown’s half-centre oscillator [5][6], opting to model neurons’ firing rates: abstractualising neuron intracellular dynamics. Essentially, Matsuoka’s CPG constitutes a coupled non-linear oscillator, where the term CPG has been borrowed from the biological domain, rather than representing a specific pathway of the spinal cord. Classical examples of coupled non-linear oscillators include those developed by Van del Pol [61], Hopf [57], and Rayleigh [49].

Matsuoka’s CPG consists of two reciprocally connected, mutually inhibited neurons (see figure 2-16). Each of the neurons were modelled as a set of coupled first order differential equations, which mimicked neuron’s firing rate adaptation [39][40] as a fatigue function. Briefly, the governing equation of the Matsuoka neuron is given by:

$$\tau \dot{u}_i = -u_i - \beta v_i + \sum_{j=1}^n w_{ij} y_{ij} + u_0 + \text{Feed}_i \quad (2.11)$$

Where u_i is the neuron’s inner state of the i^{th} neuron; v_i , the degree of adaptation; y_i , the output of the i^{th} neuron; u_0 , the external input; Feed_i , the feedback signal; and β , the degree of adaptation.

In contrast to Rybak et al.’s model, Matsuoka’s pattern generator has found wide use in controlling biological inspired robots, e.g., mastication robots [63].

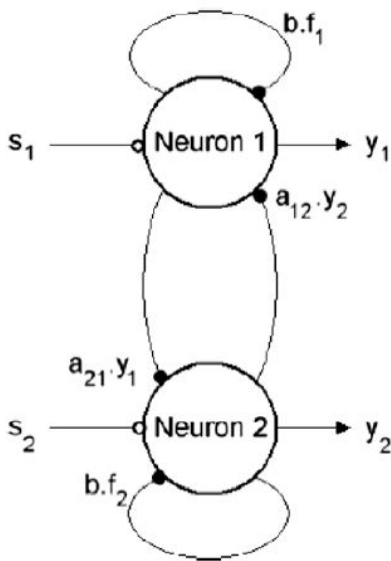


Figure 2-16: Schematic of the Matsuoka’s reciprocally connected, mutually inhibited neurons, central pattern generator.

2.8 Summary

In this review, the current state of wearable assistive device technology has been presented. Classification of different assistive devices show a clear trend for traditional devices to be passive and non-compliant; however, a powered exoskeletons have, in recent times, become a popular medium for providing active assistance.

The hierarchy and organisation of the nervous system and its separation into the peripheral and central nervous systems has been discussed. Particular import was placed on descending pathways; where, the corticospinal and reticulospinal tract’s have been identified as playing significant roles in voluntary motor control and modulation of the spinal cord’s locomotion pattern generator.

Within the central nervous system’s spinal cord, functional pathways, termed central pattern generators, have been identified and discussed. Rybak et al.’s dual layered, reciprocally inhibited model of the locomotor has been found to be the most up-to-date CPG model, describing a number of biological phenomenon. We have discussed and identified some of its advantages over classical models, such as

Graham Brown's half-centre oscillator.

Following discussion of pattern generators, we have reviewed the operation of skeletal muscles, and muscle sensory organs: the muscle spindle and the Golgi tendon organ, as well as the role gamma-motor neurons play. Hill's muscle model has been reviewed with key elements discussed. Subsequently, bio-mimetic McKibben fluidic muscles and their operation has been discussed. McKibben muscles have been found to agree with Hill's muscle model, and present an attractive option for assistive device actuation due to their compliance.

In order to seat the literature pertaining to the nervous system, the neuron: the smallest functional unit of the peripheral and central nervous systems, has been reviewed and its operation discussed. Neuron models have been classified based on their realism, with a number of models discussed.

This review has provided a complete review of a wide range of literature, describing the extremely wide scope of the research. Key conclusions are presented below:

- Current wearable assistive actuator technologies are not novel, i.e. they still utilize DC motors; as such, they lack compliance.
- The brain is responsible for generating motor plans; however, it is the spinal cord that effects the corresponding movement.
- The spinal cord contains functional neural pathways termed central pattern generators (CPGs); which, generate motor patterns as a result of descending activation (e.g. descending MLR innervations).
- Rybak et al.'s CPG model is the most recent and subsequently up-to-date model of the locomotion generating spinal pathway, overcoming the limitations of Graham Brown's half-centre oscillator (HCO).
- Skeletal muscles are the nervous systems' compliant actuators, whose force-length properties are described by Hill's muscle model. Pneumatic McKibben muscles are engineering parallel of the biological muscle and have been shown to agree with Hill's muscle model's dynamics

- Neurons constitute the nervous system's functional unit; forming the basis of the central pattern generators found within the brain-stem and spinal cord. Reciprocal connection, mutual inhibition of two neurons has been shown to elicit rhythmic activity.

Chapter 3

Hill's Model, Parametric Variation, and Antagonistic Actuation

In this chapter, this thesis presents Hill's three element muscle model [23]; evaluating parallel and series viscous and elastic elements' effects on the production of a skeletal muscle's force. In addition, this chapter investigates the role active contractile forces play in antagonistically producing movement and varying a joint's compliance. Section 3.1 identifies the importance of modelling muscles, reiterating their organisation, discussing the mechanism of force production, and introduces Hill's phenomenological approach to modelling muscle dynamics. Section 3.2 presents Hill's three element model. Section 3.4 discusses the methodology used in this chapter. In section 3.5, Hill's muscle model is fitted to the ramp stretch response of the soleus muscle. In section 3.6, the chapter's parametric analysis of an implemented Hill-type soleus muscle model is presented, summarising key parameters' effects on muscle tension. In section 3.7, an antagonistically coupled pair of the soleus muscle models are presented; demonstrating the role active contractile forces play in differential and coactivation of a joint's muscles. Section 3.8 closes the chapter, discussing key conclusions.

3.1 Introduction

Skeletal muscles can be thought of as the nervous system's actuators, effecting joint rotation through antagonistic coupling. An important aspect of understanding how they effect compliant and adaptive movement is being able to model them. Literature review has identified two key models: Huxley's micro-sscopic model [25], and Hill's macro-sscopic model [23]. In terms of this thesis, the objective is to replicate qualitatively the behaviour of the nervous system; therefore, modeling force production as a function of myosin and actin cross-bridging exceeds requirements, therefore making Hill's model ideal.

The skeletal muscle is a complex system and in order to interpret how it works, it is necessary to understand how it is organised. Muscle is wrapped in a dense connective tissue, which joins with the tendon. The muscle consists of fiber bundles, termed fascicles, which are also separated from each other by connective tissue. Each muscle fiber consists of parallel bundles of myofibrils; where, each myofibril is made up of series of contractile elements, termed sarcomeres. These sarcomeres generate contraction via myosin and actin cross-bridging, whose force is transferred to the tendon.

Contraction is controlled by the central nervous system; action potentials originate from the spinal-cord's alpha-motor neurons, travelling along their axons, and terminating on muscle fibers. When the spikes innervate a muscle fiber, calcium flows into the myofibrils' sarcomeres, which in turn causes their filaments to slide relative to each other, as per Huxley's cross-bridging theory [25]. During contraction, the myosin proteins' globular heads twist and bind with the actin filament, exerting force upon the thin filaments, causing the sarcomeres to shorten and the muscle to contract. The muscle's contraction can be categorised by either its length change or the force produced: under isotonic contraction, the muscle's length changes; whereas, under isometric contraction, the length stays the same and force increases.

To quantify a skeletal muscle's force production, Hill performed experiments on isolated muscle fibers [23]. The fibers were attached to a bar that pivoted about a point; where, one end of the bar had a catch mechanism and the other held a weight.

Initially the muscle was maximally excited and the bar held in place (i.e., under isometric conditions). Once the catch was released, the muscle was loaded, and its length changed (i.e., isotonic contraction). Hill observed an immediate reduction in tension and length, followed closely by a gradual shortening. He reasoned this sharp change in length was due to a "series elastic" element; whereas, the slow change was due to an elastic element acting via a viscous component, the "parallel elastic" and "parallel damping" elements, respectively. This parallel and series viscosity and stiffness composes the muscle's passive properties. In terms of active force, Hill noted that innervated muscle produces more force when held isometrically, which reduced as the muscle shortened. Furthermore, Hill observed that tension reduced as the rate of contraction increased. He reasoned that this behaviour was due to a "resistive force"; analogous to a mechanical damper, which could be accounted for by the parallel damping element.

In the following section, this thesis presents Hill's three element model's governing equations, relating force to muscle length and rate of length change.

3.2 Hill's muscle model

Hill's muscle model described the tension within the parallel and series elements by:

$$T = k_{se}(x_{se} - x_{se}^*) \quad (3.1)$$

$$T = k_{pe}(x_{pe} - x_{pe}^*) + b\dot{x}_{pe} + A \quad (3.2)$$

where A represents the muscle's active force component, x_{se} and x_{pe} , the muscle's parallel and series elements' lengths; \dot{x}_{pe} , the rate of change of the parallel elements' length; b , the muscle's viscous damping; and T , the muscle's force. Here, $*$ is used to represent the parallel and series elements' nominal lengths. Because the length of the muscle is the sum of the parallel and series elements' lengths, the total length is

expressed by:

$$x = x_{se} + x_{pe} \quad (3.3)$$

$$x^* = x_{se}^* + x_{pe}^* \Rightarrow x - x^* = (x_{se} - x_{se}^*) + (x_{pe} - x_{pe}^*) \quad (3.4)$$

Substituting $(x_{pe} - x_{pe}^*)$ into equation (3.4), we get:

$$T = k_{pe}(x - x^*) - k_{pe}(x_{se} - x_{se}^*) + b\dot{x}_{pe} + A \quad (3.5)$$

Solving equation (3.3) for $(x_{se} - x_{se}^*)$ and noting $\dot{x}_{pe} = \dot{x} - \dot{x}_{se}$, substitution into the previous equation results in the following:

$$T = k_{pe}(x - x^*) - k_{pe}\frac{T}{k_{se}} + b(\dot{x} - \dot{x}_{se}) + A \quad (3.6)$$

which, for the following relationship:

$$x_{se} = \frac{T}{k_{se}} + x_{se}^* \Rightarrow \dot{x} = \frac{T}{k_{se}} \quad (3.7)$$

results in the muscle's force-length characteristic equation:

$$T = k_{pe}(x - x^*) - k_{pe}\frac{T}{k_{se}} + b\left(\dot{x} - \frac{\dot{T}}{k_{se}}\right) + A \quad (3.8)$$

Solving equation (3.8) for \dot{T} , the rate of change in the muscle's force can be expressed as:

$$\dot{T} = \frac{k_{se}}{b} \left[k_{pe}(x - x^*) + b\dot{x} - \left(1 + \frac{k_{pe}}{k_{se}}\right) T + A \right] \quad (3.9)$$

The following section describes the process for determining the properties of muscles.

Figure 3-1: Picture is a schematic of Hill's muscle model. The model consists of a series elastic element, k_{se} ; parallel elastic element, k_{pe} ; and active force component, A . The active force generated within the model is a function of innervations; great levels of activation result in an increased force component acting across the parallel elastic and viscous elements.

3.3 Determining muscle's properties

In terms of force production, the muscle's tension is dependent on the stimulus' magnitude; for example, weak innervation results in an isometric twitch, and maximum activation results in tetanus - maximum sustained force production - occurs. During tetanus, if a muscle is stretched, the series elastic element's stiffness k_{se} , and subsequently k_{pe} and b , can be determined. According to Hill [23], the series elastic element k_{se} is responsible, since force due to activation A was at a maximum prior to the stretch. The series elastic elements stiffness therefore is determined by:

$$k_{se} = \frac{\Delta T}{\Delta x} \quad (3.10)$$

where, ΔT is the change in the muscle's tension, and Δx is the change in length used to elicit the change in tension. After stretching the muscle, the time response of the muscle's force decays to a steady state value. Comparing the force before and force after can be used to solve for k_{pe} . From equation 3.8, we have tension before the stretch equal to:

$$T_b \left(1 + \frac{k_{pe}}{k_{se}} \right) = k_{pe}(x_{se} - x^*) + A \quad (3.11)$$

where T_b is the force in the muscle before. After the stretch, we have:

$$T_a \left(1 + \frac{k_{pe}}{k_{se}} \right) = k_{pe}(x_{se} - x^*) + A \quad (3.12)$$

where T_a is the muscle's force after the stretch. The corresponding change in force therefore is equal to

$$\Delta T \left(1 + \frac{k_{pe}}{k_{se}} \right) = k_{pe}\Delta x \quad (3.13)$$

Expressing the previous equation in terms of $\Delta x/\Delta T$ results in the following relationship:

$$\frac{\Delta x}{\Delta T} = \frac{k_{se} + k_{pe}}{k_{se}k_{pe}}, \quad (3.14)$$

from which the parallel elastic element's stiffness can be determined from the following:

$$k_{pe} = \frac{k_{se}}{\frac{\Delta x k_{se}}{\Delta T} - 1} \quad (3.15)$$

In order to determine the parallel viscous element's damping coefficient, it is necessary to consider the muscle tension's transient response to the stretch. At the time the stimulus is applied t_n , the tension T and tensions' rate of change \dot{T} in the muscle is given by:

$$T(t_n) = k_{se}\Delta x + A \quad (3.16)$$

$$T(t) = \frac{k_{se}}{b}(k_{pe}\Delta x + A) - \frac{k_{se}}{b} \left(1 + \frac{k_{pe}}{k_{se}}\right) T(t) \quad (3.17)$$

$$(3.18)$$

the solution of which is given by the following:

$$T(t) = \frac{k_{se}(A + k_{pe}\Delta x)}{k_{se} + k_{pe}} + \left[\frac{k_{pe}A + k_{se}^2}{k_{pe} + k_{se}} \exp\left(-\frac{k_{se} + k_{pe}}{b}t\right) \right] \quad (3.19)$$

Given the exponential term's form is $\exp(-t/\tau)$, the time constant of the transient response can be solved by determining the point where the transient response has reduced by approximately 63%.

3.4 Methodology

In implementing Hill's model, this thesis has evaluated the qualitative behaviour of skeletal muscle. In the following sections, an implementation of Hill's three element model fitted to the ramp stretch response of a feline's soleus muscle is presented.

Based on the experimental results of Lin's work [34], the theory of section 3.3 has been applied and, for a 4.00 mm ramp stretch applied at 100 mm/sec, the series elastic, parallel elastic, and parallel damping elements' default values determined.

Following that, two simulated studies that have been carried out are presented. In the first case, an isolated soleus muscle's parallel and series elements were independently varied from 0 % and 100 % of their default values. For the first section of simulation, inactive isotonic conditions were replicated; where, for an active force of 0 N, a 4.00 mm ramp stretch was applied at 100 mm/sec. In the simulation's second section, active isotonic conditions were replicated; where, for an active force of 10 N, the same ramp function was applied.

In the second simulated study, the implemented soleus muscle was coupled antagonistically; where, for the purpose of simulation, a "fore-limb" modelled as a critically damped pendulum of mass 0.30 kg and length 0.35 m has been used. In the first part of the simulations, the extensor and flexor muscles receive a difference in active force, termed "differential activation". The extensor's active force was increased from 10 N to 50 N, while the flexor's active force was held constant at 10 N. In the simulation's second part, both the antagonistic muscles' active forces were incremented equally, termed "coactivation". For an active force increasing from 0 N to 2.00 N, both a constant and 100 ms pulsed 10 N load was applied distally and the joint angle's transient response recorded.

3.5 Muscle Parameter Fitting

In this thesis, Hill's muscle model [23] was implemented in MathWorks' Simulink environment. In order for the Simulink model's output to be congruent with the biological muscle's generation of tension, special care was applied to the muscle model's rate of change \dot{x} . It was ensured that step changes in length were prohibited. The reasoning for this was that if x is discontinuous, the derivative will tend towards infinity. The consequent action on the muscle model's tension is for the damping coefficient to dominate the solution, leading to (generally) an incorrect, negative, tension output. To prevent this, we have limited the change in length to continuous

Table 3.1: Hill-type muscle model parameters used during simulation.

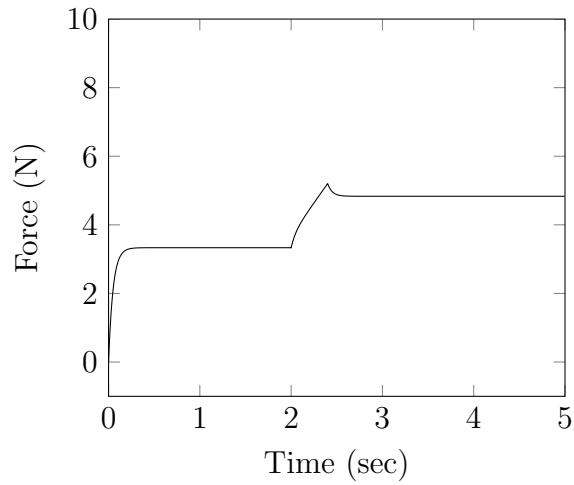
Parameter	Value	Units
k_{se}	1125.00	N/m
k_{pe}	562.50	N/m
b	83.38	Ns/m

signals only. For near step-like changes in length, we used the ramp function $r(t)$, with the slope tending towards, though not equal to, infinity. In addition, k_{se} and b are required to be a non-zero values to ensure Simulink model integrity. With respect to the muscle’s active force component, discontinuous signals do not cause the model to become non-congruent; as such, the nature of the active force component signal has not been constrained. Finally, the muscle’s active force component A is restricted to a positive only signal.

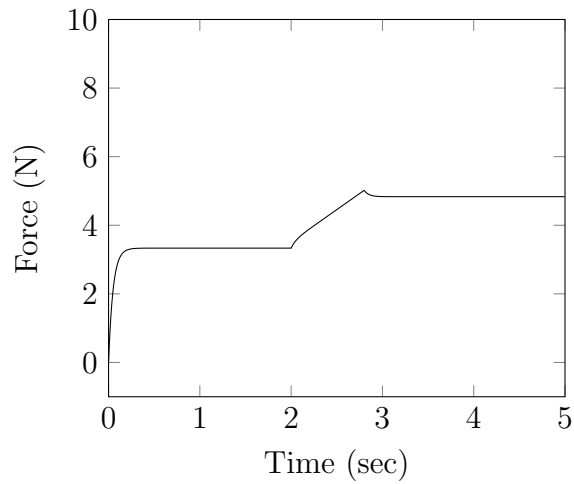
The simulated muscle model parameters were determined based on the results of ramp stretches of the cat (*felis catus*) soleus muscle, where a 4.00 mm ramp stretch function was applied at 100.00 mm/s and 20.00 mm/s rates [34]. Initial activation of the soleus muscle resulted in a nominal force of 5.00 N; which, rose to, approximately, 9.50 N and 7.50 N per the respective stretch functions. Peak force rate of change dF/dt values of, approximately, 500.00 N/s and 100 N/s were observed. The corresponding steady state values were 6.5 N and 5.5 N.. Based on the response plots in [34], the series elastic element’s stiff was found to be 1125.00 N/m, as such the parallel element’s stiffness was found to be 562.50 N/m, and lastly the parallel viscous element’s damping coefficient was found to be 83.38 Ns/m (see table 3.1). Figure 3-2 shows the muscle model’s tension as a function of the 100 mm/s and 20 mm/s ramp functions being applied at time $t = 2$ sec.

3.6 Passive and Active Muscle Parameter Analysis

In order to determine the series and parallel elastic (k_{se} and k_{pe}) and viscous (b) parameters’ effects on Hill’s muscle model’s passive behaviour, they were indepen-



(a)



(b)

Figure 3-2: SIM Response of the modelled Hill muscle's tension to a ramp input of (a) 100 mm/s and (b) 20 mm/s applied at time $t = 2$ sec and held constant for the remainder of the simulation. In this example $k_{se} = 1125.00$ N/m, $k_{pe} = 562.5$ N/m, and $b = 83.38$ Ns/m and the active force component $A = 5$ N.

dently varied from 0 % to 100 %, in 20 % incremental steps, of their default values. First, inactive isotonic conditions; where, the muscle's active force was 0 N, were considered. For a 4.00 mm ramp stretch applied at 100 mm/sec, the parameters' effects are summarised below:

- **Series stiffness k_{se} variation.** In determining k_{se} 's effect on the model's output, k_{pe} , b , and A were held constant. Generally speaking, the series elastic element acts as the muscle tension's gain, multiplying the body of equation (3.9) (see figure 3-3(a)). For k_{se} approaching 0, the muscle model's tension is numerically equal to the input ramp function used to drive the model. As the series stiffness increases ($k_{se} \approx 100$), the "tendon" is sufficiently stiff so that the parallel viscous element's damping becomes evident - leading to a first-order rate of decrease from the peak stretch-resultant force. For increasing k_{se} , the damping's effect becomes more pronounced and the peak force increases. As the series elastic elements stiffness approaches the maximum value 1125 N, a 4 mm, 100 mm/s ramp function elicited a peak and steady-state tension of 1.87 N and 1.5 N, respectively. In general the rate at which the muscle's force is produced is proportional to the ramp function's rate/gradient. Increasing the series stiffness of the muscle further doesn't change the qualitative properties of the behaviour.
- **Parallel stiffness k_{se} variation.** As before, in determining k_{pe} 's effects of the muscle model, k_{se} and b were held constant. In general, the parallel element's stiffness affects the steady state force generated in the model: too low a value and the steady-state tends towards to zero, too high and the steady state value is numerically equal to k_{se} (see figure 3-3(b)). For $k_{se} \rightarrow 0$, the muscles tension's transient response looks akin to an impulse, spiking to a peak value 0.83 N, before decaying to zero. As the parallel stiffness increases, e.g. $k_{se} = 100$, the peak increases to 1.069 N and a non-value steady-state value 0.3673 N is generated. Further increase the parallel stiffness increases the peak tension output and reduces the peak-stead-state difference. In general, the parallel stiffness helps determine the magnitude of the steady-state value.

- **Parallel viscosity b variation.** In order to determine b 's effects on the muscle model's output, we isolated k_{se} and k_{pe} ; holding the stiffnesses constant. Generally speaking, eliminating damping in the muscle causes the output of the muscle traces the input; amplified proportional to k_{se} and k_{pe} (see figure 3-3(c)). Increasing b from near-zero values cause the characteristic spike in muscle tension to occur. In addition, increasing damping from zero introduces the aforementioned steady-state-peak difference. As b is increased further, the transient response approaches that shown in 3-2(a). From simulation, b has little effect on the tension's output gradient.

Having determined the series and parallel elastic and viscous parameters' effects on the Hill model's passive properties, the following considers the case of active isotonic contraction; where, the muscle's active force was 10 N. As before, for a 4.00 mm ramp stretch applied at 100 mm/sec, the parameters' effects are summarised below:

- **Active force component magnitude.** In order to determine the active force component's effects on the muscle's tension output, the passive elastic and viscous elements were left at their default values. Here, step changes in the muscle's active force were applied. For $A = 0$ no tension is generated by the Hill type model under isometric conditions. As A is increased, step inputs evoke characteristic transient responses (see figure 3-4(a)). For the muscle's default parameters, steady-state tension T_{ss} was equivalent to $0.667A$, which for either a step or ramp input of magnitude $A = 10$ resulted in $T_{ss} = 6.667$ N. Increasing A further does not qualitatively change this observation.
- **Series stiffness k_{se} variation** In order to determine the series elastic element's effect of the active generation of muscle force, A was set to 10 N, and k_{pe} and b left at the default values. Increasing the series elastic element's stiffness results in a proportional increase in generated muscle tension (see figure 3-4(b)) as a function of A , which can be reasoned for by noting that k_{se} of equation (3.9) multiplies the body of the equation.
- **Parallel stiffness k_{pe} variation.** In order to determine parallel elastic ele-

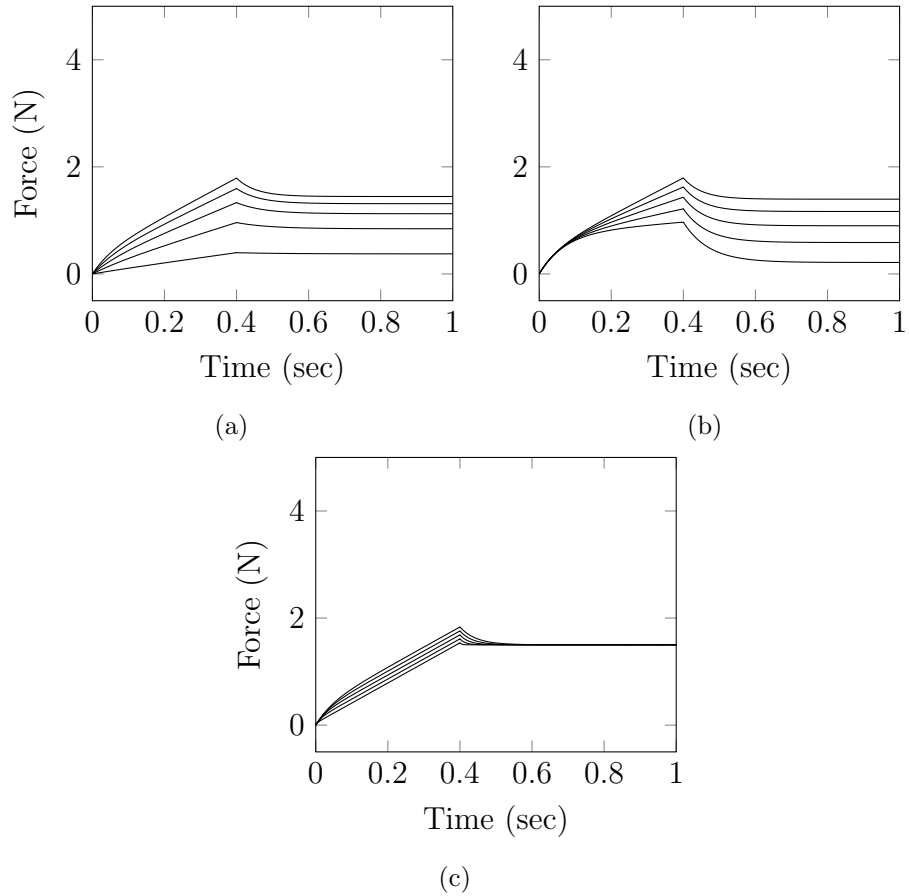


Figure 3-3: SIM Response of the modelled Hill muscle's active tension to (a) changes in the series stiffness k_{se} , (b) parallel stiffness k_{pe} , and (c) parallel viscosity b . In this example $k_{se} = \{112.50, 337.50, 562.50, 787.50, 1125.00\}$ N/m, $k_{pe} = \{56.25, 168.75, 281.25, 393.75, 562.50\}$ N/m, and $b = \{8.34, 25.01, 41.69, 58.37, 83.38\}$ N/m/s.

ment's effect on active force production, the active force A was set to 10 N and k_{se} and b held at default values. In general, decreasing parallel stiffness has the effect of increasing the produced tension (see figure 3-3(b)); where, increasing parallel stiffness results in the steady-state tension T_{ss} reducing from 9.524 N at $k_{pe} = 56.25$ to 6.67 N at $k_{pe} = 56.25$ N. Varying k_{pe} also has the effect of changing the tension's transient response rise time t_r (measured between 10% and 90% T_{ss}) from 109.00 ms to 157.60 ms: a 44.59% increase. Increasing k_{pe} does not change the qualitative nature of the output, which remains characteristic of a first order response.

- **Parallel viscosity b variation.** As before, to determine the parallel viscous element's effect on muscle tension, the active force component was set at 10 N, while k_{se} and k_{pe} were held at default values. Generally speaking, the effect of parallel viscosity is to slow down the muscle's rate of tension production. For b increasing from 8.34 N/m/s to 83.38 N/m/s, the rise time of the transient response t_r (measured between 10% and 90% T_{ss}) increases from, approximately, 11.50 ms to 109.00 ms: an 847.83 % increase. In addition, oscillation in muscle tension output is eliminated as the $b \rightarrow 83.38$ N/m/s. Varying b has no significant effect on the steady-state T_{ss} , which remains equal across the viscosity parameter set.

3.7 Antagonistic Actuation

A key reason to investigate antagonism is to see what effects differential and coactivation of antagonistic muscles have on joint dynamics; moreover, whether these contributions could be applied to control of a wearable assistive device. In this section, the results of simulating an antagonistically coupled pair of the implemented soleus muscles are presented. As before, simulations were carried out in MathWorks' Simulink environment. The active force component has been limited to a positive only force and all other modelling constraints maintained. The results of differential and coactivation of the antagonistic muscles is summarised below:

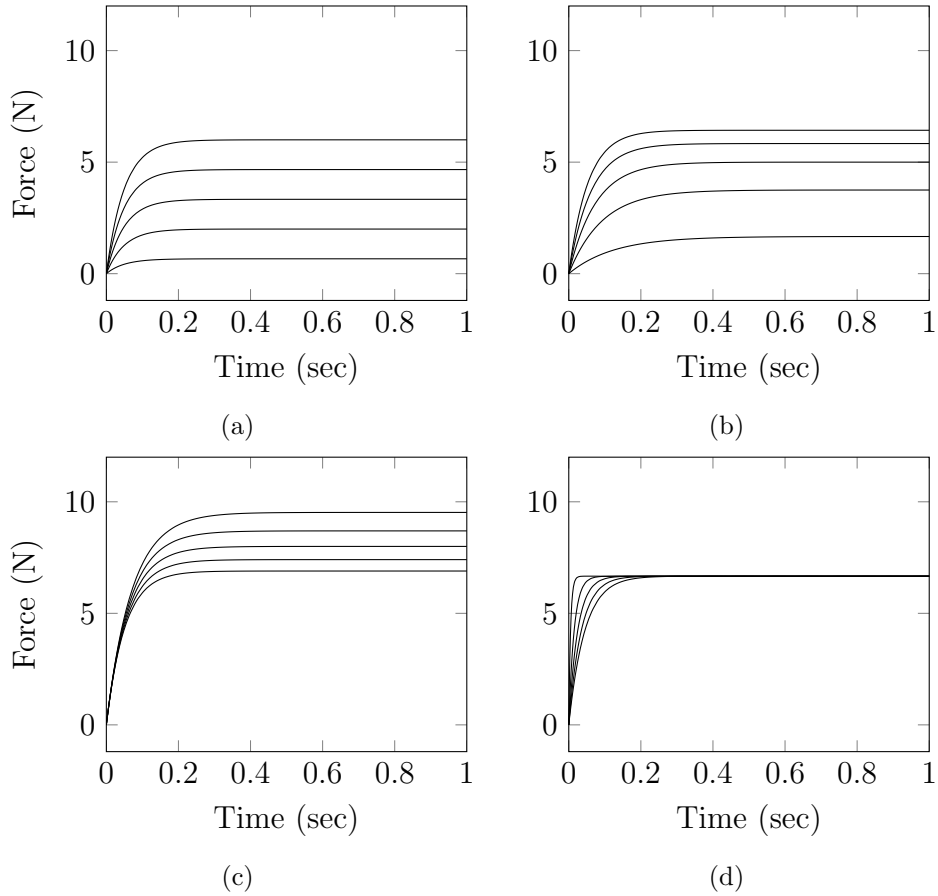


Figure 3-4: SIM Response of the modelled Hill muscle's active tension to (a) changes in the active force component A , (b) series stiffness k_{se} , (c) parallel stiffness k_{pe} , and (d) parallel viscosity b . In this example, $A = \{1, 3, 5, 7, 10\}$ N, $k_{se} = \{112.50, 337.50, 562.50, 787.50, 1125.00\}$ N/m, $k_{pe} = \{56.25, 168.75, 281.25, 393.75, 562.50\}$ N/m, and $b = \{8.34, 25.01, 41.69, 58.37, 83.38\}$ N/m/s.

- **Differential Activation.** As discussed, two soleus muscles have been coupled in antagonism; where, the extensor's active force has been increased from 0 N to 50 N in 10 N increments. Two simulations have been performed: first, a constant extensor force was applied; second, a sinusoid of equal magnitude and frequency of 1 rad/sec was applied. In either case, the flexor's nominal active force was set to 10 N. Figure 3-5(a) shows the modelled limb's transient response as a function of constant extensor tensor. It can be seen that the joint angle varies from 0 rad to 0.459 rad, which corresponds to an angular displacement ranging from 0deg to 26.30deg; a 0.5260deg/N change. Figure 3-5(b) depicts the modelled limb's transient response to a sinusoidal extensor active force. As before, the maximum angular displacement was 0.459 rad, or 2deg; however, the joint angle is not constant, rather it traces a sinusoidal path proportional to the input sine function. Note that there are quiescent periods where the joint does not move - this is due to the extensor muscle being unable to push, i.e. generate a force in response to a negative active force.
- **Coactivation.** Given the same antagonistic pairing of implemented soleus muscles, as before. Both the Extensors and flexor's active forces were increased from 0 N to 2.0 N in 0.5 N increments. Two simulations have been performed: first, equal extensor and flexor active forces were applied, followed by a 10 N load applied distally at 0.35 m, equivalent to a 3.5 Nm torque load, at time $t = 2.0$ sec; second, the same perturbation was applied as a pulse of 100 ms duration. Figure 3-6(a) shows the antagonistic system's response to the step perturbation; reducing the resulting angular displacement from 0.09 rad to 0.06 rad, a 5.16 deg to 3.44 deg change, for an increasing level of coactivation. It should be noted, that, for an active force equal to, or greater, than 2.5 N, the joint becomes maximally stiff: resulting in a maximum displacement of 0.06 rad irrespective of increasing active force. Figure 3-6(b) depicts the antagonistic extensors and flexor's response to a 3.5 Nm, 100 ms pulse. It can be seen that for equal coactivation, a displacement decreasing from 0.026 rad to 0.022 rad can be achieved. Again, as the muscle's active force increases, the maximum

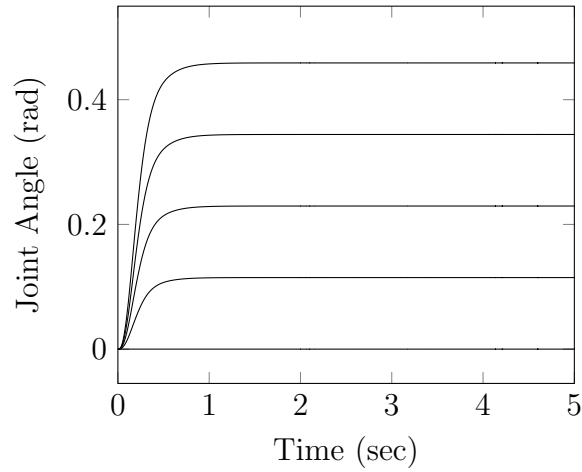
displacement tends towards a boundary point: 0.022 rad.

3.8 Summary

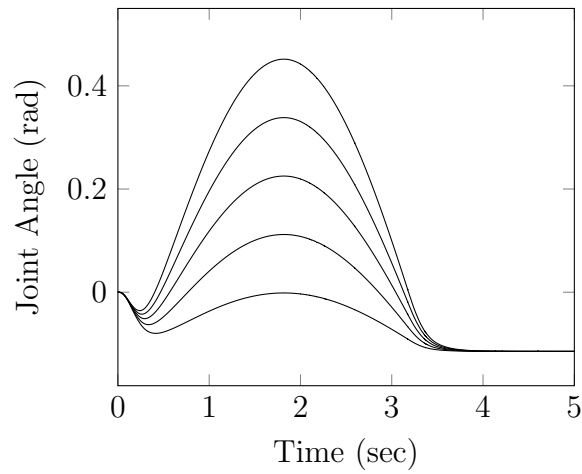
In this chapter, this thesis has discussed the implementation of a feline's soleus Hill-type muscle, presenting a parametric analysis of the model. Following the analysis, an antagonistically coupled pair of the soleus muscles were presented; where, active contractile forces contribution to the movement and compliance was identified. While the Hill type muscle model is well established, reviewing literature, we did not see a parametric analysis identifying the impacts of changing variables on overall model dynamics; as such, this thesis makes it clear what happens in response to parametric change.

With respect to Hill's three element muscle model, it is phenomenological; describing the generation of force in terms of series and parallel stiffness and damping elements. With respect to variation of the muscle's passive properties, this thesis has found the following: muscle tension T 's magnitude is tightly coupled to the series stiffness k_{se} , as stiffness increases so too does tension's magnitude; increasing parallel stiffness k_{pe} determines the steady-state value of the muscle when exposed to a ramp stretching function, increasing T_{ss} as k_{pe} increases; and parallel viscosity b affects the production of the spiking-peak behaviour of the passive output, although, it doesn't appear to significantly affect the qualitative behaviour of the muscle. With respect to variation of the muscle's properties under active conditions, we have made the following observations: when increasing the muscle's active force component, the generated tension's transient response is akin to that of a first order system's; for increasing series stiffness k_{se} , the produced tension increases proportional to the increase in stiffness; for increasing parallel stiffness k_{pe} , the steady-state's magnitude decreases; and increasing parallel viscosity b has the effect of slowing down the muscles transient response: increasing the generated tension's rise time.

In terms of antagonistic coupling of the soleus muscle, simulation of an increasing agonist contractile force resulted in a joint's limb rotating up to 0.459 rad, settling to

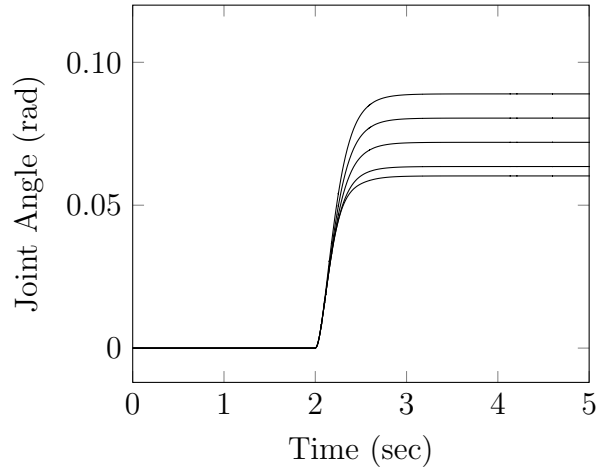


(a)

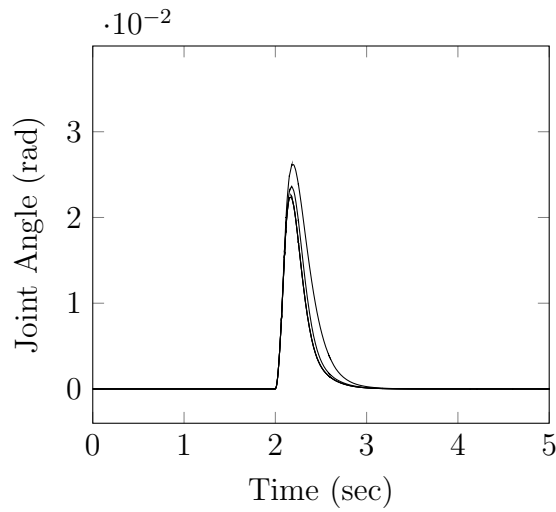


(b)

Figure 3-5: SIM Response to (a) constant and (b) sinusoidal differential activation of an antagonistically actuated limb joint. Given an extensor's active force of $A_E = [10,20,30,40,50]$ N, the top plot shows the corresponding response; increasing from 0 rad to a maximum 0.459 rad. For a sinusoidal extensor force of the same amplitude and frequency of 1 rad/sec, the bottom plot shows the limb joint's transient response. As before, the maximum angular displacement is 0.459 rad; however, it is not constant, rather, it follows the input sine function.



(a)



(b)

Figure 3-6: SIM Response of a coactivation limb's joint angle to (a) constant, distally applied, perturbation and (b) a 100 ms, 3.5 Nm disturbance. Given the system's extensors and flexor's active force of $A_{E,F} = \{0,0.5,1.0,1.5,2.0\}$ N, the top plot shows the response to a fixed load applied at time $t = 2$ sec; decreasing from a maximum 0.09 rad to 0.06 rad. The bottom plot shows the equally activated muscles' response to the pulsed load; decreasing from a maximum of 0.026 rad to 0.022 rad.

a new equilibrium point under a constant active force of 50 N. Sinusoidal variation of the extensor's active force resulted in the limb's joint tracing a path proportional to the input sine function. In addition, equal activation of the agonist and antagonist muscles produced no net torque; rather, it resulted in increased stiffness. Given a step of 10 N applied distally, the 3.5 Nm perturbation elicited a maximum displacement of 0.09 rad, which reduced to 0.06 rad as coactivation resulted in increasing the joint's maximum stiffness, a 33.33 % decrease, as extensor and flexor active force $A_{E,F}$ increased from 0 N to 2 N.

With respect to wearable assistive devices, this chapter's observations are of particular use; namely, those drawn from simulation of differential and coactivation of antagonistic muscles. In being able to vary a joint's stiffness, and therefore its compliance, we have identified a mechanism for ensuring an assistive device is safe to use, i.e. compliant, while also being able to be control a joint's angle via varying the paired muscle's equilibrium point.

Chapter 4

Novel Central Pattern Generator and Analysis

This chapter introduces the methodology used to analyse the central pattern generators (CPGs), which are used throughout this thesis. It introduces the concepts of quasi-linearisation and describing function analysis, discussing their application to non-linear systems. Following that, the chapter presents the pattern generator's governing equations and describes how they are coupled to a wearable assistive device's (WAD) joint. The chapter then introduces the non-linear system analysis methodology, which is applied to the pattern generators. The describing function analysis is accurate, and can be applied in a number of ways. It shows the effects of parameters on the overall systems gain and phase, which enables the tuning of parameters. It also shows the inherent robustness of the pattern generator's properties to parameter and system changes; in other words, the controller's ability to remain stable in response to a wide range of stimulus or stimuli. The chapter concludes by demonstrating the coordination between the pattern generator's dynamics and a number of single degree-of-freedom mechanical systems.

4.1 Introduction

A system that obeys the superposition principle is said to be *linear*. The principle states that if the input $x_1(t)$ elicits the response $y_1(t)$, and $x_2(t)$ elicits the response $y_2(t)$, then for any value of a and b , the response to $ax_1(t) + bx_2(t)$ will be $ay_1(t) + by_2(t)$, which must be true for all inputs. Any system for which the superposition principle doesn't hold is defined as *non-linear*. In this case, it is not possible to generalise from the responses of any class of inputs to the response of any other input [56][18].

The response of a linear time-invariant system to any input, can be expressed as the convolution of that input with the system's transfer function. The response for any initial conditions, of whatever magnitude, can always be decomposed into complex exponential functions of time, or as real exponentials and exponentially increasing or decreasing sinusoids. Non-linear systems, in contrast, cannot be characterised in this way; a key difference is non-linear system's reliance of the response on the amplitude of the input - either the forcing input or initial conditions

The issue of studying the nonlinear pattern generator can be avoided altogether by replacing the non-linear element with a linear operation; however, this is dependent on the validity of the linearising approximation, which generally is only justified around a small deviation about a critical point (i.e, the nominal linearisation point). Any response that carries variables through a range which exceeds the limits of reasonable approximation cannot be described in this way.

If the small-signal constraint of true linearisation is relieved, but linearisation's advantages maintained, it is necessary to determine the operation performed by the non-linear element on a finite signal, approximating it with a linear operation. This results in different approximations for the same non-linearity when driven by an input of varying magnitude. The approximation of a non-linear operation by a linear one that depends on some properties on the input's characteristics (e.g., magnitude and frequency) is termed *quasi-linearisation*. By definition, a transfer function of a true linear, time-invariant system cannot depend on the amplitude of the input function because an LTI system is linear. Thus, this dependence on amplitude generates a

family of linear systems that are combined in an attempt to capture salient features of the non-linear system behaviour. The advantage of quasi-linearisation is that there is no limit to the range of signal magnitudes which can be linearised.

With respect to feedback systems, the signal at the input to the non-linearity depends on both the reference input and the feedback (i.e., the error signal), which complicates the determination of the form of the signal which appears at the non-linearity's input. For quasi-linearisation, input signal form, typically: bias, sinusoid, or a Gaussian process, can be specified; simplifying the problem. These approximating functions, which describe the non-linearity's transfer function, are termed *describing functions*.

Of the various describing functions, the *sinusoidal-input describing function*, Equation (4.1), is by far the most widely used

$$l(t) = A \sin(\omega t + \theta), \quad (4.1)$$

where A and ω are the amplitude and frequency, respectively, and θ is describing function's phase, which we set to 0 here.

The advantage of sinusoidal describing function linearisation is that it allows a wide range of totally unrelated modes of behaviour to be studied. In the following sections, we present our central pattern generator models, subsequently discussing our method of analysis in following sections.

4.2 The Central Pattern Generator

The central pattern generator (CPG) used throughout this thesis utilises Graham Brown's half-centre concept; where, the pattern generator consists of two reciprocally coupled, and mutually inhibited simulated spiking neurons. Figure 4-1 shows the overall organisation. The pattern generation model approximates the firing rate envelope of a real biological neuron with firing-rate adaptation

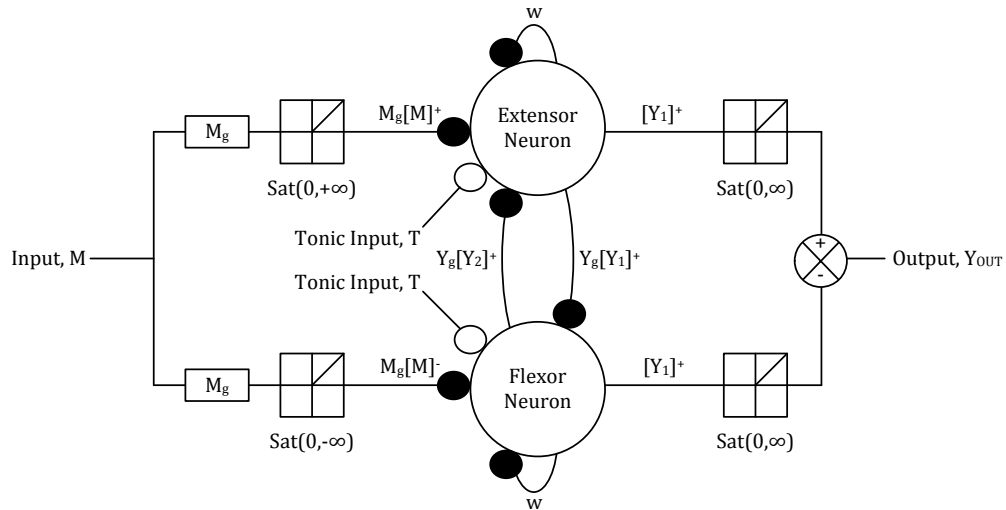


Figure 4-1: Schematic of the pattern generator. Black circles denote inhibitory inputs; open circles to excitatory inputs. The mutual inhibition is through $Y_g[Y_n]^+$ connections, and w is the corresponding neuron's firing-rate adaptation. The input M is weighted by input gain M_g , then split into positive and negative signal portions. The positive part $M_g[M]^+$ inhibits the extensor neuron; whereas the negative component $M_g[M]^-$ inhibits the flexor neuron. The positive output of each neuron is weighted by gain Y_g and used to inhibit the reciprocal neuron. The output of the pattern generator Y_{Out} is the difference of the neuron's firing rates.

The model is governed by the following equations:

$$C \frac{dV_1}{dt} = T - w - g_L (V_1 - E_L) + g_L \Delta_T \exp\left(\frac{V_1 - V_T}{\Delta_T}\right) - V_1 - Y_g[Y_2]^+ - \Sigma M g [M_n]^+ \quad (4.2)$$

$$\tau_w \frac{dw}{dt} = a (V - E_L) - w \quad (4.3)$$

$$Y_1 = \frac{t}{e} \exp\left(\frac{-t}{e}\right) * \delta(t - t_1) \quad (4.4)$$

$$C \frac{dV_2}{dt} = T - w - g_L (V_2 - E_L) + g_L \Delta_T \exp\left(\frac{V_2 - V_T}{\Delta_T}\right) - V_2 - Y_g[Y_1]^+ - \Sigma M g [M_n]^- \quad (4.5)$$

$$\tau_w \frac{dw}{dt} = a (V - E_L) - w \quad (4.6)$$

$$Y_2 = \frac{t}{e} \exp\left(\frac{-t}{e}\right) * \delta(t - t_2) \quad (4.7)$$

$$Y_{Out} = [Y_1]^+ - [Y_2]^+ \quad (4.8)$$

At spike time t_n ($V > -20mV$) : $V \rightarrow E_L$, and $w \rightarrow w + b$

Function $\delta(t, t_n)$ of Equations (4.4) and (4.7) is the time shifted Dirac delta function $\delta(t)$. Mathematically, the Dirac delta function is defined by:

$$\int_{t_1}^{t_2} x(t) \delta(t) dt = x(0), \quad t_1 < t < t_2 \quad (4.9)$$

provided $x(t)$ is continuous at $t = 0$.

The function $\delta(t)$ is depicted graphically by a spike at the origin and possesses the following properties:

1. $\delta(0) \rightarrow \infty$
2. $\delta(t) = 0, t \neq 0$
3. $\int_{-\infty}^{\infty} \delta(t) = 1$
4. $\delta(t)$ is an even function; i.e., $\delta(t) = \delta(-t)$

Due to the discontinuous nature of $\delta(t, t_n)$, we have used the following continuous

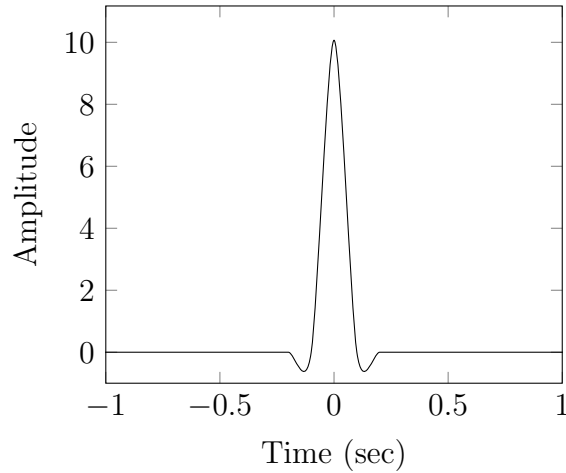


Figure 4-2: SIM Dirac delta plot used to describe the "impulse" behaviour of a neuron's action potential. In this example $d = 0.01$.

function in lieu of Equation (4.9):

$$\delta(t, t_n) = \frac{1}{\pi\sqrt{d}} \exp\left(-\frac{(t - t_{n1})^2}{d^2}\right), \quad (4.10)$$

where parameter d determine the function's height, width, and rate of change; and t and t_n are time and neuron spike time, respectively. Via substitution, it can be seen that for a "small" d , Equation (4.10) has the following properties:

1. The value at $t = 0$ is very large (i.e., $\delta(t, t_n) \rightarrow \infty$).
2. The duration of is relatively short (i.e., tends towards zero as $d \rightarrow 0$).
3. The total area under the function is constant and equal to one.
4. The function is equal.

We reason, that, since (4.10)'s properties are akin to those of (4.9), Equation (4.10) is an appropriate approximation of Equation (4.9).

The function,

$$k(t) = \frac{t}{e} \exp\left(\frac{-t}{e}\right),$$

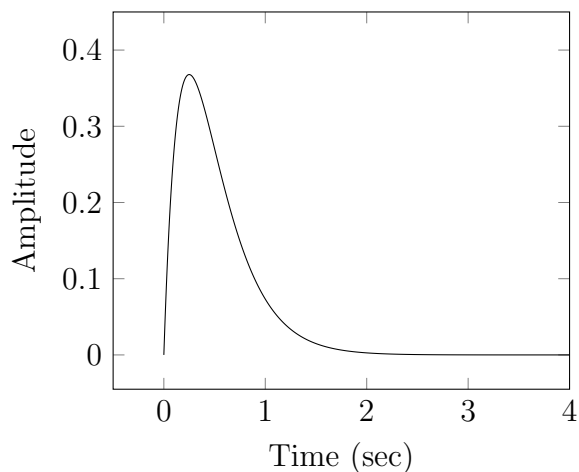


Figure 4-3: SIM Linear kernel plot. The linear kernel is convolved with the Dirac delta function in order to generate a continuous neuron output rather than a discrete impulse. In this example $e = 0.25$.

of Equations (6.3), (4.7) is the linear kernel (figure 4-3) which is convolved with the Dirac delta function (figure 4-2 generated at spike time t_n). In this thesis we have used $e = 0.25$, which we have empirically determined to ensure limit cycle rhythmogenesis in the pattern generator.

Each modelled neuron's spiking behaviour is governed by two equations; neuron 1 by (4.2) and (4.3), and neuron 2 by (4.5) and (4.6). The variables V_1 and V_2 represent the neurons' membrane voltage, and the w_1 and w_2 variables represent the neurons' internal adaptation to their respective firing rates. The variables Y_1 and Y_2 represent the firing rate of the neurons, and are taken to be result of convolving a Dirac delta function at the neurons' spiking time, t_1 and t_2 , with the linear kernel $k(t)$. The output of the pattern generator is taken to be the difference of Y_1 and Y_2 : Equation (4.8). Like the Graham Brown's half-centre oscillator, the neurons are reciprocally organised, mutually inhibiting each other via (4.2) and (4.5)'s Y_1 and Y_2 terms.

The pattern generator can be characterised by the following parameters: e , which determines the linear kernel $k(t)$'s height, gradient, and width; d , which determines the "sharpness" of Equation (4.10)'s impulse; E_L , which sets the neurons' resting

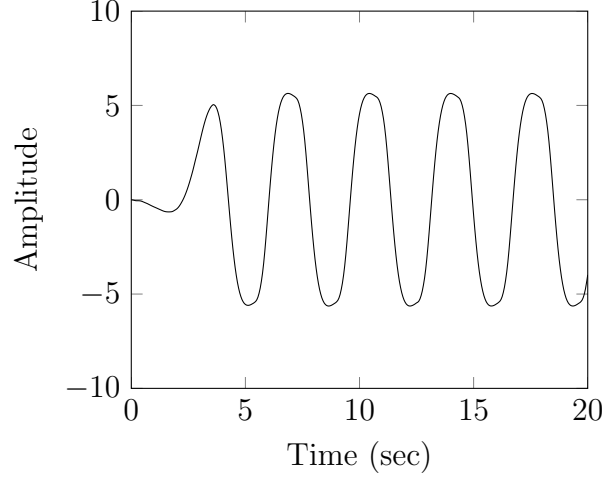


Figure 4-4: SIM Natural central pattern generator output. In the absence of input, the pattern generator oscillates at its natural frequency $\omega_n = 1.7257$ rad/sec with a maximum amplitude $A = 5.6376$. In this example, $T = 5e^{-9}$, $C = 281e^{-12}$, and $\tau_w = 1$.

potential; V_T , which sets the neurons' threshold potential; Δ_T , is the slope factor; gL , which sets the neurons' leak conductance (i.e., the inverse of resistance); T , the tonic/constant parameter, which enables rhythmogenesis and determines the CPGs output's amplitude A ; C , the neurons' capacitance, which determines each neuron's firing rate; and τ_w and b , which determine the rate of adaptation dw/dt .

Inputs are applied to the pattern generator through the variable M_n , which is weighted by Mg . The inputs are arranged to always inhibit the neuron, applying the positive part $[M_n]^+$ to one neuron, and the negative part $[M_n]^-$ to the other.

When no input is applied to the pattern generator, the CPG oscillates at its natural frequency ω_n , which determined by the neurons' capacitance C and adaptation constants, τ_w and b , with a fixed amplitude defined by the tonic input T , as shown in 4-5. If an oscillatory input is applied to the CPG, the pattern generator entrains to the input, producing an output at the same frequency of the input. This entrainment behaviour is illustrated in figure 4-6. The CPG tends to entrain very quickly, generally within one cycle of the pattern generator's input signal's frequency.

As discussed, the central pattern generator's application is control of an antago-

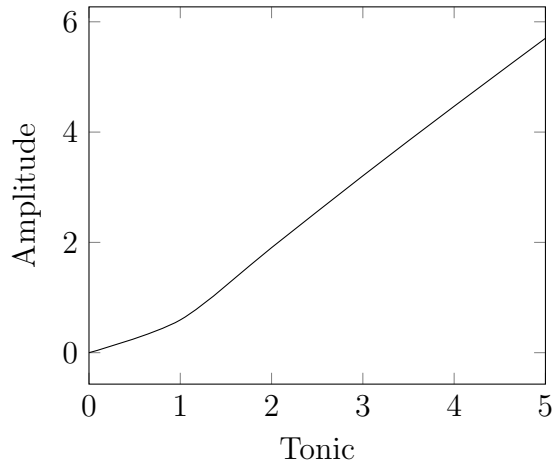


Figure 4-5: SIM Pattern generator behaviour under changing tonic T . The graph shows the amplitude of the CPG plotted against normalised tonic excitation (i.e., $T/1e^{-9}$). For this example $C = 281e^{-12}$ and $\tau_w = 1$.

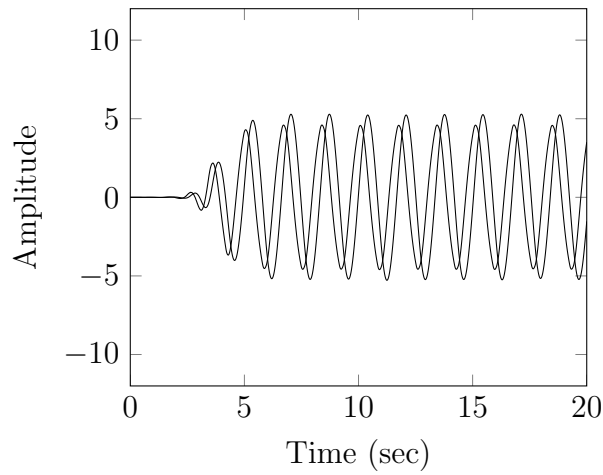


Figure 4-6: SIM Plot of the pattern generator and coupled systems' outputs Y_{out} and L as functions of time. In this example, $m = 1$ kg, $b = 2$ Ns/m, and $k = 10$ N/m.

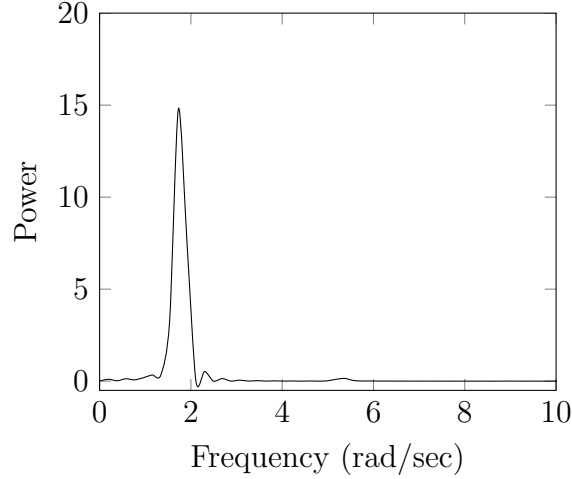


Figure 4-7: SIM Power density spectrum of the pattern generator. The plot shows power plotted as a function of frequency, where the peak frequency ω_n occurs at $\omega = 1.7257$ rad/sec, and a much smaller one at $\omega = 5.2$ rad/sec or $\omega = 3\omega_n$. The sinusoidal nature of the pattern generator agrees with the describing function's approximation.

nistically actuated wearable assistive device's joints. To control the WAD's angular position, a proportional-derivative (PD) control law is used, making the commanded torque at the i th joint

$$u = k_c(h_0\theta_{in} - \theta) - k_d\dot{\theta} \quad (4.11)$$

where k_c is the proportional constant, equivalent to joint stiffness; k_d is the derivative constant, equivalent to joint viscosity; h_0 is the input gain, θ_{in} is the desired joint angle, and θ and $\dot{\theta}$ are the joint's current angle and angular velocity, respectively. The pattern generator is designed to be connected to an assistive device using the pattern generator's output to control the set-point for the joint and connecting either the joint angle or the joint torque u to the input l of the pattern generator.

4.3 Analysis Methodology

The pattern generator is a non-linear system, whose output depends on the amplitude and frequency of its input, as well as, the dynamics of the coupled linear system. As

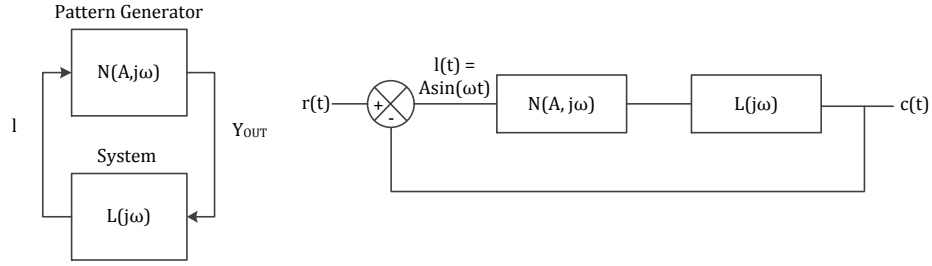


Figure 4-8: Coupled pattern generator and system schematic. (Left) The figure shows the pattern generator tightly coupled with the linear system. The pattern generator's out Y_{out} drives the linear system, whose output l is the CPG's input. At frequency ω and amplitude A , the linearised frequency responses of the CPG and system are $N(A, j\omega)$ and $L(j\omega)$, respectively. (Right) Closed-loop system with a nonlinear element. Here $N(A, j\omega)$ characterises the pattern generator's non-linearity and $L(j\omega)$ represents the frequency transform of the coupled linear system. Stable limit cycle oscillations will only occur when $N(A, j\omega)L(j\omega) = -1$.

such, it is necessary for a non-linear analysis methodology to be applied in order to elucidate the CPGs and coupled pattern generator and system's behaviour. Briefly, the approach taken is to express the pattern generator and coupled system as frequency responses, subsequently treating $N(A, j\omega)$ and $L(j\omega)$ as linear gains. In this section we present our application of the describing function analysis methodology.

The coupled CPG and system is shown in figure 4-8, where the non-linear element $N(A, j\omega)$'s output Y_{out} is passed to the linear system $L(A, j\omega)$'s input, whose output l is fed back to the non-linear element's input port.

One of the key assumptions made in order to carry out describing function analysis is that the non-linear system $N(A, j\omega)$ does not contain higher order dynamics, and that the coupled linear system's gain be much lower at these harmonics (i.e., $L(j\omega)$ acts as a low-pass filter). The Fourier transform of the pattern generator's output is shown in 4-7. The power density spectrum of the output shows a clear fundamental peak at $\omega = 1.7257$ rad/sec, the CPG's natural frequency ω_n .

Given that $N(A, j\omega)$ characterises the pattern generator's nonlinearity, the describing function can be used to describe the pattern generator's effects on the closed-

loop system of figure 4-8.

If the input of the closed loop in figure 4-8 $r(t)$ is taken to be zero, the pattern generator's input is:

$$X(j\omega) = -L(j\omega)Y(j\omega) \quad (4.12)$$

If the pattern generator's describing function is taken to be a linear gain; the CPG's output can be expressed as:

$$Y(j\omega) = N(A, j\omega)X(j\omega) \quad (4.13)$$

Substituting equation (4.13) into (4.12), the characteristic equation is therefore

$$1 + N(A, j\omega)L(j\omega) = 0 \quad (4.14)$$

Solutions of this equation yield the amplitudes and frequency of the loop limit cycles. Figure 4-9 depicts one such limit cycle.

The closed-loop characteristic equation for linear systems with gain K can be expressed as

$$KL(j\omega) = -1 \quad (4.15)$$

where the fixed point (-1,0) is the stability boundary point. Equation (4.15) can be written alternatively, as

$$L(j\omega) = -\frac{1}{K} \quad (4.16)$$

in which case the stability point(-1/K,0), a variable quantity depending on the gain K . Similarly, the characteristic equation (4.14) can be expressed as

$$L(j\omega) = -\frac{1}{N(A, j\omega)} \quad (4.17)$$

Satisfaction of equation (4.17) indicates a limit cycle. Plotting $L(j\omega)$ and $1/N(A, j\omega)$ loci on the same set of coordinates, possible limit cycles are made to occur at the intersection of the two plots.

In order for the previous analysis to be congruent with the presented pattern

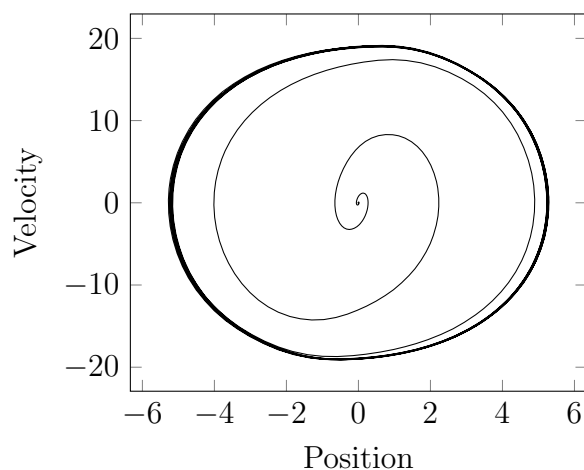


Figure 4-9: SIM Phase plot of the coupled pattern generator and system $L(j\omega)$. The plot shows velocity as a function of position for a coupled CPG and linear system. The plot converges to a limit cycle, irrespective of the initial conditions.

generator, it is important to note that the CPG's extensor and flexor neurons are inhibited by input l when $l > 0$ and $l < 0$, respectively; in essence constituting a negative feedback system. Therefore, given a negative feedback topology the net effect will be equivalent to that of a positive feedback system's. This can be easily accounted for by ensuring the condition for limit cycle oscillation, rather than (4.17), is

$$L(j\omega) = \frac{1}{N(A, j\omega)} \quad (4.18)$$

4.4 Pattern Generator Describing Function

The pattern generator's describing function $N(A, j\omega)$ expresses the gain and phase difference between input and output as a function of amplitude and frequency. This can be calculated by applying a sinusoidal input to the non-linear element's input, e.g. $l(t) = A\sin(\omega t)$, and measuring the output Y_{Out} . If the amplitude and frequency of Y_{Out} and l are the same; the pattern generator is said to be *entrained*, and the Fourier transform can be used to determine A and ω . The describing function of the

coupled pattern generator and linear system is shown in figure 4-11. In this example the amplitude and frequency lies between 5 and 10, and 2.5119 rad/sec and 3.9811 rad/sec, respectively.

Figure 4-10 shows the Bode plot of the describing function $N(A, j\omega)$. From the magnitude plot, it can be seen that for an increasing amplitude, the gain decreases slightly (i.e., $N(A, j\omega)$ is inversely proportional to input amplitude). As frequency increases from 1.2589 rad/sec to 3.1623 rad/sec, the magnitude's response increases monotonically from -3 dB to 1.34 dB; however, as frequency increases past $\omega = 3.1623$ rad/sec, the magnitude decreases at a rate of, approximately, -50 dB per decade. From the phase angle plot, it can be seen that the phase is bounded between the asymptotes 180^{deg} and -90^{deg} for ω approaching 0 rad/sec and 10 rad/sec.

With respect to wearable assistive devices, the WAD's limb is modelled as a mass m actuated by a linkage of stiffness k via a joint of viscosity b . Ignoring the dynamics of the actuator, the dynamics of the link are given by the following:

$$m \frac{d^2\theta}{dt^2} + b \frac{d\theta}{dt} + k\theta = k\theta_i n \quad (4.19)$$

where θ and $\theta +_i n$ are the assistive devices joint's angle and desired angle, respectively. The transfer function for the linear system is given by

$$L(s) = \frac{k}{ms^2 + bs + k} \quad (4.20)$$

Substituting $s = j\omega$, the transfer function is given by

$$L(j\omega) = \frac{k}{k - m\omega^2 + j\omega b} \quad (4.21)$$

The condition for limit cycle oscillation (equation 4.18) can now be solved graphically by plotting $L(j\omega)$ and $N(A, j\omega)$ on the complex plane and finding points of intersection for equal frequency. Figure 4-11 shows the combined plots. There exists a number of intersection points; however, there is only one where the frequency is common. The intersection point determines both the frequency and amplitude of

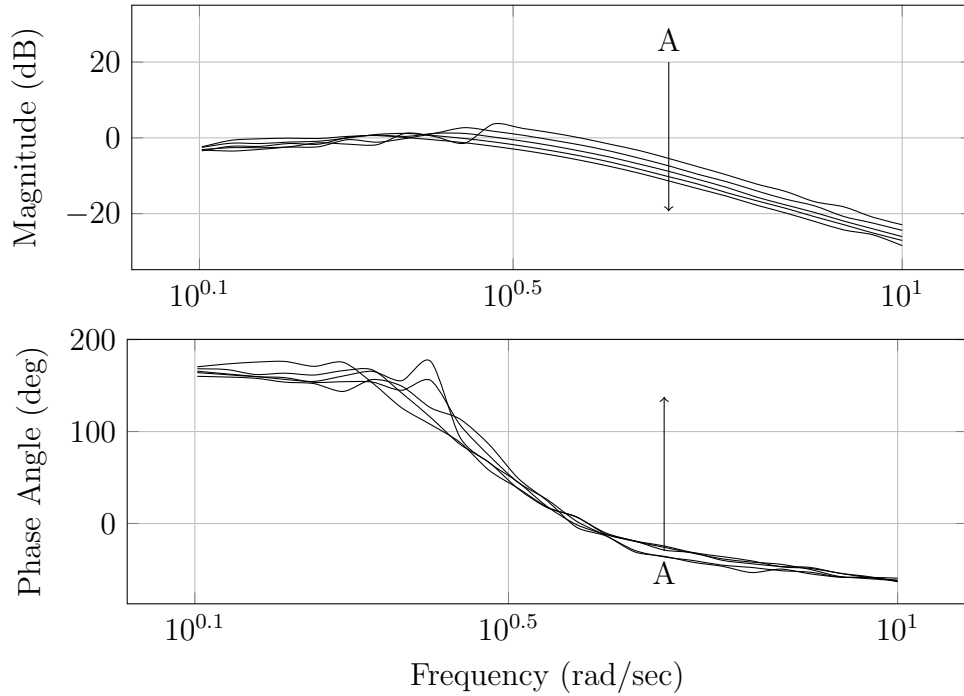


Figure 4-10: SIM Coupled pattern generator and system Bode plot. The top graph shows the coupled system's gain $|N(A, j\omega)|$ plotted as a function of frequency. The multiple lines on the magnitude plot correspond to the amplitudes A applied, equal to 5 through 10. Gains increase monotonically, from -3 dB to 1.34 dB, for frequencies between 1.2589 rad/sec and 2.51 rad/sec; after which, the gain decreases by - dB per decade. The bottom plot corresponds to the coupled systems phase angle. As ω tends towards zero, phase angle θ approaches the 180deg upper bound; whereas, ω tend towards infinity, the phase angle approaches the -90deg lower bound.

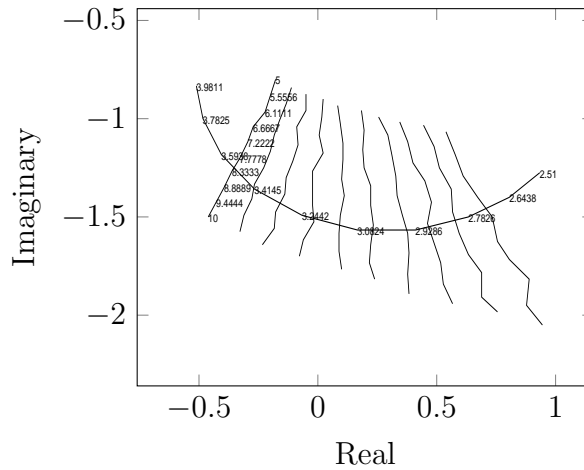


Figure 4-11: SIM Complex plane plots of coupled system's $N(A, j\omega)$ and $L(j\omega)$ as functions of A and ω . The plot $1/N(A, j\omega)$ corresponds to the linearised pattern generator; where, (i.e., the vertically aligned plots), correspond to constant frequency, with amplitude A increasing along each line. A limit-cycle solution at the point where the two plots intersect; here, $\omega_f = 3.163$ and $A_f = 8.8889$. In this example $m = 1$ kg, $b = 2$ Ns/m and $k = 100$ N/m, corresponding to a natural frequency ω_n of 3.1623 rad/sec.

the limit cycle solution. In this case $\omega_f = 3.1623$ rad/sec and $A_f = 8.8889$.

4.5 Limit Cycle Stability

With respect to stability, if the limit cycle (see figure 4-9) is perturbed and returns to the original state it will be stable; whereas, if the either its amplitude or frequency tends towards another equilibrium state, it will be unstable. In terms of small perturbations, the limit cycle stability becomes a problem of transient oscillation; however, if terms involving rate change of frequency and damping are ignored, it is possible to account for limit stability via the graphical approach. If the limit cycle perturbation is positive, a stable system, in which energy is dissipated, is required; whereas, if the perturbation is negative, an unstable system, in which energy is absorbed, is required. This behaviour ensures a locally stable limit cycle.

4.6 Parameter Evaluation

In this section we evaluate the coupled pattern generator and linear system's parameter's effects on output. To do so we apply describing function analysis, which grants insight into the output's frequency and amplitude as function of static inputs, gains, and time coefficients. In general, analysis reveals the pattern generator to be robust and capable of adapting to a wide range of frequencies and system parameters; encouraging results when considering the application at hand.

Gains and tonic inputs. The tonic parameter T affects the output amplitude of the pattern generator and is effectively decoupled from all other parameters. The effect of the tonic parameter is monotonic, as was shown in figure 4-5, and can be understood by looking at equation (4.2). Disregarding all other inputs, other than the tonic input T , equation (4.2) can be expressed as $CdY/dt = T - Y$. The solution is $Y = T - T \exp(-t/C)$, and solving for time, $t = -C \log(1 - Y/T)$. If Y exceeds the threshold V_{th} , an action potential is said to be generated at time t . Here, we see the effects of the tonic input: as T increases, the inter-spike time decreases (assuming constant capacitance C); therefore, increasing the firing-rate of the neuron, without affecting any other property directly.

The input gain M_g ; however, is not decoupled from the pattern generator's parameters that set frequency. A change from $-0.1e^{-9}$ to $-10.1e^{-9}$ shifts the dominant frequency from 1.9175 rad/sec to 4.5540 rad/sec: a 137.50% change in the coupled pattern generator and system's frequency. Interestingly, as M_g tends towards 0 the amplitude of the coupled system increases. For the aforementioned range, the amplitude ranges from 11.23 to 3.916: decreasing monotonically as M_g decreased. As M_g reaches 0, the frequency of the coupled system is equal to the CPG's natural frequency $\omega_n = 1.7257$ rad/sec and has a peak amplitude equal to 11.23. Describing function analysis shows that M_g has little effect on $N(A, j\omega)$; for $M_g = -0.1e^{-9}$ through to $-1.1e^{-9}$ there was no significant change to $N(A, j\omega)$ about the limit cycle solution's frequency.

Time constants. The main effect of changing the time constants C and τ_w is to change the frequency of the coupled pattern generator and system.

For linear system $L(s)$, with $m = 20$, $b = 2$, and $k = 10$, changing the adaptation time constant τ_w from 0.2 to 2.0 resulted in a frequency shifting from 3.3556 rad/sec to 3.8350 rad/sec: a 14.29% increase in the coupled system's frequency. The output can also vary greatly; for the aforementioned range, the output decreases monotonically from 9.733 to 3.285: a 66.25% decrease. For $\tau_w = 1.0$, corresponding to $\omega = 3.8350$ rad/sec variation of $L(s)$'s stiffness k from 1 to 20 can be evaluated. For the aforementioned range, the dominant frequency changed from 2.1572 rad/sec to 4.3143 rad/sec: a 100% change. These results demonstrate the robustness of the pattern generator to variations in system parameters, and to changes in system $L(j\omega)$.

Altering the neurons' capacitance C time scales the membrane voltage's response; for example, increasing C from 281 pF to 1.405 nF caused the peak output amplitude from 5.289 to 3.228: a 38.97% decrease. In addition, increasing C causes the time to begin entrainment to increase; for 281 pF increasing 1.405 nF, the onset time increased from 0.8362 seconds to 0.9274 seconds: a 10.91% increase

System changes. The pattern generator is also very robust to changes in the system $L(j\omega)$. For example, changing $L(s)$'s damping changes its shape; however, not the frequency. As such, the damping ratio of $L(j\omega)$ can be altered from 0.3 to 0.6, while remaining entrained; the entrained frequency varying from 3.8350 rad/sec to 3.3556 rad/sec: a change of 12.5%, as shown in figure 4-12.

Entrainment. The final aspect of the pattern generator control, which is of practical use, is that it tends to entrain very quickly: usually within one cycle. In this way, it is easy to see the qualitative effects of a parameter on the transient behaviour of the coupled pattern generator and system. With respect to robustness, the pattern generator's ability to entrain to a system adds to the system's robustness since it is able to respond to changes quickly.

4.7 Summary

This chapter described the behaviour of the pattern generators when coupled to a single degree-of-freedom, mechanical system. Analysis using quasi-linearisation-based

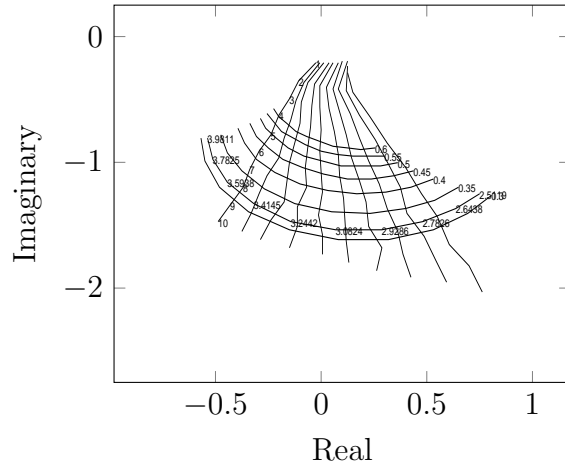


Figure 4-12: SIM Figure showing the effect of varying the damping ratio of the linear system $L(j\omega)$. The plot shows the describing function $N(A, j\omega)$ for the pattern generator, with lines for $L(j\omega)$ indicating different damping ratio values, as marked. The damping ratio can be altered from 0.30 to 0.60 while remaining entrained, with a 12.50% change in the output frequency.

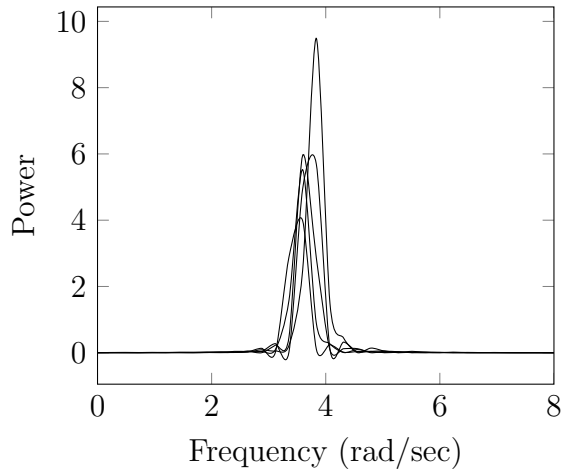


Figure 4-13: SIM Power density spectrum for coupled pattern generator with varying system dynamics. The plot shows power plotted as a frequency, with a clear peak at $\omega = 3.8350$ rad/sec. For a change in damping ratio ζ from 0.3 to $\zeta = 0.6$ (in 0.05 increments) a shift of 12.50% was observed with a subsequent change in power of the system's output signal, decreasing from 9.4872 to 3.1720.

describing functions was introduced, and was shown to be a useful tool for evaluating the pattern generator's output and predicting the behaviour of the coupled system. This analysis reveals a number of principles that apply to the pattern generator's solutions:

- Robustness in parameter settings. Damped and un-damped systems have shown the robustness of the pattern generator to the type of the coupled system. The variation of system characteristics have been shown to have no change on the CPG's describing function $N(A, j\omega)$; furthermore, the effects of varying pattern generator parameters results in monotonic changes, which are decoupled from each other - making it easy to choose working parameters.
- Sensitivity to system changes. Due to the pattern generator's describing function's $N(A, j\omega)$ shape, the CPG is sensitive to coupled system's resonant frequencies; tuning to match them. Fourier transforms and power density spectrum plots have been used to show that indeed the resonant frequency of the output shifts to that of the coupled system.
- Stability of final solutions. Evaluation of the Jacobian matrix's trace $tr(\mathbf{J})$ and determinant $det(\mathbf{J})$ has been used to show whether the coupled system's equilibrium points were stable or unstable nodes or a focus. The respective phase plots of coupled pattern generator and spring-mass or damped-pendulum systems demonstrate the stable limit-cycle behaviour. Finally, the pattern generator's output is characteristic of a stable system, i.e. the transient response doesn't deviate exponentially from a steady-state value as time t tends towards ∞ .
- Synchronisation. The pattern generator generates a motor command, which is dependent on the coupled system's displacement or rotation. The pattern generator is, therefore, sensitive to the joint's motion - changing its output frequency to match the coupled system's natural frequency ω_n . This has been shown for a number of mechanical systems.

Chapter 5

The McKibben Muscle, Antagonistic Actuation, and Antagonistic Controllers

In this chapter, this thesis presents a geometric-based parametrisation of McKibben muscles; evaluating their production of force in the presence of static and dynamic friction terms. In addition, this chapters presents results from differential activation and coactivation of an antagonistically coupled pair of pneumatic muscles. Furthermore, a proposed differential pressure control approach, followed a closed-loop torque controller, are presented. Section 5.1 introduces McKibben actuators, discussing their operation and proposing a means of control. Section 5.2 presents the model used in this thesis. In section 3.4, the methodology of the chapter is presented and how the modelled McKibben msucles are simulated discussed. Section 5.4 presents the results of simulation of the implemented basic and friction models. Section 5.5 presents an antagonistic pairing of muscles, where results from simulation of differential activation and coactivation are presented. Section 5.6 presents the monovariale pressure control approach, followed by the torque controller. Section 5.7 concludes the chapter, discussing the chapter's results.

5.1 Introduction

Hill's muscle model provides a reasonable easy method to account for skeletal muscle's force production; in addition, pneumatic McKibben muscles have been shown to be in agreeance with Hill's three element system [59]. As a consequence, skeletal muscle's phenomenological behaviour can be replicated in the engineering domain.

While literature review has identified a number of different McKibben-like actuators, e.g. Festo's DMSP fluidic muscle [15],pleated muscles [52], and Shadow Robotic's actuators [9]; pneumatic muscles typically consist of an expandable bladder, which is encapsulated by an inextensible mesh braid, whose ends are capped allowing a compressible medium to be injected via an inlet. As the muscle is "inflated", radial expansion causes the mesh braid's pantograph structure to contract, transferring radial force axially. As the muscle contracts, static and dynamic friction damps the muscle; akin to Hill's parallel viscous element's effects. In addition, as the actuator shortens, the braid angle tends towards a maximum, at which no further contraction or force production is possible; phenomenologically similar to skeletal muscle's reduction in tension as a function of decreasing myosin-actin bonding.

A number of McKibben muscle models have been identified in literature, e.g. Hannaford's [8], Tondu's [59], and Klute's [30],[31]. Typically, a pneumatic muscle's force production has been accounted for by taking a geometric-based approach; where, tension has been determined by considering changes in volume as a function of braid angle. Subsequent transformations allow an actuator's force to be expressed as a function of pressure and length; akin to Hill's model length and active force parameters. However, a widely used assumption is that the McKibben muscle maintain a cylindrical shape during contraction, which doesn't account for the actuators end cap's conical constraints. In addition, hysteresis is not accounted for in the simple models; however, the addition of static and dynamic friction coefficients, while increasing modelling's complexity, provide a means to account for decreased and increased force production during contraction and extension, respectively.

As with skeletal muscle, McKibben actuators are entirely contractile; therefore, two muscles need to be connected in antagonism. In this way, extensor and flexor

muscles are able to effect joint rotation given differential activation in this case a pressure difference. Furthermore, by varying said difference in a controlled manner, a pressure-based equilibrium point control can be achieved. In order to provide a set point, a central pattern generator can be used; where, the desired muscles' forces are expressed as a function of the CPG's output and limb joint's angular feedback. In this way, not only can the McKibben muscle's compliance be exploited, but the pattern generator's adaptation can be used to achieve a combination of compliant actuation and adaptive control.

While the differential controller can elicit a joint rotation due to an offset in the muscles' nominal pressure, incorporating an additional control loop enables the CPG to be coupled to the antagonistic actuators via a PD control law. In this way, the pattern generator's angular output can be expressed as a desired torque, which a closed-loop PID controller can track. In effect, the torque controller ensures the CPG's desired quantity of energy is injected into the plant; thus driving it to a coupled resonance.

In the following section, this thesis presents the McKibben muscle model that has been used. Subsequent sections present simulations of static and dynamic friction's effects on the actuator, antagonistic coupling, and presents an antagonistically actuator control paradigm.

5.2 The McKibben Muscle Model

As discussed, the McKibben muscle is, essentially, a mesh braid encapsulated, expandable bladder. When inflated, the textile sheath opens, taking a cylindrical shape, and transforms radial expansion to an axial contraction. To account for the actuator's contractile force production, McKibben muscles have been parameterised by the following variables:

- The initial braid angle, α_0 : the angle measured between the muscle's axis the actuator's individual thread.
- The initial muscle length, l_0 : the nominal muscle length measured along the

muscle's shell.

- The initial radius, r_0 : the radius of the inner bladder in contact with the mesh braid.

where it has been assumed that the braid initially covers the entire bladder, which is supposed to be a thin-wall shell. It should be noted, however, that this assumption can be assumed satisfied if the ratio between the tube thickness and inner tube is [1:10] [59]. As long as the thickness does not exceed this limit, pressure force can be assumed to be fully transmitted to the mesh braid.

Taking the above assumptions to be valid, a McKibben muscle's generated force can be explained by virtue of virtual work. During contraction, the muscle's radius and length changes from r_0 to r and l_0 to l , respectively. If the static force of the muscle is denoted F and extension is assumed to be positive, the virtual work of the equilibrium force against contraction's force is $F\delta l$, where δl is the elementary muscle length variation [59]. The virtual work of pressure force can be expressed as a function of elementary volume variation [8]:

$$P\delta V = -F\delta l \quad (5.1)$$

which can be split into lateral and axial pressure forces [59]:

$$\delta W_{lateral} + \delta W_{radial} + \delta W_{equilibrium} = 0 \quad (5.2)$$

$$\Rightarrow (2\pi r l P)(\delta r) - (\pi r^2 P)(-\delta l) - F(-\delta l) = 0 \quad (5.3)$$

Therefore, F can be determined by considering the volume imposed on the muscle's bladder by the mesh braid. If α is the current mesh braid angle, the the following ratios can be determined [59]:

$$(l/l_0) = \cos \alpha / \cos \alpha_0, \quad \text{and} \quad (r/r_0) = \sin \alpha / \sin \alpha_0 \quad (5.4)$$

$$\Rightarrow r = r_0 \left[\sqrt{1 - \cos^2 \alpha_0 (l/l_0)^2} / \sin \alpha_0 \right] \quad (5.5)$$

Substituting the above relationships into equation (5.2), the McKibben muscle's force can be expressed as a function of contraction ratio and pressure:

$$F(\epsilon, P) = (\pi r)0^2)P [a(1 - \epsilon)^2 - b], \quad 0 \leq \epsilon \leq \epsilon_{Max} \quad (5.6)$$

$$\text{with } \epsilon = (l - l_0)/l_0 \quad (5.7)$$

$$a = 3/\tan^2(\alpha_0), \quad b = 1/\sin^2(\alpha_0) \quad (5.8)$$

From equation (5.6) it is clear, that at $\epsilon = 0$, a maximum force F_{Max} will be produced; in addition, for $F = 0$, the contraction ratio will be at a maximum ϵ_{Max} . The subsequent expressions are given below:

$$F_{Max} = (\pi r_0^2 P(a - b)), \quad \text{for } \epsilon = 0 \quad (5.9)$$

$$\epsilon_{Max} = (1 - \sqrt{b/a}), \quad \text{for } F = 0 \quad (5.10)$$

As discussed, the presented McKibben modelling approach assumes a constant cylindrical shape; whereas, the actuator's ends are in fact conical. Consequently, the more the muscle contracts the more the active part decreases [59]; resulting in an actual maximum contraction ratio less than that of equation (5.9)'s. To account for this, an experimentally determined constant k can be added to equation (5.6). The modified force model is given by:

$$F(\epsilon, P) = (\pi r)0^2)P [a(1 - k\epsilon)^2 - b], \quad 0 \leq \epsilon \leq \epsilon_{Max} \quad (5.11)$$

where the maximum contraction ratio is given by:

$$\epsilon_{Max} = (1/k)(1 - \sqrt{b/a}), \quad \text{for } F = 0 \quad (5.12)$$

Equation (5.11) forms the basis of the model used in the subsequent sections.

5.3 Methodology

In this chapter, this thesis presents a number of simulations, which have been carried out in MathWorks' Simulink environment in order to determine the McKibben muscle's static and dynamic properties, how the muscles perform in antagonism, i.e. in response to differential activation and coactivation; and their suitability for use in conjunction with a pattern generator, with application to assistive device control. In the following section, an implementation of the McKibben muscle model of section 5.2, the parameters of which have been taken from literature [59], is presented.

Initially, two simulations have been performed: static modelling, where only the volumetric change in the muscle is modelled; and dynamic modelling, where static and dynamic friction coefficients are incorporated with the model. In either case, the muscle model's contractile and extensile tension is plotted as a function of a 0.1 m change in length applied at 0.1 m/sec, and the static and dynamic forces compared.

Following that, two of the implemented muscle models are connected in antagonism and a further two simulations are performed: differential activation, where the extensor has an increasing pressure ranging from 1 bar to 5 bar applied to it, while the flexor's is held constant at 1 bar; and coactivation, where an equal pressure ranging between 1 bar and 5 bar is applied and the system perturbed. In this simulation, the coupled muscles actuate a limb segment modelled as a critically damped pendulum of mass $m = 0.3$ kg and length $l = 0.35$ m. The coactivated system's disturbances are first applied distally as a step of 10 N at time $t = 1$ sec, followed by a 100 ms pulse of equal magnitude at time $t = 1$ sec.

Having simulated the McKibben muscles in their predicted usage, a proposed differential pressure controller is presented and simulations performed; where, pressure differences ranging between 0 bar and 2 bar are shown to elicit a changing in the modelled limb's joint angle. Subsequently a closed-loop torque controller is presented, where set points between 0 Nm and 1 Nm are applied and the evoked joint rotation recorded.

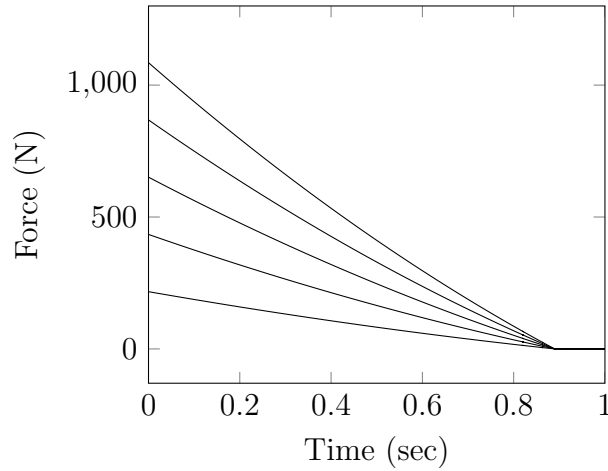


Figure 5-1: SIM Plot of the basic McKibben muscle model’s force production as a function of contraction ratio. In this example $l_0 = 0.30$ m, $r_0 = 0.007$ m, $\alpha_0 = 20$ deg, and $P = [1,2,3,4,5]$ bar.

5.4 Static and Dynamic Modelling

In this section, the results from simulation of the McKibben model, which has been implemented in MathWork’s Simulink environment, are presented.

In this first part of simulation, the basic model’s force production, as a function of contraction and extension, is considered. For a muscle of initial length $l_0 = 0.30$ m, initial radius r_0 , and initial braid angle a_0 , and a 0.1 m ramp change in length applied at 0.1 m/s, figure 5-1 depicts the basic McKibben muscle model’s force production. It can be seen that as pressure P increases from 1 bar to 5 bar, the muscle’s generated force increases from 217.01 N to 1085.10 N: an approximately 400 % increase.

In the second part of the simulation, the basic model has an additional frictional term added to it. First, a static frictional term taken from literature [59] has been used to account for the decreased and increased force produced during contraction and extension. It is assumed that the mesh braid in contact with the internal bladder is rigidly locked during contraction, fulling transferring pressure from the inner tube to the braid. Here the frictional term is considered to be a property of the mesh

braid's internal workings; where, the following equation has been used:

$$|F_{Static}| = f_s(1/n)S_{Contact}P \quad (5.13)$$

where f_s is the static friction constant, $S_{Contact}$, the surface contact coefficient; P , the muscle's pressure; and n , the ratio of lateral contact constant. Incorporating the term $\text{sign}(dl/dt)$ defines the sign of the friction term: positive for extension, negative for contraction. The surface contact coefficient is expressed by the following:

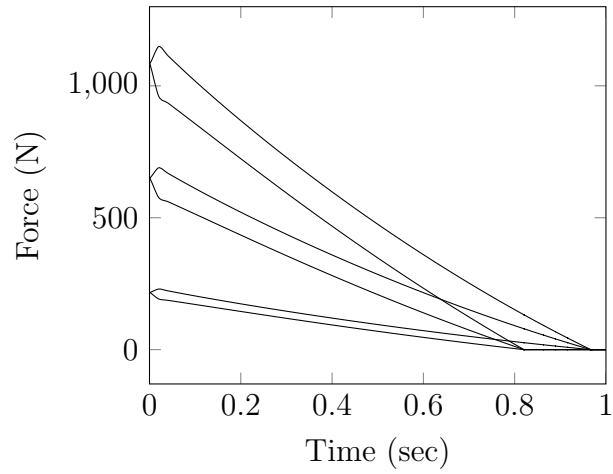
$$S_{Contact} = (2\pi(r_0l_0)) \frac{\sin \alpha_0}{(1 - k\epsilon)\sqrt{1 - \cos^2 \alpha_0(1 - k\epsilon)^2}} \quad (5.14)$$

For a muscle of initial length $l_0 = 0.3$ m, initial radius $r_0 = 0.007$ m, and initial braid angle of 20 deg, and a 0.1 m ramp change in length applied at 0.1 m/s, figures 5-2(a) and 5-2(b) depict the static friction term's effects on force production given a static friction coefficient $f_s = 0.1950$ and pressure $P = [1,3,5]$ bar and $P = [2,4]$ bar, respectively. As before, it can be seen that as pressure P increases, the overall force increases from 217.01 N to 1085.10 N; however, under contraction, the resulting force is less than that shown in figure 5-1; whereas, under extension, the force is greater than shown in the previous figure. As pressure P increases to its maximum value, the static friction term's effect becomes more pronounced; increase the contraction and extension force's difference from 37.56 N at 1 bar to 187.83 N at 5 bar: a 400 % increase. This, however, can be explained by evaluating equation (5.13), where P effectively acts as a gain.

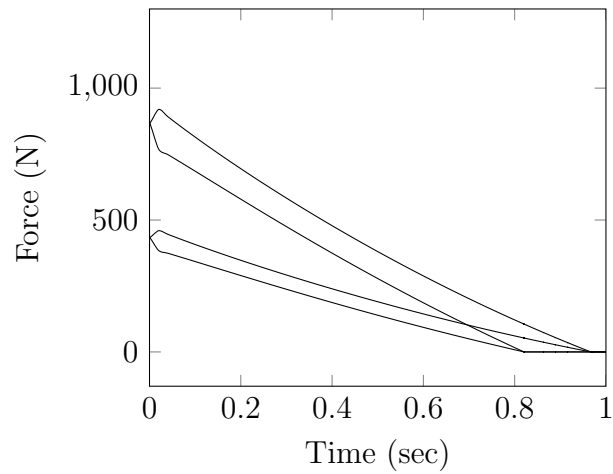
In considering dynamic friction, a frictional term taken from literature [59] has been used to describe the contraction-extension's hysteresis loop. The dynamic dry friction coefficient f has been expressed as a function of the following three term relationship:

$$f = f_k + (f_s - f_k) \exp(-\dot{l}/x_s) \quad (5.15)$$

where f_s is the static coefficient; f_k , the maximum kinetic coefficient; \dot{l} , the muscle length's rate of change; and x_s , a velocity constant. In addition, it has been shown that equation (5.15) is in agreement with Hill's modelling of muscle's damping [59].



(a)



(b)

Figure 5-2: SIM Plot of the static friction-incorporating McKibben muscle model's force production as a function of contraction ratio. Figure (a) depicts the muscles' produced contractile and extensile forces for pressure $P = [1,3,5]$ bar. Figure (b) depicts the muscles' produced contractile and extensile forces for pressure $P = [2,4]$ bar. In this example $l_0 = 0.30$ m, $r_0 = 0.007$ m, $\alpha_0 = 20$ deg, and $f_s = 0.1950$.

The subsequent friction term is given by the following:

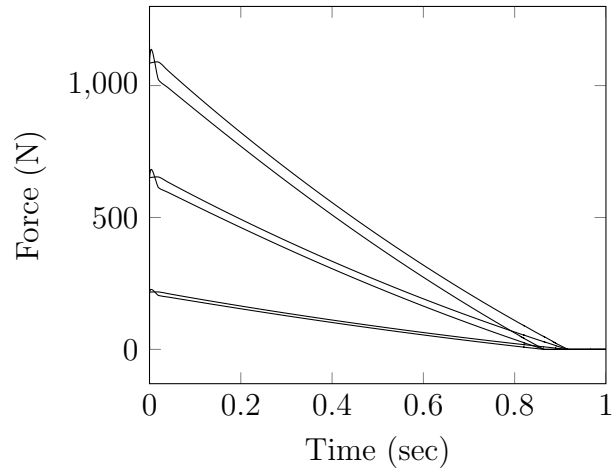
$$|F_{Dynamic}| = f(1/n)S_{Contact}P \quad (5.16)$$

where $S_{Contact}$ is the aforementioned surface contact coefficient; P , the pressure; and n , the ratio of lateral contact constant.

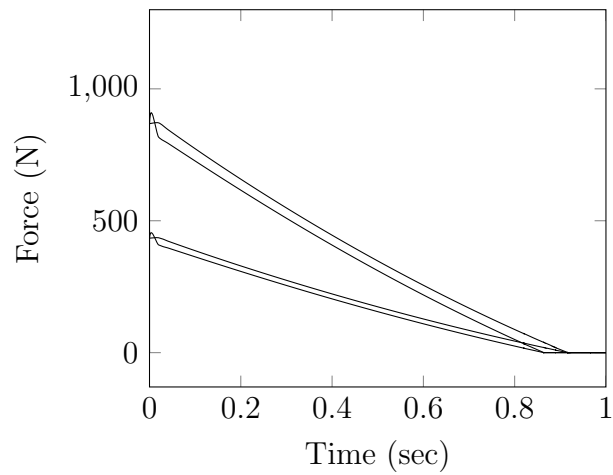
For a muscle of initial length $l_0 = 0.30$ m, initial radius $r_0 = 0.007$ m, initial braid angle of 20 deg, and a 0.1 m ramp change in length applied at 0.1 m/s, figures 5-3(a) and 5-3(b) depict the dynamic friction term's effects on force production given $f_s = 0.1950$, $f_k = 1.3650$, and pressure $P = [1,3,5]$ bar and $P = [2,4]$ bar, respectively. It can be seen, as before, that as pressure increases, the overall force produced increases; ranging from, initially, 217.01 N to 1085.10 N. In addition, as P increases, the dynamic frictions effect on contractile and extensile force also becomes more pronounced; however, by not as much: increasing from 13.54 N at 1 bar to 67.70 N at 5 bar. In the dynamic friction's case, the hysteresis loop's force variation is approximately a third of that of the static case's, which, according to Tondu [59], results in a closer agreeance with experimental results.

5.5 Antagonistic Coupling

As discussed, a key reason to investigate antagonism is two fold: to account for differential activation, where a difference in extensor and flexor activation results in rotation of a limb's joint; and to quantify coactivation, where the paired muscles both receive equal activation, effects on joint stiffness and stability. In terms of an antagonistic coupling of Hill-type muscles, it has been shown that increasing an extensor's active force in the present flexor active force produces a joint oration of up to 0.459 rad, or 26.30 deg; in addition, applying an increased, but equal, active force to the coupled muscles increases the stiffness of the joint, rejecting perturbations. in this section, this thesis presents an antagonistically coupled pair of McKibben muscles, which have been implemented in MathWorks' Simulink environment; where, differential and coactivation simulations have been carried out.



(a)



(b)

Figure 5-3: SIM Plot of the dynamic friction-incorporating McKibben muscle model's force production as a function of contraction ratio. Figure (a) depicts the muscles' produced contractile and extensile forces for pressure $P = [1,3,5]$ bar. Figure (b) depicts the muscles' produced contractile and extensile forces for pressure $P = [2,4]$ bar. In this example $l_0 = 0.30$ m, $r_0 = 0.007$ m, $\alpha_0 = 20$ deg, $f_s = 0.1950$, and $f_k = 1.3650$.

In the first simulation, the extensor McKibben muscle's pressure has been increased from 1 bar to 5 bar, in 1 bar increments, applied at time $t = 1$ sec, while the flexor actuator's pressure is fixed at 1 bar. As with the antagonistic coupling of Hill-type muscles, a limb has been modelled as a critically damped pendulum of mass $m = 0.30$ kg and length $l = 0.35$ m. Consequently, the plant's transfer function is given by:

$$L(s) = \frac{1}{0.0367s^2 + 0.39s + 1.03} \quad (5.17)$$

In addition, both muscles act about the limb's joint through a moment arm $R = 0.05$ m.

For an initial muscle length $l_0 = 0.30$ m, initial radius $r_0 = 0.007$ m, initial braid angle $\alpha_0 = 20$ deg, and static friction coefficient $f_s = 0.1950$, figure 5-4 shows the joint angle's transient response to an extensor pressure $P = [1,2,3,4,5]$ bar increased at time $t = 1$ sec. It can be seen that as P increased 1 bar through to 5 bar, the angular displacement increased from 0 rad to a maximum 0.8333 rad; almost double that achieved by antagonistic coupling of two Hill-type muscle models. Furthermore, as P increases, the peak displacement's time changes from 1.1420 sec to 1.040 sec: a 3.327 % decrease. In addition, the transient response's settling time (within 5 % of the steady-state value) rises from 1.2361 sec to 1.414 sec: a 16.167 increase. In the second part of the simulation, two coactivation scenarios have been considered: first, when a constant 10 N disturbance is applied distally at time $t = 1$ sec; and secondly, when a load of equal magnitude is applied at time $t = 1$ sec for a 100 ms duration. In both cases, the extensor and flexor muscles pressure P is increased equally from 1 bar to 5 bar in 1 bar increments. As before, a limb of mass $m = 0.3$ kg and length $l = 0.35$ m, modelled as a damped pendulum, has been used. For an initial muscle length $l_0 = 0.30$ m, initial radius $r_0 = 0.007$ m, and static friction coefficient $f_s = 0.1950$, figure 5-5(a) shows the joint angle's transient response to the constant load given pressure $P = [1,2,3,4,5]$ bar. It can be seen that the peak displacement, which changes from 0.36 rad to 0.0807 rad, decreases in response to an increased degree of coactivation. In addition, the response of the coactivated joint is far less oscillatory compared to the differentially activated response of figure 5-4;

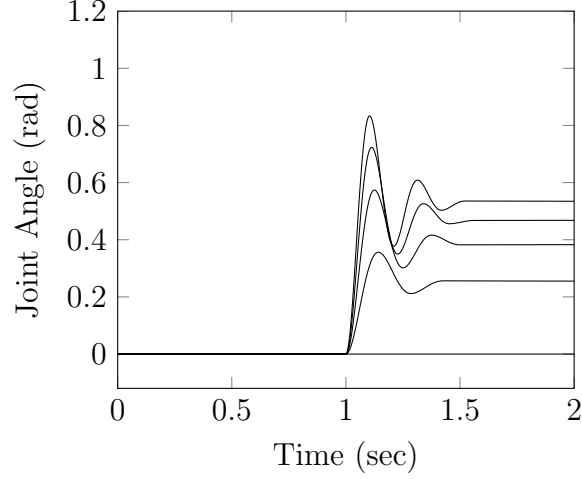
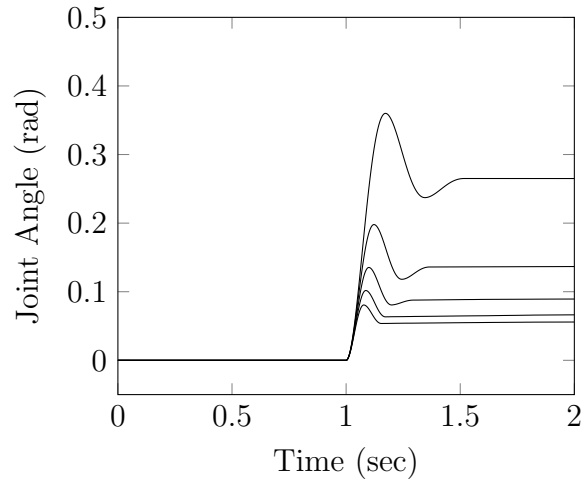
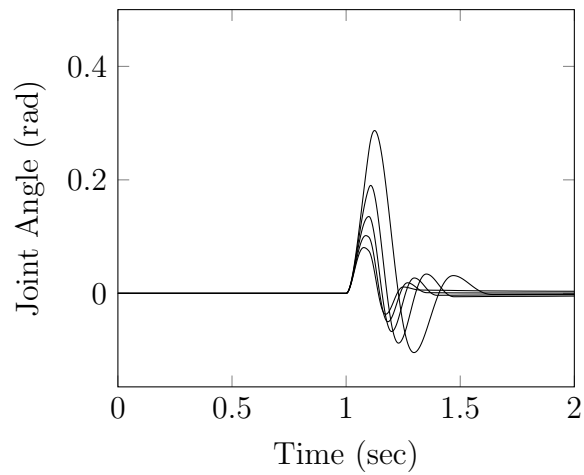


Figure 5-4: SIM Plot of differential activation of antagonistically coupled McKibben muscles. Here, the extensor muscle's pressure $P = [1,2,3,4,5]$ bar for a constant flexor pressure $P = 1$ bar. In this example $l_0 = 0.30$ m, $r_0 = 0.007$ m, $\alpha_0 = 20$ deg, and $f_s = 0.1950$.

whose peak displacement's time decreases from 1.1728 sec to 1.0770 sec: an 8.168 % decrease. In addition, the transient response's settling time (within 5 % of the steady-state value) changes from 1.2992 sec to 1.1520 sec: an 11.33 % decrease. With respect to the second scenario, the antagonistically coupled muscles are identical to the previous cases. Figure 5-5(b) depicts the joint angle's transient response to a 10 N load applied distally for a 100 ms duration given pressure $P = [1,2,3,4,5]$ bar. It can be seen that the peak displacement decreases as the degree of coactivation increases; reducing from a maximum of 0.2869 rad at 1 bar to 0.0807 rad at 5 bar. Furthermore, as P increases, the displacement's peak time reduces from 1.1250 sec to 1.0760 sec: a 4.356 % decrease. In addition, the settling time (within 5 % of the steady-state value) changes from 1.6286 sec to 1.327 sec: an 18.519 % decrease.



(a)



(b)

Figure 5-5: SIM Plot of coactivation of antagonistically coupled McKibben muscles. Figure (a) depicts the joint angle's transient response to a constant 10 N perturbation applied distally to the modelled limb at time $t = 1$ sec given pressure $P = [1,2,3,4,5]$ bar. Figure (b) depicts the joint angle's transient response to a 10 N disturbance applied distally at time $t = 1$ sec for a duration of 100 ms given pressure $P = [1,2,3,4,5]$ bar. In this example $l_0 = 0.30$ m, $r_0 = 0.007$ m, $\alpha_0 = 20$ deg, and $f_s = 0.1950$.

5.6 Antagonistic Actuator Control Paradigm

As discussed, the combination of a pattern generator and a limb joint antagonistically actuated by McKibben muscles allows for both the actuator's compliance and the CPG's adaptation to be utilised, with potential application to assistive devices. However, the pattern generator's singular output, typically, is expressed in terms of a desired angle; whereas, each McKibben muscle is individually controlled by a corresponding pressure. In this section, this thesis presents a differential pressure control approach, which builds upon the previous section's differential activation concept; followed by a closed-loop PID torque controller, which incorporates the differential pressure controller.

With respect to the differential pressure controller, the underlying principle is to use a mono-variable based approach to controlling the antagonistic extensors and flexor's pressure by adding and subtracting a pressure offset from the actuators' nominal pressure. If the pressure is expressed as dP , the subsequent muscle pressures can be expressed as:

$$P_E = P_0 + dP \quad (5.18)$$

$$P_F = P_0 - dP \quad (5.19)$$

where P_0 is the nominal pressure; and P_E and P_F are the extensor and flexor supply pressure, respectively.

In using a monovariable approach, a single input (dP) and single output (θ) control methodology has been developed. Furthermore, by reducing the system to a single input and single output, it is possible to use classical controllers, e.g. PID [45]. To demonstrate the differential pressure controller's functionality, simulations of an antagonistically actuated limb have been carried out in MathWorks' Simulink environment. Given an initial muscle length $l_0 = 0.3$ m, initial radius $r_0 = 0.007$ m, initial braid angle α_0 , and static friction coefficient $f_s = 0.1950$, figure 5-7 depicts the joint angle's transient response to a pressure difference $dP = [0,0.5,1.0,1.5,2.0]$ bar applied at time $t = 1$ sec. It can be seen that as the pressure difference dP increases,

Figure 5-6: Schematic of the torque controller, differential pressure controller, antagonistic muscles, and modelled limb. A torque set-point τ_d and measured torque τ_m are input into a summing junction, whose output e , the error signal, is passed to the PID controller. The controller's output dP is passed to the differential pressure controller ΔP , which in turn drives the antagonistic extensor and flexor muscle. The corresponding torque produced is measured and the loop closed.

so too does the joint's angle; ranging between a peak displacement of 0.1898 rad at 0.5 bar to 0.8333 rad at 2.0 bar, before settling to steady state values of 0.1280 rad and 0.5353 rad at 0.5 bar and 2.0 bar, respectively. In addition, the settling time changes from 1.261 sec to 1.402 sec: an 11.182 % increase.

Based on the response of the differential controller's output, a key conclusion that can be drawn is that the approach is able to effect open-loop control of an antagonistically coupled pair of McKibben muscles; however, the transient response (see figure 5-7) tends to be oscillatory; increasing in frequency as dP increases. An alternative control approach is to incorporate a closed-loop PID controller, whose set-point is a desired torque and control action is the corresponding pressure difference. Figure 5.6 depicts schematically the torque controller approach.

In order to validate the torque controller approach, simulations have been carried out in Simulink; where, the same antagonistic system and modelled limb have been used and a desired torque $\tau_d = [0.1, 0.2, 0.3, 0.4, 0.5]$ Nm has been used as an input in place of dP . In this simulation, the PID controller's proportional gain k_c , integral gain k_i , and differential gain k_d have been experimentally determined as 100, 10, 5, respectively. Figures 5-8(a) and 5-8(b) depict the joint angle's transient response for 1 bar and 3 bar nominal pressures; where, an immediate consequence of the closed-loop controller is obvious: the oscillatory response of the previous control approach has been eliminated, tracing a first-order, step-like response. It can be seen that joint angle's transient response ranges from 0.0969 rad to 0.4847 rad for 1 bar nominal pressure; through to 0.0936 rad to 0.4697 rad for a 3 bar nominal pressure. In addition, the transient response's rise time remains relatively constant at 0.393 sec for both 1 bar and 3 bar nominal pressure.

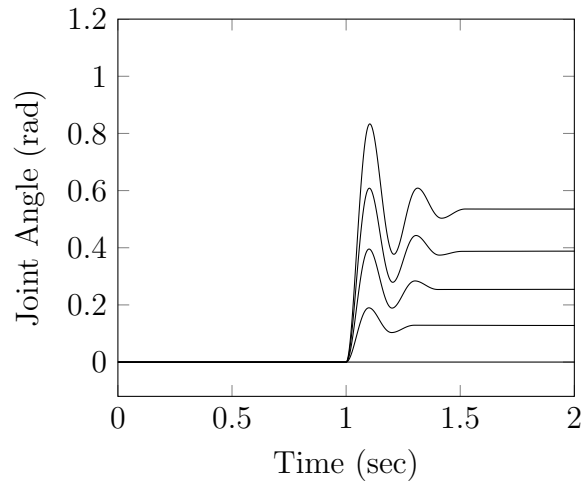
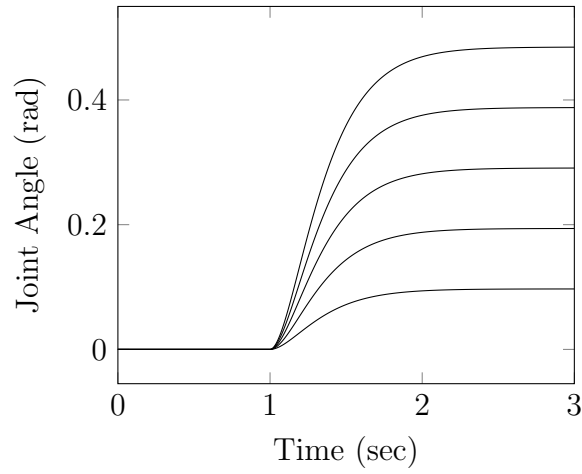


Figure 5-7: SIM Plot of differential pressure controller evoked joint angle's transient response to a pressure difference $dP = [0,0.5,1.0,1.5,2.0]$ bar applied at time $t = 1$ sec. In this example $l_0 = 0.30$ m, $r_0 = 0.007$ m, $\alpha_0 = 20$ deg, $f_s = 0.1950$, and $P_0 = 3$ bar.

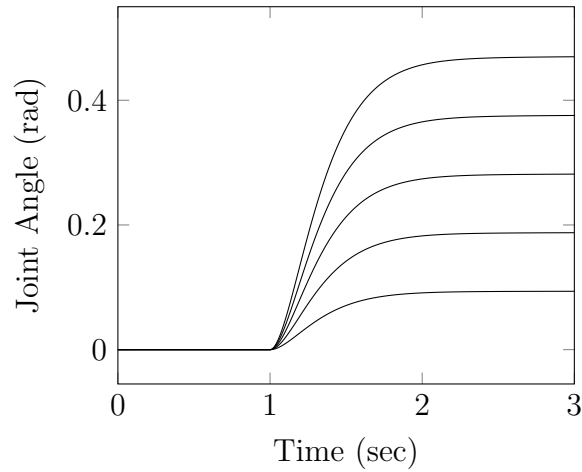
5.7 Summary

In this chapter, the operation of the McKibben muscle has been discussed, a geometric-based parametrised model presented, and results from simulation of the basic and friction-incorporating muscle models have been presented. To account for a joint's rotation, two McKibben actuators have been connected in antagonism and results from simulation of a modelled limb under differential activation and coactivation have been presented. Subsequently, a differential pressure control approach has been discussed; which is improved upon by including a closed-loop torque controller. Simulation of both control methods has demonstrated their merits.

It has been demonstrated that the basic McKibben model doesn't account for muscle's variation in force during change in length; whereas, incorporation of a friction term has been shown to result in a difference in generated tension during contraction and extension. The inclusion of a static friction term represents a "worst case" hysteresis scenario; where, the difference in generated force ranged from 37.5586 at 1 bar to 187.8253 N at 5 bar for $f_s = 0.1950$: approximately 3 times that produced



(a)



(b)

Figure 5-8: SIM Plot of the torque controller's evoked joint angle's transient response to a desired torque $\tau_d = [0.1, 0.2, 0.3, 0.4, 0.5]$ Nm applied at time $t = 1$ sec. Figure (a) depicts the joint angle's transient response given τ_d and a nominal pressure $P_0 = 1$ bar. Figure (b) depicts the joint angle's transient response give τ_d and a nominal pressure $P_0 = 3$ bar. In this example $l_0 = 0.30$ m, $r_0 = 0.007$ m, $\alpha_0 = 20$ deg, and $f_s = 0.1950$.

in the dynamic friction's case (13.5396 N at 1 bar and 67.6978 N at 5 bar). In either case, the inclusion of a friction term resulted in an output that tended to be more congruent with experimental data [59], compared to the basic model.

With respect to antagonistic actuator; under differential activation, it has been demonstrated that a maximum rotation of 0.8333 rad was achieved, given the extensor and flexor muscles received a pressure of 5 bar and 1 bar, respectively. Under coactivation, it has been shown that an increased, equally applied, pressure P resulted in a reduced joint angle displacement in response to a constant 3.5 Nm disturbance: decreasing from 0.36 rad at 1 bar to 0.0807 rad at 5 bar. In addition, when a disturbance of equal magnitude was applied over a duration of 100 ms, an increased P also resulted in a reduced peak displacement: decreasing from 0.2869 rad at 1 bar to 0.0807 at 5 bar. A key conclusion drawn, it that an increased degree of coactivation results in an increased joint stiffness; reducing the effects of limb joint perturbation. In either case, it has been found that a minimum nominal pressure $P = 0.6$ bar is required for the extensors and flexor's muscle lengths to remain bounded within the range $[0, \epsilon_{Max}]$, which is important, because, if the muscles reach the bound's limits, undesirable oscillatory behaviour is introduced into the joint angle's transient response.

In terms of the discussed differential pressure controller, a monovariate control approach has been presented; however, the evoked joint rotation has been shown to become increasingly oscillatory as the pressure dP incremented; where, the settling time increased from 1.261 sec for $dP = 0.5$ bar to 1.402 sec for $dP = 2.0$ bar. To overcome undesirable transient response behaviour, a closed-loop torque controller has been presented; where, for a desired torque τ_d , an angular displacement ranging from 0.0969 rad for $\tau_d = 0.1$ Nm to 0.4847 rad for $\tau_d = 0.5$ Nm has been demonstrated. A key observation that can be made is that the torque controller leads to a much more desirable transient response: tracing a step-like path.

Chapter 6

Assistive Device Controller and Antagonistic Actuator

In this chapter, this thesis presents an assistive device controller, which builds upon the previous chapter's antagonistic actuator's torque and differential pressure controllers; incorporating the discussed central pattern generator. In addition, fabricated McKibben muscles are presented; where, experimental results demonstrate their force production as a function of pressure, which is fitted to a series of polynomial curves and used to optimise the presented muscle models. Subsequently, a fabricated antagonistic actuator and realised controller are presented, on which a number of experiments are used to validate the discussed assistive device control approach.

In section 3.1 the pattern generator, McKibben muscle model, and the control paradigm are discussed. Section 6.2 presents the chapter's methodology; where, how the McKibben muscle's are experimented with, curves fitted, model optimised, and antagonistic experiments are carried out discussed. Section 6-3 through section 6.3 present the McKibben muscle's experimental results, their fitted curves, and the optimised parameters. Section 6.4 presents the results of static and dynamic simulation of the control paradigm and a modelled limb. Section 6.5 presents the antagonistic actuator and the realised controller. Section 6.6 presents the results

of static and dynamic experimentation with the coupled antagonistic actuator and realised controller. Section 6.7 closes the chapter; discussing key conclusions.

6.1 Introduction

In previous chapters, the need for adaptive control and compliant actuation has been discussed; identifying current technologies' lack of compliance and intelligence as being a key impedance to the development of active assistive devices. As such, the biological nervous system has been looked to for inspiration; where, literature review has identified the role neurons, muscles, and central pattern generators play in effecting locomotions and voluntary movement's desirable behaviour. Subsequently, this thesis has implemented and developed Simulink models of the neuron, muscle, and central pattern generator; demonstrating the qualitative and quantitative behaviour of each component. Building upon the fact that pneumatic McKibben muscles have been shown to be congruent with Hill's muscle model [59], this thesis has also modelled and implemented the actuators in Simulink; proposing a number of antagonistic control methodologies.

Up to this point, it has been shown that pattern generators are capable of autonomously generating output in the absence of feedback; however, once an input is applied, the CPG entrains to it. Furthermore, antagonistic coupling of McKibben muscles have demonstrated a compliant means of actuation; which, when coupled with a closed-loop torque controller, is able to generate smooth joint rotation. In this chapter, a combination of central pattern generator and antagonistic McKibben muscles is presented: the "assistive device controller"; where, the governing equations of

the CPG are given by:

$$C \frac{dV_1}{dt} = T - w - g_L (V_1 - E_L) + g_L \Delta_T \exp\left(\frac{V_1 - V_T}{\Delta_T}\right) - V_1 - Y_g[Y_2]^+ - \Sigma Mg [M_n]^+ \quad (6.1)$$

$$\tau_w \frac{dw}{dt} = a(V - E_L) - w \quad (6.2)$$

$$Y_1 = \frac{t}{e} \exp\left(\frac{-t}{e}\right) * \delta(t - t_1) \quad (6.3)$$

$$C \frac{dV_2}{dt} = T - w - g_L (V_2 - E_L) + g_L \Delta_T \exp\left(\frac{V_2 - V_T}{\Delta_T}\right) - V_2 - Y_g[Y_1]^+ - \Sigma Mg [M_n]^- \quad (6.4)$$

$$\tau_w \frac{dw}{dt} = a(V - E_L) - w \quad (6.5)$$

$$Y_2 = \frac{t}{e} \exp\left(\frac{-t}{e}\right) * \delta(t - t_2) \quad (6.6)$$

$$Y_{Out} = [Y_1]^+ - [Y_2]^+ \quad (6.7)$$

At spike time t_n ($V > -20mV$) : $V \rightarrow E_L$, and $w \rightarrow w + b$

and the antagonistic muscles modelled by:

$$F(\epsilon, P) = (\pi r) 0^2 P [a(1 - k\epsilon)^2 - b] - f_s(1/n) S_C \text{sing}(\dot{l}), \quad 0 \leq \epsilon \leq \epsilon_{Max} \quad (6.8)$$

Figure 6-1 depicts the assistive device control paradigm. The CPG generates a desired trajectory θ_d , which along with angular feedback θ_m , is passed to a PD controller given by:

$$\tau_d = k(\theta_d - \theta_m) - b(\dot{\theta}_m) \quad (6.9)$$

where k is the coupling stiffness; b , the coupling damping; θ_d , desired angle; and θ_m , measure angle. The subsequent output τ_d is then passed to the antagonistic actuator sub-system, whose torque controller tracks the set-point, generating a torque τ that acts upon the plant. The plant's joint angle is passed back to the antagonistic actuators, PD controller, and pattern generator, closing the feedback loop.

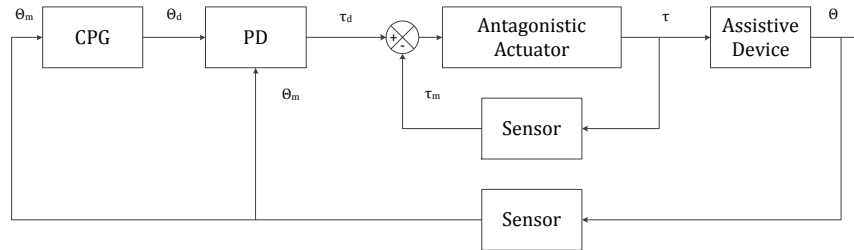


Figure 6-1: Assistive device’s control paradigm’s schematic. The pattern generator is coupled to the antagonistic actuators via a PD control law, whose output is the desired torque τ_d . The antagonistic actuator’s torque controller follows the input, generating a corresponding torque τ that acts upon the plant. The plant’s angle θ_m is fed back into the antagonistic actuator, PD controller, and CPG closing the loop.

In the following section, this thesis presents the methodology used to determine the assistive device controller’s actuator properties, discussing their force curve fitting and model parameter optimisation; followed by outlining control paradigm simulation and antagonistic actuator, realised control experimentation methodology.

6.2 Methodology

In this chapter, this thesis presents a novel assistive device control paradigm, which utilises an antagonistic coupling of fabricated McKibben muscles and central pattern generator. Subsequently, the control approach is implemented on an embedded target and used to control a fabricated antagonistic actuator.

In the following section, the McKibben muscles used herein are presented and the process of fitting curves to experimentally determined force-length vectors discussed, results presented, and model parameters optimised. In order to determine the muscle’s force-length relationship, the T30K tensionometer (see 6-2), Festo VPPE proportional-pressure regulator, and power supply have been used. Given a 0 - 10 V signal, the regulator produces a proportional pressure $P = [0:10]$ bar at a rate of 1 bar/volt. However, since the airline’s maximum pressure was, approximately 6 bar, a maximum of 5 bar has been used. Each muscle was loaded into the test-rig,

pressure applied, and their length changed at a rate of 1 mm/sec, while the produced force was recorded.

Having determined the McKibben muscle model's optimum parameters, a combination of antagonistic pair of actuators and central pattern generator is presented and static and dynamic simulations, where a tonic CPG input T is applied, are carried out. In the static case, a modelled limb is allowed to oscillate unperturbed; however, in the dynamic case, a constant 10 N load is applied distally at time $t = 15$ sec. In either case, the assistive device controller and limb joint angle's transient response is plotted as a function of CPG activation T .

Finally, a fabricated antagonistic actuator and realised controller, consisting of an antagonistic coupling of the fabricated muscles, VPPE proportional-pressure regulators, power supply unit, BeagleBoard, and Arduino Uno, are presented. The assistive device controller's Simulink model is deployed to the BeagleBoard, where it runs in real-time; driving the extensor and flexor regulators via the Arduino Uno. Subsequently, experimentation with the apparatus has been carried out and the results of free and perturbed oscillation presented.

6.3 Fabricated McKibben Muscle

As discussed, the McKibben muscle, in essence is an expandable bladder, encapsulated in a mesh braid, whose ends are closed, though allow air (or any compressed medium) to be injected via an inlet. In this section, the thesis' fabricated McKibben muscles are presented, and force curve fitting and model optimisation performed.

Figure 6-3 depicts the actuator that has been made. Its nominal length and radius were $l_0 = 0.26$ m and $r_0 = 0.006$ m, respectively. Here, the inner bladder was made from a silicon tube, whose outer radius and thickness was approximately 12 mm and 1.3 mm, respectively. The corresponding thickness to outer diameter ratio [1.3:12], which is approximately equivalent to [1:10], is sufficient to assume that the silicon tube acts as a thin wall pressure vessel; transferring all force to the mesh braiding, as discussed. The muscle's mesh braid was made from nylon and had a minimum and maximum diameter of 0.014 m and 0.018 m, respectively.



Figure 6-2: McKibben muscle's testing apparatus. Shown is a JJT30K tensionometer and a FESTA DMSP fluidic muscle.



Figure 6-3: Fabricated pneumatic McKibben actuator used in this chapter, whose parameters have been experimentally determined, as discussed in subsequent sections. Here, the initial muscle length $l_0 = 0.26$ m and initial radius $r_0 = 0.006$ m.

The actuator was assembled by inserting a length of pre-cut silicon into a length of mesh braiding in excess of the silicon tubing. Next, the end caps were inserted into the inner tube and hose clamps placed around the end cap, braid, and silicon tube. The mesh braid was pulled through the one clamp until the braid was firmly affixed against the inner tube; at which point, the clamp was tightened and closed. The previous step was then repeated for the remaining end.

Once the actuator was fabricated, its force-length relationship was experimentally determined through use of the T30K tensionmeter of figure 6-2. Having placed the muscle into the test-rig's end effectors, pressure $P = [1,2,3,4,5]$ bar was applied and its length allowed to gradually shorten at a constant rate of 1 mm/sec until the produced force $F = 0$ N; at which point, the direction was reversed and the muscle extended until its length $l = l_0$. In this way, the force-length characteristics of the actuator were captured over a wide range of pressures.

In the following section, the curves fitted to the recorded force-length vectors are presented; subsequently, they are used to optimise the parameters of a model of the fabricated McKibben muscle.

Curve Fitting

Having determined the fabricated McKibben muscle's produced force as a function of pressure $P = [1,2,3,4,5]$ bar, MathWorks' curve fitting tool (cftool) was used to determine a series of fitted curves, which accounted for the variation in measured response.

Initially, each pressure's force and length vectors were pre-processed; separating them into three vectors: f_{Con} , f_{Ex} , and x , which corresponded to contraction and extension phases' produced force and the JJT30K's end effector's height as a function of muscle's length change ($x = 100 - \Delta l$, where $\Delta l = l_0 - l$).

Subsequently, a new curve fitting session was created for the corresponding f_{Con} , f_{Ex} , and x vectors, and their according pressure. Separate fits were made for the contraction and extension forces; where, a third order polynomial was found to offer the best fit, with regression's coefficient of determination R^2 values of up to 0.9929 achieved. Higher order equations offered no significant improvements, especially as pressure P tended towards 5 bar.

Given pressure $P = [1,2,3,4,5]$ bar, table 6.1 through table 6.5 tabulate the fitted curves' parameters; in addition, figures 6-4 and 6-5 depict the fitted force curves as functions of a ramp change in length applied at 1 mm/sec given $P = [1,3,5]$ and $P = [2,4]$ bar, respectively. Comparing table 6.1 through table 6.5, it is evident that the lower the pressure, the lower the regression fits the data; furthermore, at $P = 1$ bar, the fitted curve is the least able to describe f_{Con} and f_{Ex} , where $R^2 = 0.5764$. However, it should be noted that the McKibben muscle performs poorly at low pressure; an issue identified in literature's experimentation [8][59]. As such, the performance of the actuator at $P = 1$ bar has been treated as an outlier and ignored in subsequent model parameter optimisation. For pressure $P \geq 1$ bar, the fitted curves were, increasingly, able to predict the measured contractile and extensile force, where R^2 increased from 0.9377 at $P = 2$ bar (see table 6.2) through to $R^2 = 0.9929$ at 5 bar (see table 6.5).

Parameter Optimisation

After determining the fabricated McKibben muscles' fitted force curves, they were used to optimise the presented McKibben muscle model presented in equation (6.8); where, Simulink's parameter estimation tool was used. Here, the known parameters were the initial length $l_0 = 0.26$ m and initial radius $r_0 = 0.006$ m. The unknown parameters optimised were the initial braid angle α_0 , static coefficient of friction,

Table 6.1: Table of the fabricated McKibben muscle's fitted force curve's parameters given pressure $P = 1$ bar, $l_0 = 0.26$ m, and $r_0 = 0.006$ m.

	Contraction	Extension
Linear model Poly1:		
$f(x) = p1*x + p2$		
Coefficients:		
p1 =	-0.00136	-0.001993
p2 =	0.01088	0.01523
Goodness of fit:		
SSE:	0.002808	0.002416
R-square:	0.5764	0.753
Adjusted R-square:	0.5754	0.7523
RMSE:	0.002601	0.002576

Table 6.2: Table of the fabricated McKibben muscle's fitted force curve's parameters given pressure $P = 2$ bar, $l_0 = 0.26$ m, and $r_0 = 0.006$ m.

	Contraction	Extension
Linear model Poly3:		
$f(x) = p1*x^3 + p2*x^2 + p3*x + p4$		
Coefficients:		
p1 =	-1.065e-06	-2.16e-06
p2 =	5.562e-05	8.868e-05
p3 =	-0.002076	-0.002738
p4 =	0.03465	0.04508
Goodness of fit:		
SSE:	0.005421	0.00531
R-square:	0.9379	0.9676
Adjusted R-square:	0.9377	0.9675
RMSE:	0.002256	0.002162

Table 6.3: Table of the fabricated McKibben muscle's fitted force curve's parameters given pressure $P = 3$ bar, $l_0 = 0.26$ m, and $r_0 = 0.006$ m.

	Contraction	Extension
Linear model Poly3:		
$f(x) = p1*x^3 + p2*x^2 + p3*x + p4$		
Coefficients:		
p1 =	-3.155e-07	-1.205e-06
p2 =	2.198e-05	6.569e-05
p3 =	-0.002013	-0.002939
p4 =	0.05853	0.07352
Goodness of fit:		
SSE:	0.007768	0.008609
R-square:	0.9813	0.9865
Adjusted R-square:	0.9813	0.9865
RMSE:	0.002214	0.002328

Table 6.4: Table of the fabricated McKibben muscle's fitted force curve's parameters given pressure $P = 4$ bar, $l_0 = 0.26$ m, and $r_0 = 0.006$ m.

	Contraction	Extension
Linear model Poly3:		
$f(x) = p1*x^3 + p2*x^2 + p3*x + p4$		
Coefficients:		
p1 =	-1.692e-07	-9.539e-07
p2 =	1.61e-05	6.644e-05
p3 =	-0.002392	-0.003602
p4 =	0.08128	0.1002
Goodness of fit:		
SSE:	0.009777	0.01807
R-square:	0.9904	0.9896
Adjusted R-square:	0.9904	0.9896
RMSE:	0.00228	0.00301

Table 6.5: Table of the fabricated McKibben muscle's fitted force curve's parameters given pressure $P = 5$ bar, $l_0 = 0.26$ m, and $r_0 = 0.006$ m.

	Contraction	Extension
Linear model Poly3:		
$f(x) = p1*x^3 + p2*x^2 + p3*x + p4$		
Coefficients:		
p1 =	-2.976e-07	-4.822e-07
p2 =	2.317e-05	3.136e-05
p3 =	-0.002884	-0.003223
p4 =	0.09368	0.1084
Goodness of fit:		
SSE:	0.02398	0.009458
R-square:	0.9929	0.9944
Adjusted R-square:	0.9929	0.9944
RMSE:	0.002296	0.002299

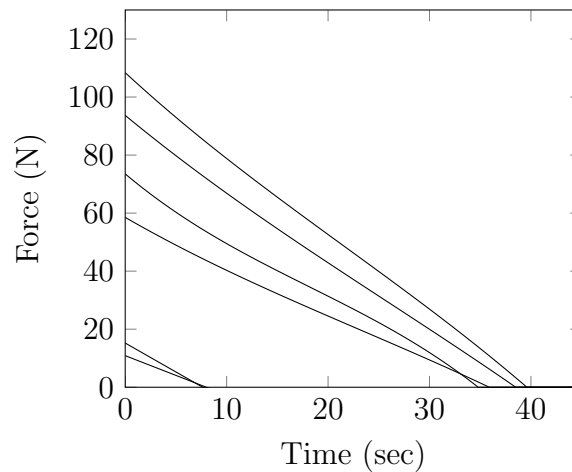


Figure 6-4: REAL Plot of the fabricated McKibben muscle's produced force as a function of constant change in length. Shown is the actuator's fitted force curve given a pressure $P = [1,3,5]$ bar and a constant change in length of 1 mm/sec. In this example $l_0 = 0.26$ m and $r_0 = 0.006$ m.

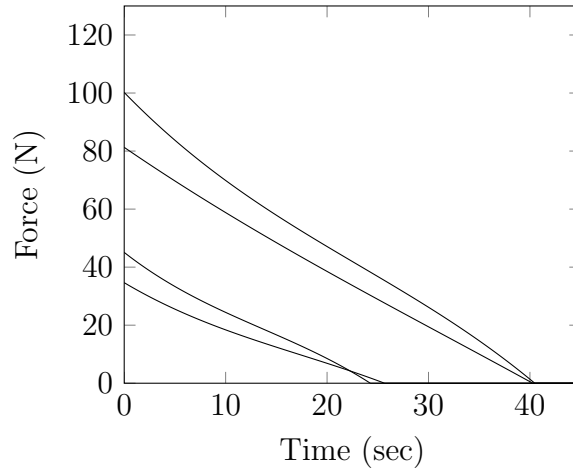


Figure 6-5: REAL Plot of the fabricated McKibben muscle’s produced force as a function of constant change in length. Shown is the actuator’s fitted force curve given a pressure $P = [2,4]$ bar and a constant change in length of 1 mm/sec. In this example $l_0 = 0.26$ m and $r_0 = 0.006$ m.

constant k , and ratio n .

Initially, the McKibben muscle model’s Simulink model was configured to work with the parameter estimator; where, the model’s output was set to produce both a contractile and extensile force. Afterwards, the outputs F_{Con} and F_{Ex} were set as linearisation output points and the estimation application executed. Subsequently, a new project was created and new "Data" and "Time/Tx" input vectors loaded with x and x , respectively; and output channels 1 and 2’s data and time vectors set as f_{Con} and f_{Ex} , and x , respectively. Afterwards, the optimisation parameters were set to α_0 , f_s , k , and n , a new estimation task created, the data set and parameters confirmed, and then executed. In this section’s optimisation, a non-linear least squares method has been used in conjunction with the "Trust-Region-Reflective" algorithm with a maximum of 100 iterations allowed.

Once parameter optimisation had been repeated for pressure $P = [1,2,3,4,5]$ bar, the corresponding α_0 , f_s , k , and n parameters were determined (see table 6.6). Ignoring the parameters of the case where $P = 1$ bar, as discussed, the rms values of the subsequent pressures’ estimated values are given in table 6.7. Interestingly,

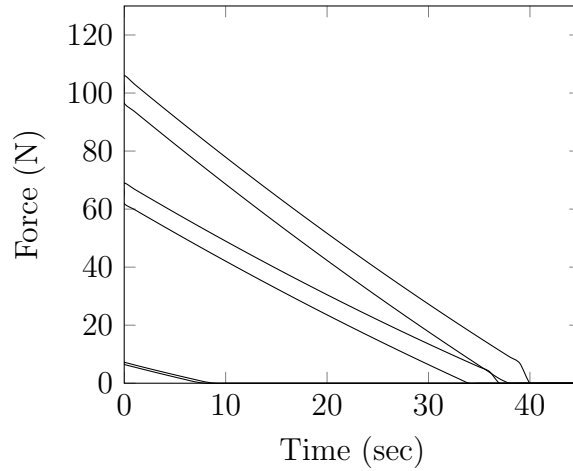


Figure 6-6: SIM Plot of the optimised parameter McKibben muscle model's produced force as a function of constant change in length. Shown is the model's force curve given a pressure $P = [1,3,5]$ bar and a change in length of 1 mm/sec. In this example $l_0 = 0.26$ m and $r_0 = 0.006$ m.

the parameters presented here are in the same order as those presented in [59] ($\alpha_0 = 20$ deg, $f_s = 0.015$, $k = 1.35$, and $n = 13$); however, the initial braid angle is much larger (almost double): explaining why the presented muscle's force is smaller by nearly a factor of 10 (compared to Tondu's [59]). Figures 6-6 and 6-7 depict the optimised McKibben muscle model's produced force as a function of a ramp change in length applied at 1 mm/sec.

6.4 Static and Dynamic Assistive Device Controller properties

In this section, this thesis presents the results of static and dynamic simulation of the assistive device controller, which has been implemented in MathWorks' Simulink environment. In the simulations, the antagonistic actuators muscles were characterised by the following parameters: $l_0 = 0.26$ m, $r_0 = 0.006$ m, $\alpha_0 = 39.7963$ deg, $f_s = 0.0224$, $k = 1.8945$, $n = 19.5911$, and acted through a moment of $R = 0.02$ m.

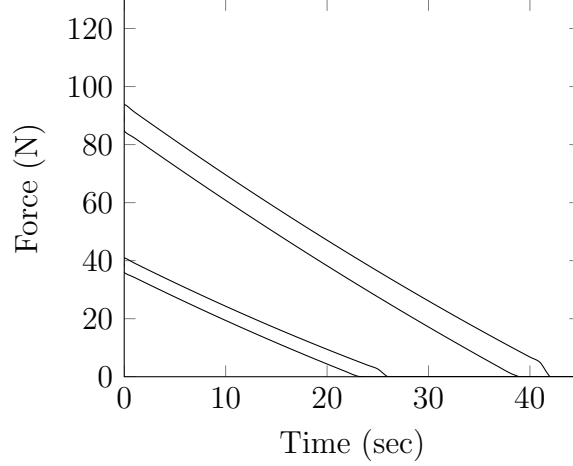


Figure 6-7: SIM Plot of the optimised parameter McKibben muscle model's produced force as a function of constant change in length. Shown is the model's force curve given a pressure $P = [2,4]$ bar and a change in length of 1 mm/sec. In this example $l_0 = 0.26$ m and $r_0 = 0.006$ m.

Table 6.6: Table of the McKibben muscle's optimised parameters. Shown are the results of Simulink optimisation of the initial braid angle α_0 , static friction coefficient f_s , constant k , and contact ratio n values given pressure $P = [1,2,3,4,5]$ bar, $l_0 = 0.26$ m, and $r_0 = 0.006$ m.

1 Bar	2 Bar	3 Bar	4 Bar	5 Bar
$\alpha_0 = 45$ deg	$\alpha_0 = 40$ deg	$\alpha_0 = 39.57$ deg	$\alpha_0 = 39.359$ deg	$\alpha_0 = 40.25$ deg
$f_s = 0.012$	$f_s = 0.024685$	$f_s = 0.023357$	$f_s = 0.0022345$	$f_s = 0.018894$
$k = 4.995$	$k = 2.4724$	$k = 1.7997$	$k = 1.6003$	$k = 1.572$
$n = 19.797$	$n = 19.547$	$n = 19.567$	$n = 19.581$	$n = 19.669$

Table 6.7: Table of the RMS values of the optimised McKibben muscle model's parameters. Shown are the working values for braid angle α_0 , static friction coefficient f_s , constant k , and contact ratio n values used in this chapter.

$$\begin{array}{c}
 \overline{\text{rms}\alpha_0 = 39.7963 \text{ deg}} \\
 \text{rms}f_s = 0.224 \\
 \text{rms}k = 1.8945 \\
 \overline{\text{rms}n = 19.5911}
 \end{array}$$

In addition, a limb segment modelled as a critically damped pendulum of mass $m = 0.3$ kg and length $l = 0.35$ m has been used as the simulations' plant.

In the first part of the simulation, a "static", unperturbed case has been investigated. Here, only the effects of tonic CPG input T on the modelled limb has been considered. Figure 6-8(a) to figure 6-8(e) depict the corresponding evoked transient response as a function of $T = [3e-9, 4e-9, 5e-9, 6e-9, 7e-9]$. It can be seen that as T tends towards $7e-9$, the peak angular displacement changes; increasing from 0.3073 rad at $T = 3e-9$ to 0.7218 rad at $T = 7e-9$: a 134.87 % increase. Furthermore, as T increases, the onset of oscillation reduces; decreasing from 2.3140 sec at $T = 3e-9$ to 1.7695 sec at $T = 7e-9$: a 23.50 decrease. Interestingly, as the input increases, the initial preferred direction of oscillation changes. For example, given $T = 5e-9$, it can be seen that the joint's transient response follows a negative path; whereas, the other tonic values elicit positive rotations.

In the second part of the simulation, the "dynamic", driven case has been investigated. Here, a combination of tonic inputs and a 0.175 Nm, $\pi/3$ rad/sec sinusoidal driving function's effects on the modelled limb's transient response has been considered. Figure 6-9(a) to figure 6-9(e) depict the corresponding evoked transient response as a function of $T = [3e-9, 4e-9, 5e-9, 6e-9, 7e-9]$. It can be seen that as T increases, both the frequency and amplitude of the entrained angular displacement increase; ranging from 0.3298 rad and 1.1872 rad/sec at $T = 3e-9$ through to 0.6909 rad and 1.7830 rad/sec at $T = 7e-9$.

6.5 Antagonistic Actuator and Realised Controller

Having developed the assistive device control paradigm, determined the fabricated McKibben muscles' optimum parameters, and presented results from simulation of the controller and modelled limb; this section discusses a fabricated antagonistic actuator and realised controller. Subsequently, results from experimentation are presented.

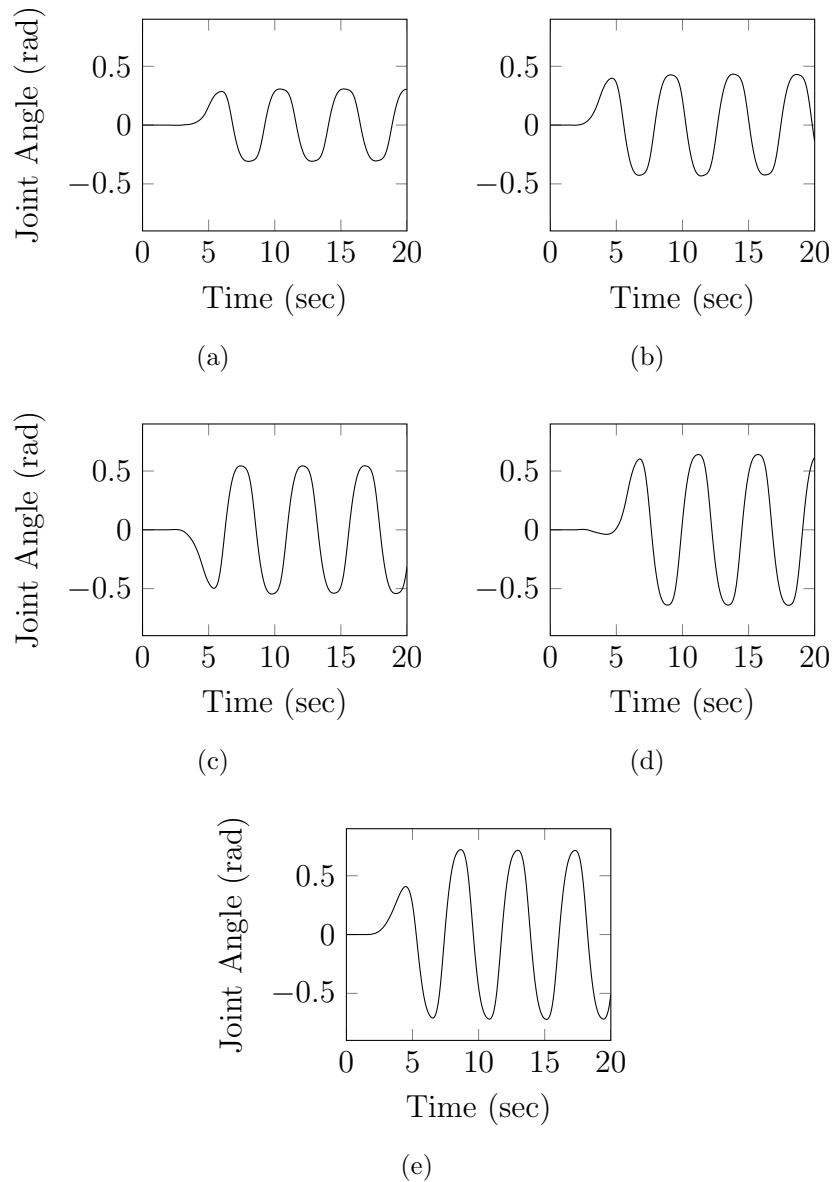


Figure 6-8: Plots of the assistive device controller’s evoked transient response. Figures (a) to (e) depict the antagonistically actuated modelled limb joint angle’s response to a tonic pattern generator input $T = [3e-9, 4e-9, 5e-9, 6e-9, 7e-9]$. In this example $l_0 = 0.26$ m, $r_0 = 0.006$ m, $\alpha_0 = 39.7963$ deg, $f_s = 0.0224$, $k = 1.8945$, $n = 19.5911$, and $P_0 = 3$ bar.

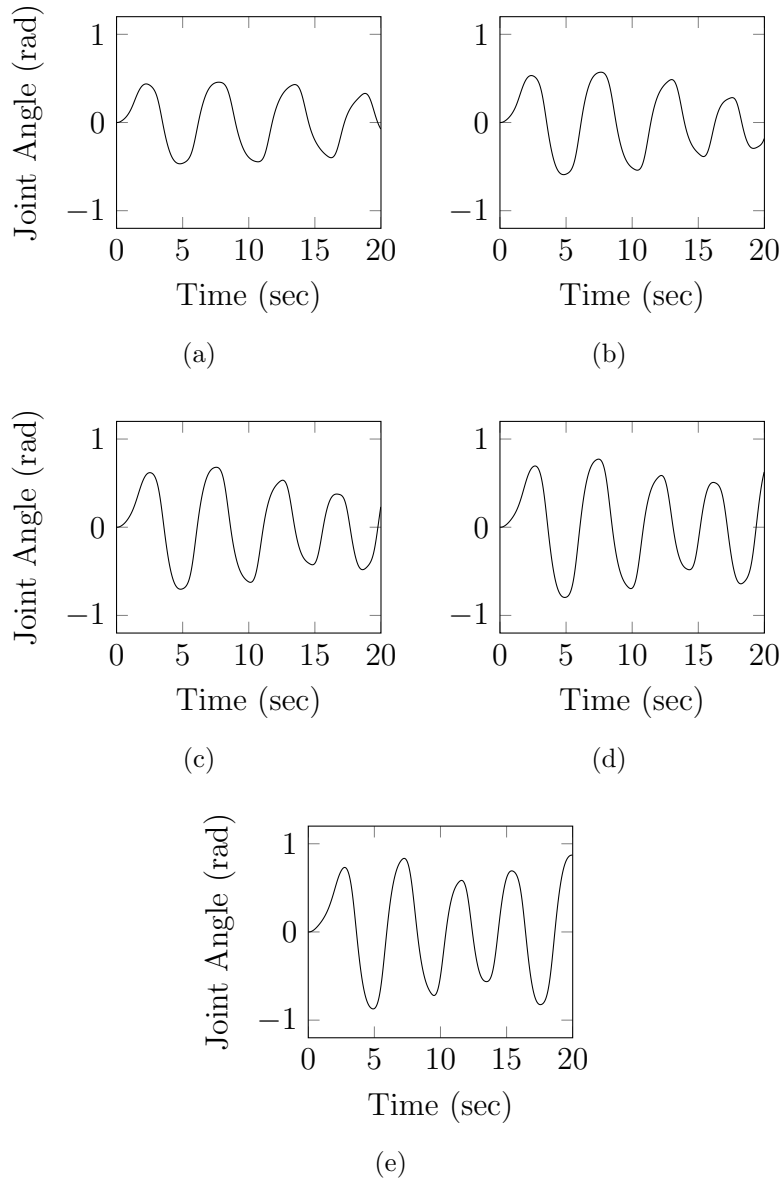


Figure 6-9: SIM Plot of the assistive device controller's transient response to a sinusoidal driving force. Figures (a) through (e) depict the antagonistically actuated modelled limb joint angle's transient response to a sinusoidal driving force distally applied given a tonic pattern generator input $T = [3e-9, 4e-9, 5e-9, 6e-9, 7e-9]$. In this example $l_0 = 0.26$ m, $r_0 = 0.006$ m, $\alpha_0 = 39.7963$ deg, $f_s = 0.0224$, $k = 1.8945$, $n = 19.5911$, and $P_0 = 3$ bar.

Antagonistic Actuator

The antagonistic actuator consisted of two of the presented McKibben muscles connected in antagonism, extensor and flexor proportional-pressure regulators, a length of chain, a sprocket, and a fabricated "limb". The actuator's base plate contained a slot that allowed the mounted sprocket to be moved. Threaded U-bolts were screwed into the McKibben muscles' end-caps, which the chain segment's ends were fixed to. The muscles' remaining ends were screwed into a perpendicular section of the actuator's base. At pressure $P = 0$ bar, the muscles were slack (i.e. length $l = l_0$) and loosely connected to the sprocket; however, once a pressure $P \geq 0.6$ bar was applied the muscles contracted approximately 20 mm: corresponding to 50 % of the maximum contraction ratio $\epsilon_{Max} = 0.15$. The antagonistic actuator's limb was designed in CAD package SolidWorks and was made from aluminium; where, the corresponding mass distribution properties of the limb are given below:

$$\begin{aligned} M &= 0.6381 \text{ kg} \\ I &= \begin{bmatrix} 0.0082 & -0.0002 & 0.0000 \\ -0.0002 & 0.0005 & 0.0000 \\ 0.0000 & 0.0000 & 0.0081 \end{bmatrix} \text{ kgm}^2 \\ CG &= \begin{bmatrix} 0.0078 \\ 0.1434 \\ 0.0001 \end{bmatrix} \text{ m} \end{aligned}$$

where M is mass, I , the inertia; and CG , the centre of gravity.

Realised Controller

Leveraging the rapid growth in the computational power of cost-effective embedded development platforms, e.g. the Arduino [1], Raspberry Pi [48], and the BeagleBoard [2], the assistive device controller's Simulink model has been deployed to an embed-

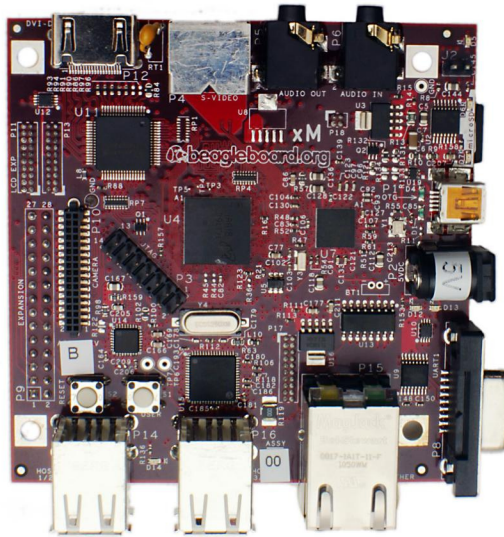


Figure 6-10: BeagleBoard-xM used to run the control approach’s Simulink model in real time. The BeagleBoard embedded target has “laptop-like” performance and is built around an ARM Cortex –A8 microcontroller with 512 MB of RAM. Pictured is the RS-232 serial port, USB ports, and 10/100 Ethernet port.

ded target; where, data has been acquired in real time and used as input to the assistive device controller. The control hardware for the realised controller consisted of a BeagleBoard xM (see figure 6-10), an Arduino UNO (figure 6-11), PWM-to-analogue voltage filters, and proportional pressure control valves. The BeagleBoard embedded target is a single board computer, with performance comparable to standard desktop computers’. The embedded system is built around an ARM Cortex A8 micro-controller with 512 MB of RAM. The Arduino is a development platform built around ATMEL’s ATmega 328p micro-controller, which is comparable to many other standard micro-controllers, e.g. PIC18F4520. The PWM-to-analogue voltage filters are, essentially, non-inverting operational amplifier circuits with a fixed gain. Generally speaking, the control strategy’s hardware can be split into two core components: first, the embedded target – the BeagleBoard; and second, the antagonistic actuator interface – the Arduino and PWM-to-analogue voltage filters.

The Arduino was used to generate the 31.25 kHz pulse width modulated signals

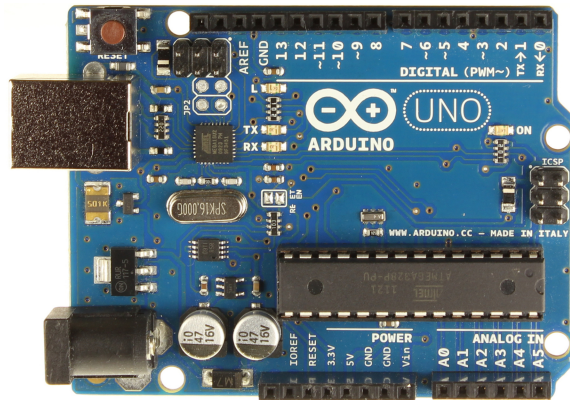


Figure 6-11: Pictured is the Arduino Uno used for sampling the assistive device’s joint angles and generating the PWM output used for controlling the FESTO proportional-pressure regulators.

$pExt_n$ and $pFlex_n$, which were output via pins 9 and 10, respectively. The Arduino’s outputs were sent to the PWM-to-analogue filter, which in turn generated continuous 0 – 5 V voltages. The filters’ outputs were then passed to non-inverting, operational amplifier LM358-based, amplifier circuits, whose gain was equal to two. The resulting output was a 0 – 10 V command, which was sent to the actuator’s corresponding proportional-pressure regulators.

With respect to the Arduino’s output, the modality of the signal is tied to the target’s input form and bounding ranges. Here, the output was conditional to the proportional control valves’ input range (0 – 10 V). It could be argued that such modalities and bounds are irrelevant; rather, it is the information that is conveyed in the signal that is of import. As such, any system that conveys the controller’s output to the actuators would suffice; however, the advantage of the approach discussed previously is in its simplicity, cost effectiveness, and availability. Wide ranging sources of literature, e.g. reference manuals, application notes, and on-line examples, exist; facilitating the development of the hardware interface. Moreover, using an already existing platform for model deployment results in time and financial savings (i.e. development of a proprietary embedded system is avoided). The widespread availability of the LM358 operational amplifier also contributes towards the ease of

replicating the presented solution for other potential wearable assistive device applications.

In order to convert the pulse width modulated signal into a continuous 0 – 10 V signal, it was first filtered. The PWM-to-analogue voltage filter was essentially two cascaded low-pass, passive filters with a LM358 voltage following buffer isolating the two systems. The advantage of the LM358 was that it was designed to operate from a single supply and could be operated directly from a standard 5 V supply. Furthermore, the operation amplifier was designed to be used in conventional operation amplifier circuits, such as that discussed herein. The low pass filters' resistance R and capacitance C were 100 k Ω and 10 pF, respectively. The corresponding transfer function is given below:

$$F(s) = \frac{1/RC^2}{s^2 + 2/RC + 1/RC^2} \quad (6.10)$$

where the filter's time constant $RC = 1e^{-5}$. The above system is a second order system; as such, a unit-step input has been used to reveal time-response characteristics of the filter. For the defined values of R and C , the rise time, settling time, and steady-state values were $3.35e^{-5}$ sec, $5.83e^{-5}$ sec, and 1.0 V, respectively; demonstrating the filter would respond quickly to a change in the Arduino's PWM output. The response characteristics were calculated for a settling time within a 2% bound and a rise time between 10% and 90% of the steady state value.

Following the PWM filter, the analogue voltage was weighted by the non-inverting LM358 operational amplifier circuit. The gain of the circuit was set by:

$$G = 1 + \frac{R_f}{R_g} \quad (6.11)$$

where a nominal resistance of 1 k Ω has been used for resistor R_f .

With respect to the realised controller's software, control of the antagonistic actuator was implemented using MathWorks' MATLAB and Simulink mathematical environment, the Eclipse Foundation's Eclipse integrated development environment (IDE), and the Ubuntu operating system.

As discussed, pins 9 and 10 were used to output the PWM-to-analog filters' $pExt_n$ and $pFlex_n$ inputs. The `analogWrite()` function was used to generate the pulse width varying signals; however, the default frequency (490 Hz) was too low to use in conjunction with the filter. For a desired PWM frequency of approximately 30 kHz, the following equation can be used to determine the prescaler N and TOP values:

$$f_{\text{PWM}} = \frac{f_{\text{clk}}}{2N\text{TOP}} \quad (6.12)$$

Here, for $N = 1$ and $\text{TOP} = 256$, $f_{\text{PWM}} = 31.25$ kHz. To achieve this, the ATmega328's Timer 1 control register TCCR1B was set using the following instruction:

```
TCCR1B = TCCR1B & 0b11111000 | 0x01
```

Operators `&` and `||` are the bitwise AND and OR operations. If the bits of TCCR1B were set, AND'ing with zero clears the bit; whereas, OR'ing with one sets the bit. The advantage of changing timer 1's control register is that it avoids affecting the `delay()` and `millis()` functions, which are controlled by timer 0.

As with the Arduino's output, the modality of any input signal is tied to the nature of the sensor (i.e. digital or analogue) and mode of communication (e.g., I2C, SPI, or RS232). Fortunately, the Arduino Uno supported SPI, TWI, and I2C communication, as well as, 10-bit analogue to digital conversion (ADC). Therefore, a wide range of interfacing options existed for interfacing between a number of devices.

6.6 Static and Dynamic Actuator and Controller properties

In this section, the chapter presents the results of static and dynamic experiments carried out on the fabricated antagonistic actuator and realised controller. In the experiments, the antagonistic muscles were characterised by the following parameters: $l_0 = 0.26$ m, $r_0 = 0.006$ m, $\alpha_0 = 39.7963$ deg, $f_s = 0.0224$, $k = 1.8945$, $n = 19.5911$, and acted perpendicularly about the actuator's sprocket, whose radius was

approximately 0.025 m. The actuator's discussed limb acted as joint's inertial load, and had a mass $m \approx 0.63$ kg. In this experiment, the actuator acted in the vertical plane (akin to a "biceps" curl).

In the first experiment, the "static", unperturbed case has been considered. Here, only the effects of tonic CPG input on the actuator's transient response has been investigated. Figure 6-12(a) to figure 6-12(e) depict the corresponding evoked transient response as a function of increasing T . It can be seen that as T tends towards $7e - 9$, the peak displacement increases from 0.5230 rad at $T = 3e-9$ through to 1.1586 rad at $T = 7e-9$: a 121.53 % increase. In addition, it can be seen that, as T increases, the frequency of the generated oscillations remain constant.

In the second part of the experiment, the "dynamic" case; where, a spring was attached between the actuator's base and the limb's distal end, and angle-dependent torque used to perturb the system. Here, both the contribution of tonic input T and the disturbance's effects have been investigated. Figure 6-13(a) to figure 6-13(e) depict the corresponding evoked transient response as function of increasing T . It can be seen that as the tonic input increases, the peak displacement increases from 0.1371 rad at $T = 3e-9$ through to 0.2924 rad at $T = 7e-9$: a 113.28 % increase. Furthermore, it can be seen that the frequency of oscillation also remains relative constant; changing slight from 1.5673 rad/sec at $T = 3e-9$ to 1.8475 rad/sec at $T = 7e-9$: a 17.88% increase.

6.7 Summary

In this chapter, the thesis' assistive device control paradigm and fabricated McKibben muscles are discussed and results from experimentation, fitting of curves to produced force, and optimisation of the muscles model's parameters presented. Subsequently, results from simulation of an antagonistically actuated, pattern generator controlled, modelled limb has been presented. In addition, a fabricated antagonistic actuator and realised controller are discussed and results from static and dynamic experiments presented.

With respect to the McKibben muscles, experimentation has shown that they

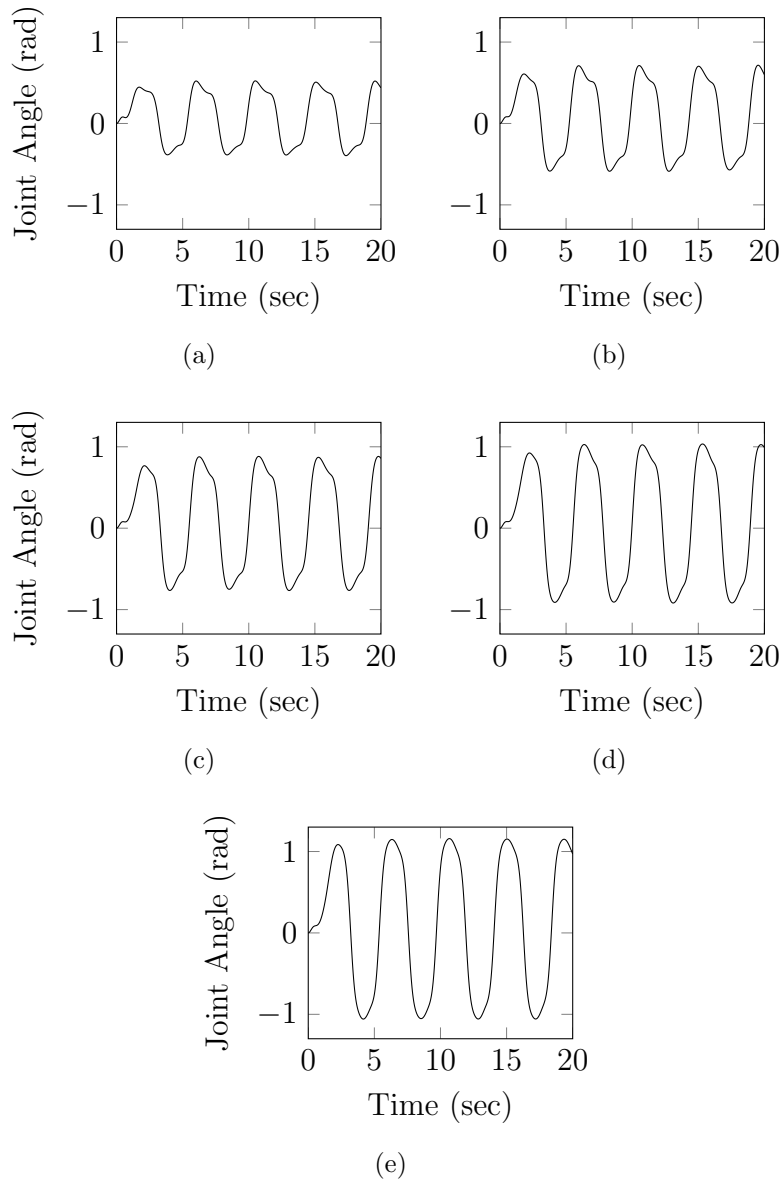


Figure 6-12: REAL Plot of the fabricated antagonistic actuator's transient response to a tonic CPG input. Figures (a) through (e) depict the realised assistive device controller, fabricated antagonistic actuator, and limb arm's transient response given input $T = [3e-9, 4e-9, 5e-9, 6e-9, 7e-9]$ and nominal pressure $P_0 = 3$ bar. In the experiment $l_0 \approx 0.26$ m and $r_0 \approx 0.006$ m.

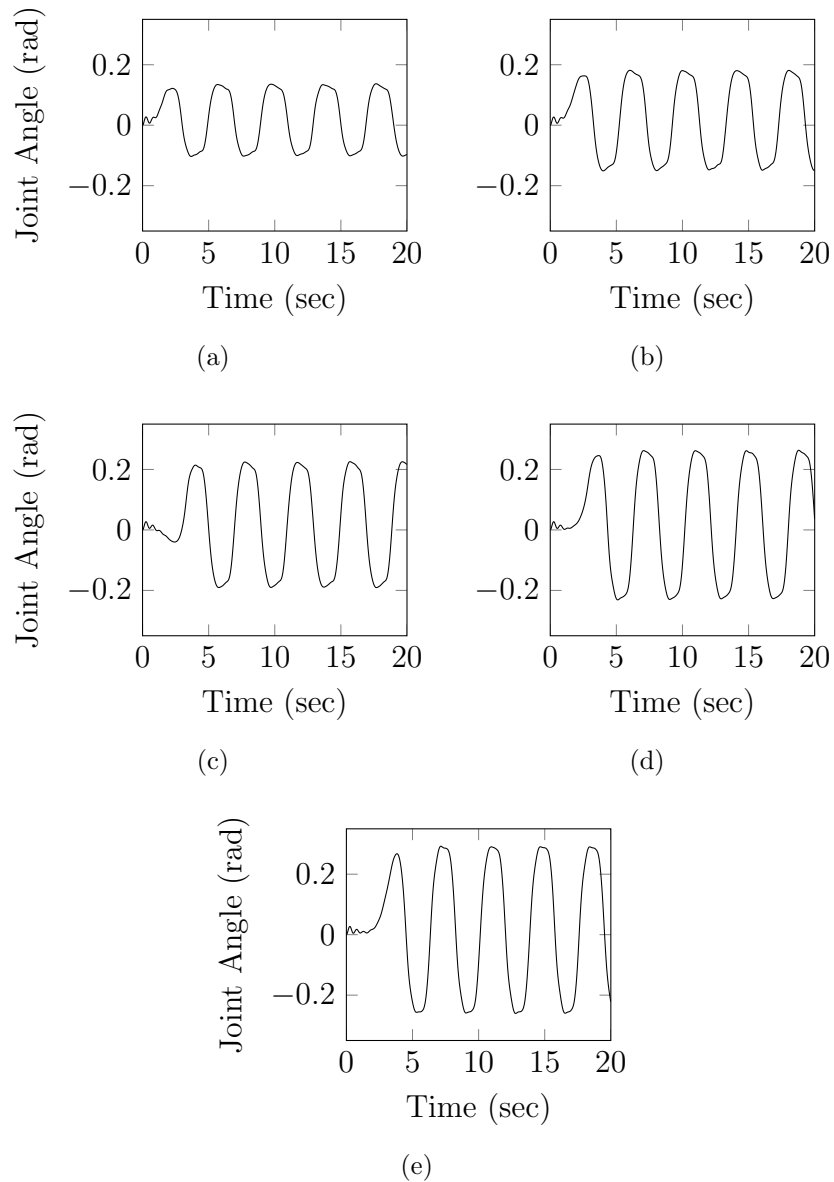


Figure 6-13: REAL Plot of the fabricated antagonistic actuator’s transient response to a joint angle-dependent force. Figures 6-13(a) through 6-13(e) depict the realised assistive device controller, fabricated antagonistic actuator, and limb’s resulting displacement given a spring fixed to the arm’s end, tonic CPG input $T = [3e-9, 4e-9, 5e-9, 6e-9, 7e-9]$, and nominal pressure $P_0 = 3$ bar. In the experiment $l_0 \approx 0.26$ m and $r_0 \approx 0.006$ m.

were able to produce an, approximate, maximum force of x N at 1 bar through to y N at 5 bar. Curve fitting third order polynomials to the force-length vectors has been shown to accurately account for the produced force, with R^2 values ≈ 1 presented. Subsequently, successful parameter estimation resulted in determination of the muscle model's initial braid angle, static coefficient of friction, constant, and contact ratio; where, the rms values were $\alpha_0 = 39.7963$ deg, $f_s = 0.224$, $k = 1.8945$, and $n = 19.5911$. These values were found to in the same order as those documented in literature [59]; however, the large α_0 value meant that the muscle's potential produced force was significantly reduced.

Subsequently, results from simulation of the assistive device controller, antagonistic McKibben muscles, and a modelled limb have been presented. Given a tonic CPG input $T = [3e-9, 4e-9, 5e-9, 6e-9, 7e-9]$, static simulation has shown the system capable of generating a smooth transient response; where, the peak displacement ranged from 0.3073 rad at $T = 3e-9$ through to 0.7218 rad at $T = 7e-9$ given nominal pressure $P_0 = 3$ bar. Under the dynamic case, where the modelled limb joint experienced a 0.175 Nm, $\pi/3$ rad/sec sinusoidal driving function, the coupled system was shown to entrain to the input, with peak displacements tending towards 0.3298 rad at $T = 3e-9$ through to 0.6909 rad at $T = 7e-9$ given $P_0 = 3$ bar.

Having modelled the assistive device control paradigm, a fabricated antagonistic actuator and realised controller have been presented; where, static experimentation has shown a peak displacement ranging from x rad at $T = 3e-9$ through to y rad at $T = 7e-9$ given nominal pressure $P_0 = 3$ bar. For the dynamic experiment, where a spring of, approximately, x N/m was fixed to the actuators limb's end, was shown to account for the angle-dependent disturbance. Peak displacement ranging from x rad at $T = 3e-9$ through to x rad at $T = 7e-9$ given $P_0 = 3$ bar were achieved.

To conclude, this chapter has presented and successfully implemented the assistive device control paradigm; facilitating a means of compliant actuation and adaptive control: a key objective of this research. With respect to wearable assistive devices, this chapter has demonstrated the feasibility of controlling and actuating a device by means of antagonistic coupled McKibben muscles and central pattern generator.

Chapter 7

Conclusion

7.1 Future Work

This research's aim has been the development of a compliant and adaptive control technology for wearable assistive devices; where, this thesis has emulated aspects of the biological domain's control of movement through incorporating a novel pattern generator and antagonistic McKibben muscles.

A range of contributions have been made: a number of neuron models have been presented, their operation discussed, and qualitative behaviour determined via simulation; results of a parametric analysis of Hill's muscle model has been presented in addition to those of individual and antagonistic muscle models' simulation; a novel central pattern generator has been presented and results of an in-depth analysis discussed; pneumatic McKibben actuators have been modelled and results from simulation of individual and antagonistic muscles shown to effect compliant actuation; and a novel assistive device control paradigm presented, where experimentation has validated this thesis' approach.

However, it is evident that there still exists a number of topics deserving of further investigation. These include, but are not limited to:

- **Sequential and compound motions.** In chapter 2, an in-depth literature review of the vertebrate nervous system has been presented. With respect

to spinal-cords CPG's, it has been shown that they are organised into networks that control correlated motor pools [54]. Descending pathways (e.g. the mid-brain's MLR signal) modulate the rhythm and pattern formation layers, and motor pools, generating sequential movements (e.g. gait) [55]. Therefore, the presented pattern generator's hierarchy is incapable of displaying this behaviour. We propose that CPGs used for control of a wearable assistive device be connected in a series of networks, in order to facilitate sequential and compound movements, weakly "innervating" neighbouring actuators across a specified joint. Extending the describing function analysis of chapter 5 to inter-connected pattern generator networks can be used to elucidate their performance.

- **Discrete motions.** Due to its neurons' spike-rate adaptation, the CPG presented in this thesis generates an oscillatory output. In the engineering domain, this output could correspond to a desired trajectory θ_d or joint torque τ_d . However, a limitation is that the pattern generator is unable to produce discrete movements. This can be addressed by looking towards the differential activation of the antagonistic actuator's extensor and flexor muscles, where it has been shown to effect joint rotation. It is proposed that a library of short, succinct "activation patterns" be built up, which could be combined to form distinct movements.
- **Theoretical questions.** Chapter 5's theoretical analysis of the presented pattern generator has shown it to be robust, adaptive, and capable of achieving a wide range of dynamics. However, the chapter does not present a means of automatically determining a pattern generator limit cycle solution; only a graphical describing function analysis method. In future works, it is proposed that a mechanism for specifying pattern generator performance be developed, which in turn could be used for determining a set of parameters that achieve the desired CPG output characteristics.
- **Compliant actuators.** Chapter 6 presented the pneumatic muscle actuators

that have been used throughout this thesis. The McKibben muscle has been shown to be congruent with Hill's muscle model [59], enabling compliant joint actuation when antagonistically coupled. However, while they possess excellent power-to-weight ratios and are cost effective, the need to have a compressed medium storage tank or source nearby is a considerable limitation. Future works can look towards optimising the performance of the muscle, e.g., minimising internal volumetric change, while maximising force generation; therefore, reducing the quantity of compressed air expended during a muscle's contraction, minimising their reliance on the fixed supply, and allowing for smaller, more portable sources to be used.

7.2 Discussion

This thesis has demonstrated the possibility of controlling a wearable assistive device through exploiting the compliance of antagonistically actuated, McKibben muscles, and the adaptability of the presented central pattern generator. However, while the approach has demonstrated the power of the pattern generator, there is still a great deal of work that needs to be carried out to achieve a level of control comparable to humans, let alone lesser vertebrates. This section considers how to bridge the current state of technology, considering other ways to utilise the pattern generator, exploiting a wearable assistive device's mass-distribution properties, completing areas of research that need to further evaluated, and looking at the problem of complex pattern moderation.

- **Traditional and pattern generator control.** In contrast to traditional control, the pattern generator does not follow a specified trajectory; rather, it modulates its output (which in the absence of feedback is determined by its governing equations, gains, tonic inputs, etc.) based on an input signal. The advantage of this is that it facilitates the entrainment of the pattern generator's output to the natural frequency of the system; however, it restricts the applicability of the presented control approach to novel situations, such as control

of wearable assistive devices. It is proposed that an automatic mapping function convert a desired trajectory's amplitude and frequency into a tonic input, or modulation of the CPG's output. In this way, the pattern generator could be applied to traditional control problems, entraining to a task's dynamics, minimising expended energy, and following a desired set-point.

- **Pattern generator structure.** With respect to the generation of voluntary motor commands, chapter 2 has shown there exists a wide range of descending pathways that modulate the cervical/thoracic and lumbar/sacral central pattern generator's motor patterns; moreover, inter-neurons and gamma motor-neuron "servo-motor" loops affect motor patterns' firing envelopes. In terms of the presented CPG, these inter-neuron and supra-spinal pattern envelope modulators have not been included in the system's dynamics. If the pattern generator's structure was modified from that of Graham Brown's characteristic half-centre model [5][6] to a more complex network, such as, Rybak et al's [54] two-level rhythm and pattern generator, it is argued, more complex motor pattern behaviour could be achieved, given a medium for generating the moderation commands.
- **Voluntary movements** Many of the examples presented in this thesis exploit system dynamics; making use of the central pattern generator's characteristic adaptation and pneumatic muscle's compliance. It is important, however, to consider static, i.e. voluntary, tasks. Humans day-to-day movements aren't just a compound set of dynamic movements; rather, they are a highly modulated output, one which higher neurological systems oversee. The ability to modulate the pattern generator's output to facilitate complex reaching tasks would be an exciting aspect of research.

As discussed, this research has led to a central pattern generator (CPG) controlled and antagonistically actuated wearable assistive device (WAD) control technology. Furthermore, to illustrate its applicability, a single degree-of-freedom (DOF) test-bed has been developed, and the results of simulation and testing presented. In order

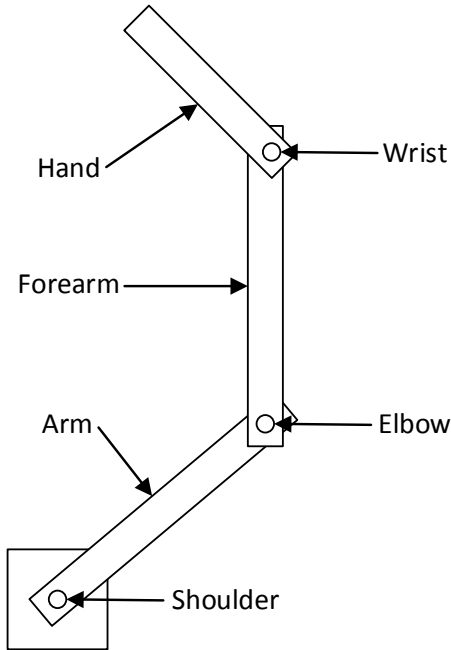


Figure 7-1: Multiple degree-of-freedom manipulation that could be used in future works.

to illustrate the scalability of the control technology, the following multiple DOF manipulator and scenario, which could be developed in further works, is presented:

Here, the manipulator of figure 7-1 consists of three links, the hand, forearm, and arm; where, each link is connected together by a revolute joint constrained to rotate about the \vec{Z} axis. Each joint, i.e. the shoulder, elbow, and wrist, are controlled by an independent CPG. The manipulator's potential use scenario consists of two parts: (a) each joint's CPG is activated and the manipulator free to move (eventually reaching equilibrium), and (b) when an external "handshaking" stimulus is applied to the hand link. It is expected that the arm, forearm, and hand links' CPGs will entrain to the frequency of the handshaking stimulus. This scenario could be manipulated further by cascading the outputs of prior controllers to the inputs of

subsequent controllers.

7.3 Summary

This thesis has presented a novel, neuroscience-based control paradigm for an antagonistically actuated, wearable assistive device. The approach exploits the adaptivity of the presented central pattern generator, which is used to drive antagonistically coupled McKibben muscles. The CPG uses angular feedback to entrain to the natural frequency of a system by adjusting its output relative to a joint's position. Figure 7-2 depicts the thesis' chapters and the chapters' core topics.

In chapter 2, the current state of passive and active assistive device technology and traditional control approaches have been reviewed. Following that, an overview of the nervous system has been presented; where, the central nervous system's hierarchy has been identified, the operation of neurons, muscles, and central pattern generators discussed. Based on the review of relevant literature, it was concluded that current actuators' lack of compliance and intelligence was responsible for impeding assistive device development; whereas, the nervous system's skeletal muscles and patten generators were identified as being responsible, in addition to descending pathways, for generating complaint and adaptive control.

Chapter 3 presented the Integrate-and-Fire, Izhikevich, and Hodgkin-Huxley neuron models, and the results of simulation; comparing their qualitative behaviour. In all three models, the ability to generate rhythmic spiking was replicated; however, the Hodgkin-Huxley model's depolarisation blocking property meant that if too large a stimulus, here $I = 10$ nA, was applied, the neuron would enter a saturation-like state; which, in terms of a pattern generator, meant that there would exist a maximum threshold capable of being entrained to. In addition, the Hodgkin-Huxley model was also shown to have a much shorter refraction period, being much more sensitive to post-action potential stimulus, in contrast to the Integrate-and-Fire and Izhikevich neurons. As such, either model was proposed as being suitable for development of a pattern generator.

In chapter 4, Hill's muscle model, an implementation of a soleus muscle, and

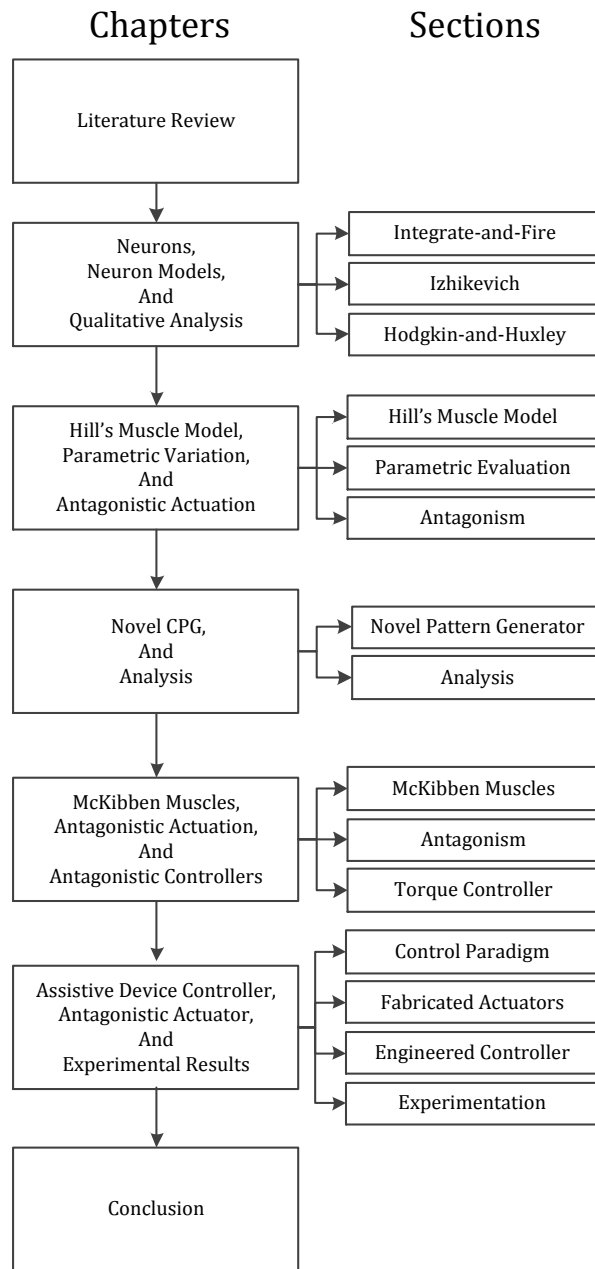


Figure 7-2: Block diagram of this thesis' chapters and chapters' topics.

results from parametric variation of the series and parallel elements' stiffness and viscosity was presented. Under passive condition, it was shown muscle tension T was tightly coupled to k_{se} , the steady state value T_{ss} was affected by k_{pe} , and damping b affects the "spike" generated in response to a ramp stretch of 4 mm applied at 100 mm/sec. Given an active force $A = 10$ N, increasing A was shown to result in a step-like increase in tension; whereas, the muscle tension increased as k_{se} increased, the steady state reduced as k_{pe} increased, and damping b slowed the muscle's transient response to the aforementioned ramp stretch. In addition, an antagonistic pairing of two soleus muscles has been presented; where, differential activation resulted in a modelled limb rotating from 0 rad to 0.459 rad given $A_E = [10,20,30,40,50]$ N and $A_F = 10$ N. Furthermore, given equal activation, the coactivated system was shown to increase joint stiffness; reducing displacement from 0.09 rad at 0 N to 0.06 N at 2 N given a disturbance of 3.5 Nm.

Chapter 5 presented a novel central pattern generator, which consisted of two, mutually inhibited, Integrate-and-Fire neurons of chapter 3. Given a tonic input T , the CPG was shown to generate an oscillatory output in the absence of feedback. Furthermore, once given an input, the pattern generator entrained to a near resonance frequency. Subsequently, an in-depth analysis has been presented, where describing function analysis has been discussed and applied to evaluate the non-linear oscillator. Coupling the CPG to a single degree of freedom mechanical system has been used to demonstrate the robustness and sensitivity of the pattern generator.

In chapter 6, the McKibben muscle's model was discussed and results from simulation of individual and antagonistic muscles implemented in Simulink presented. In this chapter, differential activation of the antagonistic extensor and flexor muscles has been shown to elicit rotation of a modelled limb's joint; ranging from 0 rad to 0.8333 rad given $P_E = [1,2,3,4,5]$ bar and $P_F = 1$ bar. In addition, equal coactivation of the muscles has been shown to increase the limb joint's stiffness, reducing the angle's displacement from 0.36 rad at 1 bar to 0.0807 rad at 5 bar. A differential pressure controller has been presented and mono-variable torque controller, which builds upon the previous controller, results in an improved, step-like, transient response.

Chapter 7 presented the thesis' assistive device controller, fabricated McKibben

muscles, an antagonistic actuator, realised controller, and results from simulation and experimentation. In the assistive device control paradigm, a CPG generated a desired trajectory θ_d , which alongside angular feedback θ_m , was fed into a PD controller that generated a desired torque τ_d . The antagonistic actuator's torque controller followed the input, generating an output τ , which acted upon a plant. Angular feedback to the CPG, PD controller, and antagonistic actuator closed the control loop. With respect to the fabricated muscles, given pressure $P = [1,2,3,4,5]$ bar, the produced force ranged from approximately 15 N to 120 N in response to a 40 mm change in length for $l_0 = 0.26$ m and $r_0 = 0.006$ m. Parameter optimisation has found $\alpha_0 = 39.7963$ deg, $f_s = 0.0224$, $k = 1.8945$, and $n = 19.5911$; close to those reported in literature [59]. Subsequent experimentation with a fabricated antagonistic actuator demonstrated oscillatory behaviour, with peak displacement ranging from 0.5230 rad to 1.1586 rad for a tonic input $T = [3e-9,4e-9,5e-9,6e-9,7e-9]$. In addition, the antagonistic actuator and realised controller have been shown to entrain to a sinusoidal driving function.

To conclude; while the nervous system is a complex, inter-related, and hierarchical system; it is argued that this thesis has successfully captured core components', i.e. central pattern generators and skeletal muscles, qualitative properties; emulating them in the engineering domain. The presented assistive device controller can now be used to facilitate the development of active wearable assistive devices, directly address current technologies' lack of compliance and intelligence. While the presented approach is relatively simple, it enables a robust, compliant, and adaptive method of control: fulfilling this thesis' state objective.

Bibliography

- [1] Arduino. Arduino uno, 2013.
- [2] Beagleboard. Beagleboard, 2013.
- [3] B.W. Bequette. *Process Control: Modeling, Design, and Simulation*. Prentice Hall International Series in the Physical and Chemical Engineering Sciences. Prentice Hall PTR, 2003.
- [4] Rex Bionics. Rex bionics, 2011.
- [5] T.G. Brown. The intrinsic factors in the act of progression in the mammal. *Proceedings of the Royal Society of London. Series B, Containing Papers of a Biological Character*, 84(572):308–319, 1911.
- [6] T.G. Brown. On the nature of the fundamental activity of the nervous centres; together with an analysis of the conditioning of rhythmic activity in progression, and a theory of the evolution of function in the nervous system. *The Journal of physiology*, 48(1):18–46, 1914.
- [7] Melrose Kiwi Concept Chairs. Melrose kiwi concept chairs, 2013.
- [8] Ching-Ping Chou and Blake Hannaford. Measurement and modeling of mck-ibben pneumatic artificial muscles. *Robotics and Automation, IEEE Transactions on*, 12(1):90–102, 1996.
- [9] Shadow Robot Company. Shadow air muscles, 2013.

- [10] Rachel E Cowan, Benjamin J Fregly, Michael L Boninger, Leighton Chan, Mary M Rodgers, David J Reinkensmeyer, et al. Recent trends in assistive technology for mobility. *Journal of neuroengineering and rehabilitation*, 9(1):1–8, 2012.
- [11] Cyberdine. Robot suit hal, 2013.
- [12] Emotiv. Brain-controlled wheelchair, 2013.
- [13] Emotiv. Emotiv, 2013.
- [14] J. Feng. Is the integrate-and-fire model good enough? a review. *Neural Networks*, 14:955–975, 2001.
- [15] Festo. Festo, 2013.
- [16] Don Fitz-Ritson. The anatomy and physiology of the muscle spindle, and its role in posture and movement: A review. *The Journal of the Canadian Chiropractic Association*, 26(4):144, 1982.
- [17] R. Fitzhugh. Impulses and physiological states in theoretical models of nerve membrane. *Biophysical journal*, 1(6):445–466, 1961.
- [18] A. Gelb and W.E. Vander Velde. *Multiple-input describing functions and non-linear system design*. McGraw-Hill electronic sciences series. McGraw-Hill, 1968.
- [19] S. Grillner. Neurobiological bases of rhythmic motor acts in vertebrates. *Science; Science*, 1985.
- [20] S. Grillner, T. Deliagina, A. El Manira, RH Hill, GN Orlovsky, P. Wallén, Ö. Ekeberg, and A. Lansner. Neural networks that co-ordinate locomotion and body orientation in lamprey. *Trends in neurosciences*, 18(6):270–279, 1995.
- [21] S. Grillner, P. Wallén, K. Saitoh, A. Kozlov, and B. Robertson. Neural bases of goal-directed locomotion in vertebrates—an overview. *Brain Research Reviews*, 57(1):2–12, 2008.

- [22] AV Hill. The heat of shortening and the dynamic constants of muscle. *Proceedings of the Royal Society of London. Series B, Biological Sciences*, 126(843):136–195, 1938.
- [23] A.V. Hill. *First and last experiments in muscle mechanics*. University Press Cambridge, 1970.
- [24] A.L. Hodgkin and A.F. Huxley. A quantitative description of membrane current and its application to conduction and excitation in nerve. *The Journal of physiology*, 117(4):500, 1952.
- [25] HE Huxley. The double array of filaments in cross-striated muscle. *The Journal of biophysical and biochemical cytology*, 3(5):631–648, 1957.
- [26] Invacare. Invacare, 2013.
- [27] E.M. Izhikevich. Simple model of spiking neurons. *Neural Networks, IEEE Transactions on*, 14(6):1569–1572, 2003.
- [28] E.M. Izhikevich. Which model to use for cortical spiking neurons? *Neural Networks, IEEE Transactions on*, 15(5):1063–1070, 2004.
- [29] E.R. Kandel, J.H. Schwartz, T.M. Jessell, et al. *Principles of neural science*, volume 4. McGraw-Hill New York, 2000.
- [30] G.K. Klute, J.M. Czerniecki, and B. Hannaford. Mckibben artificial muscles: pneumatic actuators with biomechanical intelligence. In *Advanced Intelligent Mechatronics, 1999. Proceedings. 1999 IEEE/ASME International Conference on*, pages 221–226. IEEE, 1999.
- [31] Glenn K Klute, Joseph M Czerniecki, and Blake Hannaford. Artificial muscles: Actuators for biorobotic systems. *The International Journal of Robotics Research*, 21(4):295–309, 2002.

- [32] N. Lan. Stability analysis for postural control in a two-joint limb system. *Neural Systems and Rehabilitation Engineering, IEEE Transactions on*, 10(4):249–259, 2002.
- [33] N. Lan, Y. Li, Y. Sun, and FS Yang. Reflex regulation of antagonist muscles for control of joint equilibrium position. *Neural Systems and Rehabilitation Engineering, IEEE Transactions on*, 13(1):60–71, 2005.
- [34] DAVID C Lin and WZ Rymer. Mechanical properties of cat soleus muscle elicited by sequential ramp stretches: implications for control of muscle. *Journal of neurophysiology*, 70(3):997–1008, 1993.
- [35] JP Lund. Mastication and its control by the brain stem. *Critical Reviews in Oral Biology & Medicine*, 2(1):33–64, 1991.
- [36] A. Lundberg. Half-centres revisited. *Regulatory functions of the CNS. Motion and organization principles*, pages 155–167, 1981.
- [37] M. MacKay-Lyons. Central pattern generation of locomotion: a review of the evidence. *Physical Therapy*, 82(1):69–83, 2002.
- [38] E. Marder, D. Bucher, et al. Central pattern generators and the control of rhythmic movements. *Current biology*, 11(23):986, 2001.
- [39] K. Matsuoka. Sustained oscillations generated by mutually inhibiting neurons with adaptation. *Biological cybernetics*, 52(6):367–376, 1985.
- [40] K. Matsuoka. Mechanisms of frequency and pattern control in the neural rhythm generators. *Biological Cybernetics*, 56(5):345–353, 1987.
- [41] D.A. McCrea and I.A. Rybak. Organization of mammalian locomotor rhythm and pattern generation. *Brain research reviews*, 57(1):134, 2008.
- [42] Barbara M Myklebust. A review of myotatic reflexes and the development of motor control and gait in infants and children: a special communication. *Physical Therapy*, 70(3):188–203, 1990.

- [43] J. Nagumo, S. Arimoto, and S. Yoshizawa. An active pulse transmission line simulating nerve axon. *Proceedings of the IRE*, 50(10):2061–2070, 1962.
- [44] Neurosky. Neurosky, 2013.
- [45] K. Ogata and Y. Yang. *Modern control engineering*, volume 4. Prentice Hall Upper Saddle River, NJ, USA, 1990.
- [46] G.N. Orlovsky, TG Deliagina, S. Grillner, GN Orlovskii, and S. Grillner. *Neuronal control of locomotion: from mollusc to man*. Oxford University Press New York:, 1999.
- [47] B.W. Peterson. Reticulospinal projections to spinal motor nuclei. *Annual review of physiology*, 41(1):127–140, 1979.
- [48] Raspberry Pi. Raspberry pi, 2013.
- [49] Lord Rayleigh. Xxxiii. on maintained vibrations. *The London, Edinburgh, and Dublin Philosophical Magazine and Journal of Science*, 15(94):229–235, 1883.
- [50] Raytheon. Raytheon, 2013.
- [51] Berkely Robotics and Human Engineering Laboratory. Berkely lower ectremity exoskeleton (blex), 2013.
- [52] The Robotics and Vrije Unversiteit Brussel (VUB) Multibody Mchanics Research Group. Bipedal walking robot lucy, 2013.
- [53] I.A. Rybak, J.F.R. Paton, and J.S. Schwaber. Modeling neural mechanisms for genesis of respiratory rhythm and pattern. i. models of respiratory neurons. *Journal of neurophysiology*, 77(4):1994–2006, 1997.
- [54] I.A. Rybak, K. Stecina, N.A. Shevtsova, and D.A. McCrea. Modelling spinal circuitry involved in locomotor pattern generation: insights from the effects of afferent stimulation. *The Journal of physiology*, 577(2):641–658, 2006.

- [55] R. Shadmehr and S.P. Wise. *The Computational Neurobiology Of Reaching And Pointing: A Foundation for Motor Learning*. Computational Neuroscience Series. Mit Press, 2005.
- [56] S.S. Soliman and M.D. Srinath. *Continuous and discrete signals and systems*. Prentice-Hall information and system sciences series. Prentice Hall, 1998.
- [57] Steven Strogatz. *Nonlinear dynamics and chaos: with applications to physics, biology, chemistry and engineering*. Perseus Books Group, 2001.
- [58] Lotte NS Andreasen Struijk. An inductive tongue computer interface for control of computers and assistive devices. *Biomedical Engineering, IEEE Transactions on*, 53(12):2594–2597, 2006.
- [59] B. Tondu and S.D. Zagal. Mckibben artificial muscle can be in accordance with the hill skeletal muscle model. In *Biomedical Robotics and Biomechanics, 2006. BioRob 2006. The First IEEE/RAS-EMBS International Conference on*, pages 714–720. IEEE, 2006.
- [60] Austin Peay State University. Gross anatomy of skeletal muscle, 2013.
- [61] Balth. van der Pol. Lxxxviii. on “relaxation-oscillations”. *Philosophical Magazine Series 7*, 2(11):978–992, 1926.
- [62] M. W. Williamson. *Robot Arm Control Exploiting Natural Dynamics*. PhD thesis, MIT, 1999.
- [63] WL Xu, F. Clara Fang, J. Bronlund, and J. Potgieter. Generation of rhythmic and voluntary patterns of mastication using matsuoka oscillator for a humanoid chewing robot. *Mechatronics*, 19(2):205–217, 2009.
- [64] R. Yuste, J.N. MacLean, J. Smith, and A. Lansner. The cortex as a central pattern generator. *Nature Reviews Neuroscience*, 6(6):477–483, 2005.
- [65] E.P. Zehr and J. Duysens. Regulation of arm and leg movement during human locomotion. *The Neuroscientist*, 10(4):347–361, 2004.